Tau lepton studies at *BABAR*

A thesis submitted to The University of Manchester
for the degree of Doctor of Philosophy
in the Faculty of Engineering and Physical Sciences

2009

Kim Elizabeth Alwyn

Particle Physics Group

School of Physics and Astronomy

Contents

Word Count: 35,270

Abstract

This thesis reports on measurements of the branching fraction for $\tau^- \to K^-\eta\nu_\tau$ and a search for the mode $\tau^- \to \pi^-\eta\nu_\tau$ using data from the *BABAR* experiment at the SLAC National Accelerator Laboratory. The measurements are made using a data set with 470.1 fb^{-1} of integrated luminosity, which includes 432 million $\tau^+\tau^-$ pairs, collected at and just below the $\Upsilon(4S)$ resonance. The branching fraction for the $\tau^- \to K^-\eta\nu_\tau$ channel is found to be

$$\mathcal{B}(\tau^- \to K^-\eta\nu_\tau) = 1.42 \pm 0.11(\text{stat}) \pm 0.06(\text{syst}) \times 10^{-4},$$

which is consistent with previous measurements. The $\tau^- \to \pi^-\eta\nu_\tau$ decay is mediated by a second-class current and is predicted to have a branching fraction of the order 10^{-5}. Second-class currents have never been experimentally observed; this decay mode provides a clean environment to search for them. To avoid bias, the search for $\tau^- \to \pi^-\eta\nu_\tau$ decays is carried out blind. An expected upper limit of the $\tau^- \to \pi^-\eta\nu_\tau$ branching fraction is calculated using Monte Carlo events and found to be $\mathcal{B}(\tau^- \to \pi^-\eta\nu_\tau) < 6.4 \times 10^{-5}$ at the 95% confidence level. After unblinding the data, no evidence for $\tau^- \to \pi^-\eta\nu_\tau$ decays is found and an upper limit on the branching fraction is measured as

$$\mathcal{B}(\tau^- \to \pi^-\eta\nu_\tau) < 9.9 \times 10^{-5}$$

at the 95% confidence level (or 8.5×10^{-5} at the 90% confidence level), which is an improvement on the previous upper limit on this mode.

Declaration

No portion of the work referred to in the thesis has been submitted in support of an application for another degree or qualification of this or any other university or other institute of learning.

Copyright

This work was supported financially by the Particle Physics and Astronomy Research Council (PPARC) and the Science and Technology Facilities Council (STFC) between October 2005 and September 2009.

The Author

Kim Alwyn was educated at the Chase High School and Sixth Form, Worcestershire, between 1994 and 2001 before obtaining a first class MPhys (Hons) at the University of Manchester in 2005. The work presented in this thesis was carried out at the University of Manchester and the SLAC National Accelerator Laboratory in California.

Kim Alwyn
High Energy Particle Physics Group
University of Manchester
Oxford Road
Manchester
M13 9PL
UK

Acknowledgements

Firstly, thank you to **Prof. George Lafferty** for being a consistently excellent supervisor. Thank you for your optimism and enthusiasm for physics, for your patient proof-reading and your invaluable guidance over the last four years.

Thank you to **Jong**, for the endless advice and help with my analysis, for the hours you spent developing the code and for your enduring patience in teaching me the complexities of C++. Thank you for the group breakfasts and lunches, which made me feel welcome when I was new to California.

Many thanks to **The University of Manchester**, particularly the **Particle Physics Group** for providing a cheerful and vibrant environment for my post-graduate research. Thank you for giving me the opportunity to work at the frontier of new physics: it has been an amazing experience which I greatly appreciate.

A special thanks to all the people I've shared an office with; for the assistance in solving programming disasters and dilemmas. Working with such friendly and helpful people made me glad to come into the office each day.

A massive thank you to my dad, **Steve**, without whom I would not be doing physics. Thank you for passing on your enthusiasm for physics and introducing me to the exciting ideas that instilled in me a love of science. A huge thank you to my mum, **Hilary**, for always being there and for always encouraging me without ever pressuring me. To both my parents, thank you for the Skype chats throughout my time in California, your love and support gave me comfort and encouragement, even from 5264.3 miles away.

In Manchester, thank you to my flatmates, **Andy**, **Chris** and **Mark**, for being like a second family to me, and a special thank you to Andy for teaching me

to program and for introducing me to the joys of Linux. Thank you to those who visited me in California, particularly to my brother **Max**: my trip with you was one of the best and I don't think I would have found my way back through the desert without you! And thank you to **Marc**, for your spontaneity and your ability to make me laugh, whatever mood I'm in.

In California, thank you to the Park Towers crew for making Palo Alto as exciting as it could be: **Christina** for bowls of noodles listening to the News Quiz; **Jen** and **Ellie** for the cocktails night (at least what I can remember); **Tim** for introducing me to road trips; **Sudan** for the constant barrage of insults; **Mark** for your dancing; **Michael** for the swanky nights out; **Aidan** and **Graham** for your ridiculous opinions on everything and **Eugenia** for the best lasagne I've ever eaten. Thank you to **Jean** for being there for us all.

Thank you to **Sandra** and **Lisa** for teaching me dance: your classes always made me happy and I hope to continue dancing for many years. Thank you to the **USA National Parks** service and the **California State Parks** service, for protecting the breathtaking natural beauty which gave me so much joy. Every Park I visited was outstanding and the memories will stay with me forever.

Last but not least, thank you to the ***BABAR*** **Collaboration** for all the work which made it such a success and for creating an inspiring environment for a young physicist to learn the ropes in. Thank you to everyone at **PEP-II** and **SLAC**, and to the analysts, technicians and support staff, without whom I would not have had any data to analyse.

Finally, I would like to acknowledge the historic contribution of **Alan Turing** to the work described in this thesis.

To my family

Chapter 1

Introduction

In 2008 half of the Nobel Prize in Physics was awarded to Makoto Kobayashi and Toshihide Maskawa for their theory which predicted the third generation of quarks and explained the source of the asymmetry in the quark sector between matter and antimatter [1]. Over the last 10 years the *BABAR* experiment at the SLAC National Accelerator Laboratory in the USA and the Belle experiment at KEK in Japan have been making the precision measurements which provided the experimental confirmation of this theory.

Originally particles and antiparticles were assumed to have CP symmetry, which means that the laws of physics remain the same if particles and antiparticles are interchanged (C symmetry) and spatial coordinates (x, y, z) are inverted to become ($-x$,$-y$,$-z$) (P symmetry). However, in 1964 Cronin and Fitch observed CP violation for the first time, in the weak decays of neutral kaons [2]. It was also realised that CP violation may be required to produce the observed matter-antimatter asymmetry in the universe [3].

In 1972, when Kobayashi and Maskawa thought of their elegant theory [1], only two generations of quarks were known to exist. The strength of mixing between the quarks participating in weak interactions was described by the Cabibbo angle [4]. Kobayashi and Maskawa realised that if this theory was extended to at least three generations of quarks then CP-violating processes would arise naturally. Therefore, CP violation is incorporated in the Standard Model [5] by including a CP-violating phase in the Cabibbo-Kobayashi-Maskawa (CKM) matrix, which describes the mixing between quarks in weak interactions. In 1974 the existence of the charm quark was confirmed [6]. This was followed by the discovery of the third generation of quarks, as predicted, with the bottom quark

in 1977 [7] and the top quark in 1995 [8].

In 1981 it was noticed that the Kobayashi-Maskawa mechanism for CP violation could be tested by measuring the properties of B mesons [9]. In the late 1980's a strategy emerged for the experimental measurement of CP violation, with the suggestion [10] to use colliders with asymmetric beam energies to increase the separation of the B meson decay vertices to a measurable distance. This led to the building of the *BABAR* and Belle B-factories, which were completed in 1999. In 2001 they both observed large CP violation in the decays of neutral B mesons [11, 12], confirming another key prediction of the theory.

For the following seven years, precision measurements from *BABAR* and Belle provided further supporting evidence for the Kobayashi-Maskawa mechanism. When accepting their Nobel Prize in 2008, Kobayashi and Maskawa acknowledged this contribution in a note [13] saying "Please accept our deepest respect for the B-factory achievements...without which we would not have been able to earn the prize."

The *BABAR* Collaboration exceeded expectations with their program of heavy flavour physics. In fact, the experiment provided a suitable environment for many physics goals, including the study of τ leptons. This continued a long history of particle physics research at SLAC, beginning in 1966 when the 2 mile linac was built and including the discovery of the τ lepton in 1975 [14].

In recent years, publications on the branching fractions of τ decays have been dominated by the B factories [15]. This thesis will describe an analysis of two τ decays modes, $\tau^- \to K^-\eta\nu_\tau$ and $\tau^- \to \pi^-\eta\nu_\tau$, using a data set with an integrated luminosity of $470\,\text{fb}^{-1}$ which was collected by the *BABAR* detector. The $\tau^- \to K^-\eta\nu_\tau$ branching fraction is measured by fitting the $\pi^+\pi^-\pi^0$ mass spectrum for events selected to contain $\tau \to K^-\pi^+\pi^-\pi^0\nu_\tau$ decays. This branching fraction has most recently been measured by the Belle Collaboration [16] but this will be the first analysis by the *BABAR* Collaboration.

A search for $\tau^- \to \pi^-\eta\nu_\tau$ decays is performed by fitting the $\pi^+\pi^-\pi^0$ mass spectrum for events selected to contain $\tau \to \pi^-\pi^+\pi^-\pi^0\nu_\tau$ decays. The $\tau^- \to \pi^-\eta\nu_\tau$ decay would be mediated by a second-class current and as such is predicted to have a branching fraction of order 10^{-5}, which no search has so far been sensitive enough to reach. The most sensitive search was performed by the CLEO Collaboration [17], which found no evidence for the decay. The larger statistics sample collected by *BABAR* may allow a search sensitive enough to observe a

second-class current for the first time.

Chapter 2 describes the main properties of the τ lepton and its decays and it introduces the theory of second-class currents. Chapter 3 describes the experimental apparatus of the PEP-II collider and the *BABAR* detector. Chapter 4 explains how the data collected by the *BABAR* detector are reconstructed into events and how the Monte Carlo events are simulated. Chapter 5 reports on a study of the π^0 detection efficiency at *BABAR*. Chapter 6 describes the selection of events containing $\tau \to K^-\pi^+\pi^-\pi^0\nu_\tau$ and $\tau \to \pi^-\pi^+\pi^-\pi^0\nu_\tau$ decays. Chapter 7 describes how the $\tau^- \to K^-\eta\nu_\tau$ branching fraction is measured and how decays of $\tau^- \to \pi^-\eta\nu_\tau$ are searched for. Chapter 8 provides a summary and conclusion for the results of the analysis.

Chapter 2

Theory

This thesis presents measurements of the $\tau^- \to \pi^- \eta \nu_\tau$ and $\tau^- \to K^- \eta \nu_\tau$ branching fractions and this chapter provides some of the basic theoretical background required to understand these decays. Section 2.1 introduces the quantum numbers which are used to classify mesons and which will be useful when discussing decays involving mesons. The basic properties of the τ lepton are introduced in section 2.2 while section 2.3 describes how $\tau^+\tau^-$ pairs are produced at e^+e^- experiments such as *BABAR*. The leptonic decays of the τ lepton are outlined in section 2.4 while section 2.5 describes the hadronic τ decays. Section 2.6 introduces the second-class current and provides an overview of searches for second-class currents in τ decays. Finally, section 2.7 outlines the motivation for the work presented in the following chapters.

2.1 Meson classification

Mesons are hadrons that are made up of quark-antiquark pairs, $q\overline{q}$, and they are classified by their quark content and by quantum numbers such as the total angular momentum (J) and parity (P). The total angular momentum is a combination of the intrinsic spin (S) and the orbital angular momentum (L) and can take any value from $|L - S|$ to $|L + S|$, in increments of 1. The total angular momentum of a system is a conserved quantum number in all interactions.

The parity operator, $\hat{P}$, reflects special coordinates through the origin so that (x, y, z) becomes $(-x, -y, -z)$. Eigenstates of the parity operator can have an eigenvalue of $P = +1$ (even parity) or $P = -1$ (odd parity). Parity is a multiplicative quantum number and the parity of a meson is related to the orbital

angular momentum by $P = (-1)^{L+1}$. The parity of a system is conserved in all interactions except the weak interaction.

Further quantum numbers are described in the following sections; strong isospin in section 2.1.1, C-parity in section 2.1.2 and G-parity in section 2.1.3.

2.1.1 Strong isospin

The concept of strong isospin, I, was introduced by Werner Heisenberg [18] in 1932, before the discovery of the quarks. It was observed that, although they had different electric charges, the proton and neutron had similar masses and similar interactions. It was therefore convenient to treat them as two states of the same particle, so they were classified as an isospin doublet. An isospin doublet (analogous to a spin doublet) comprises two states with the same isospin, $I = 1/2$, but different projections of this isospin, $I_z = +1/2$ and $-1/2$, which are assigned to the proton and neutron respectively.

As further particles were discovered they were assigned different isospin values. The pions, π^-, π^0 and π^+, form an isospin triplet with $I = 1$ and respective values of $I_z = -1, 0$ and $+1$. The kaons (K^-, $\overline{K}^0$) form an $I = 1/2$ doublet and the η meson is an $I = 0$ singlet state.

Once the quark model was understood, these properties were seen to be due to the constituent quarks. The up and down quarks have similar masses and the same strong interaction, and therefore form an isospin doublet. The heavier quarks have very different masses from each other and are therefore all classified as isospin singlets. The concept of isospin is useful because it is a conserved quantum number in strong interactions.

2.1.2 C-parity

The charge conjugation operator, $\hat{C}$, swaps particles with their anti-particles. Only neutral particles can be eigenstates of $\hat{C}$, such as a neutral $q\overline{q}$ meson. For a charge-conjugation eigenstate, $|\Psi\rangle$, of a $q\overline{q}$ system, the eigenvalue is called C-parity and is defined as $C = (-1)^{l+s}$, so that

$$\hat{C}|\Psi\rangle = (-1)^{l+s}|\Psi\rangle, \tag{2.1}$$

where l is the orbital angular momentum and s is the intrinsic spin angular momentum of the $q\overline{q}$ system.

The property of C-parity is conserved in strong and electromagnetic interactions but broken in weak interactions. As an example, the π^0 meson is an eigenstate of charge-conjugation because $\hat{C}|\pi^0\rangle = \pm|\pi^0\rangle$. To find the sign of the $\hat{C}$-eigenvalue (C-parity) it can be noted that the π^0 decays into two photons and photons have odd C-parity ($C = -1$). Since C-parity is a multiplicative quantum number, the π^0 must have even C-parity ($C = +1$), and therefore

$$\hat{C}|\pi^0\rangle = |\pi^0\rangle. \tag{2.2}$$

Similarly, the η meson is also an eigenstate of $\hat{C}$ with positive C-parity ($\hat{C}|\eta\rangle = |\eta\rangle$).

2.1.3 G-parity

For neutral and charged mesons, the concept of C-parity can be generalised to the concept of G-parity. The $\hat{G}$-operator is defined as a rotation of π radians around the y-axis of isospin space followed by charge conjugation:

$$\hat{G} = \hat{C}e^{i\pi\hat{I}_y}. \tag{2.3}$$

The eigenvalue of $\hat{G}$ is the G-parity, which is therefore given for a $q\overline{q}$ system by $G = (-1)^{l+s+I}$, so that that

$$\hat{G}|\Psi\rangle = (-1)^{l+s+I}|\Psi\rangle, \tag{2.4}$$

for some eigenstate, $|\Psi\rangle$, of $\hat{G}$, for a $q\overline{q}$ system.

For example, since the π^0 meson is in an eigenstate of $\hat{C}$ with even C-parity, it must be an eigenstate of $\hat{G}$ with odd G-parity ($G = -1$), so $\hat{G}|\pi^0\rangle = -|\pi^0\rangle$. The charged pion is not an eigenstate of $\hat{C}$ but it is an eigenstate of $\hat{G}$ because $\hat{G}|\pi^\pm\rangle = \pm|\pi^\pm\rangle$, although the eigenvalue is ambiguous (± 1). For convenience, the eigenvalue is chosen so that all members of the isospin triplet have the same G-parity as the neutral member. Therefore pions always have negative G-parity:

$$\hat{G}|\pi\rangle = -|\pi\rangle. \tag{2.5}$$

Since G-parity is a multiplicative quantum number, the G-parity of a meson which decays strongly into a system of n pions will be $(-1)^n$.

The concept of G-parity provides no information which is not already known from isospin invariance and charge conjugation, but it is a useful shorthand when considering the selection rules for decays of meson resonances. Strong interactions conserve G-parity because they are invariant under charge conjugation and rotations in strong isospin space, while electromagnetic and weak interactions can violate G-parity conservation.

Vector mesons such as ρ and ω decay by strong interactions, so conservation of G-parity dictates the number of pions in the dominant pion decay mode; 2π for the positive G-parity ρ and 3π for the negative G-parity ω. On the other hand the η meson has positive G-parity and decays by electromagnetic transitions. Parity conservation forbids the strong decay into 2π, leaving the G-violating decay into three pions as the most favoured possibility for pionic decay.

2.2 The τ lepton

The tau lepton (τ) is the heaviest charged lepton in the Standard Model [5], with a mass of 1776.84 ± 0.17 GeV/c^2 [15]. All three standard model charged leptons, the electron, muon and tau (e, μ and τ), have the same electroweak couplings but different masses. They each have a corresponding neutrino (ν_e, ν_μ and ν_τ) and all six of these leptons have a corresponding anti-lepton, assuming that neutrinos are Dirac particles.

The τ lepton is an unstable, point-like, spin-$\frac{1}{2}$ Dirac particle with a lifetime of $(290.6 \pm 1.0) \times 10^{-15}$ s [15]. It was discovered in 1975 by Martin Perl and the Stanford Linear Accelerator Center-Lawrence Berkeley Laboratories (SLAC-LBL) Collaboration, later called MARK I [14].

2.3 Production of $\tau^+\tau^-$ pairs

Figure 2.1 shows the lowest-order Feynman diagram for $\tau^+\tau^-$ production at electron-positron colliders. The process is mediated by the exchange of a photon or a Z boson, with interference occurring between the two processes.

The cross section for $e^+e^- \to \tau^+\tau^-$ is shown in figure 2.2 as a function of e^+e^- centre-of-mass (CM) energy, E_{CM}. The maximum cross section is seen at an energy just above the threshold for $\tau^+\tau^-$ production, and after that it decreases approximately as $1/E_{CM}$, with a large peak at the Z resonance mass.

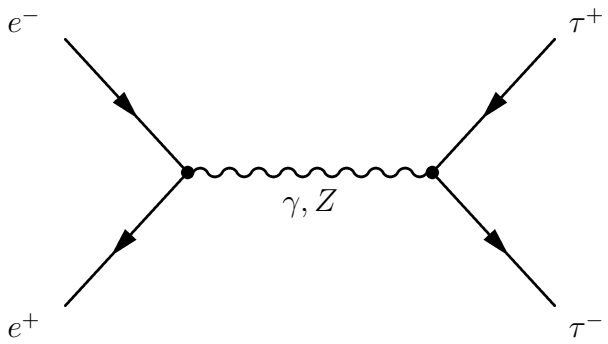

Figure 2.1: Feynman diagram of $\tau^+\tau^-$ production from e^+e^- annihilation through the exchange of a photon or Z boson.

The *BABAR* experiment uses an electron-positron collider, with a CM energy of 10.58 GeV. At this energy τ production is dominated by the exchange of photons so it is a reasonable approximation to ignore the γ-Z interference. The cross section (σ) for $e^+e^- \to \tau^+\tau^-$ is given to the lowest order by

$$\sigma_{\tau^+\tau^-}(s) = \frac{4\pi\alpha^2}{3s}\beta\frac{(3-\beta^2)}{2}F_c, \tag{2.6}$$

where s is the CM energy squared ($s = E_{CM}^2$), $\beta = \sqrt{1-4m_\tau^2/s}$ is the velocity of a τ in the CM frame and α is the electromagnetic coupling (fine structure) constant [20]. The Coulomb attraction between τ^+ and τ^- is accounted for by F_c where

$$F_c = \frac{\pi\alpha}{\beta(1-e^{-\pi\alpha/\beta})}. \tag{2.7}$$

The cross section at *BABAR* can be estimated using the *BABAR* CM energy of $\sqrt{s} = 10.58$ GeV, which gives $\sigma_{\tau^+\tau^-} = 0.94$ nb. However, the effect of initial-state radiation (when an electron or positron emits a photon before annihilation) also must be taken into account because it reduces the CM energy, thereby changing the $\tau^+\tau^-$ production cross section. Other corrections must be applied to the cross section to account for the physical effects of final-state radiation (photon radiation from the τ), beam energy spread, vacuum polarisation (quantum electrodynamic corrections to the photon propagator) and the interference with the Z boson. The size of each correction depends on the CM energy. The cross section for $e^+e^- \to \tau^+\tau^-$ at the energy of the *BABAR* experiment is calculated to be 0.919 ± 0.003 nb [21], which is used through the following chapters.

It is possible for τ leptons to be produced in the decays of certain D and B mesons; however the numbers produced are more than an order of magnitude

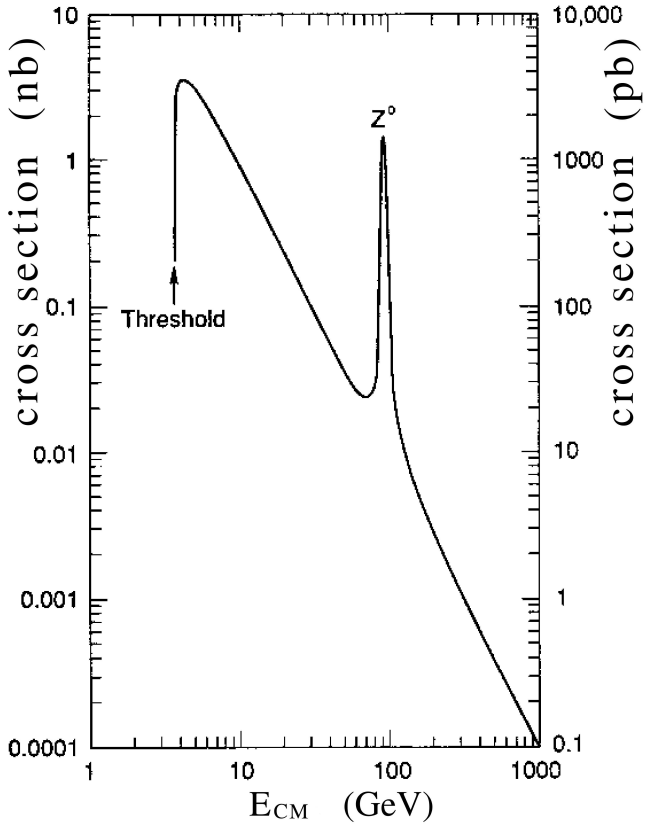

Figure 2.2: The cross section of τ pair production from e^+e^- annihilation, as a function of CM energy (from [19]).

lower than those produced by e^+e^- annihilation and usually only single τ leptons are produced by this process.

2.4 Leptonic decays of τ leptons

The τ lepton can decay leptonically, when the τ decays into a τ neutrino and an intermediate virtual $W^{\pm}$ vector boson which couples to a charged lepton and its corresponding anti-neutrino ($\tau^- \rightarrow l^- \overline{\nu_l} \nu_\tau$). The branching fraction for $\tau^- \rightarrow e^- \overline{\nu_e} \nu_\tau$ and $\tau^- \rightarrow \mu^- \overline{\nu_\mu} \nu_\tau$ (see table 2.2) are similar, although the muonic decay is slightly suppressed because the muon has a larger mass. A photon can also be emitted from any of the charged leptons, before or after the decay, and appear in the final state.

Lepton number is conserved in the Standard Model; lepton-flavour violating

decays involving charged leptons have never been observed and upper limits on their branching fractions have been measured at between 10^{-5} and 10^{-8} [15]. Leptonic τ decays which are allowed in the Standard Model but which have more than one charged lepton, or a charged lepton and hadrons, in the final state are heavily suppressed and have measured branching fractions of order 10^{-5} or less [15].

2.5 Hadronic decays of τ leptons

If a τ decays hadronically, as shown in figure 2.3, it couples to a τ neutrino and an intermediate virtual $W^{\pm}$ vector boson which in turn couples to a quark-antiquark pair. When the τ decays into a hadronic state in this way, there are various selection rules which explain why certain hadronic states are favoured.

2.5.1 Selection rules

The intermediate $W^{\pm}$ vector boson will only couple to quark-antiquark pairs with a total angular momentum, J, of 0 or 1. Since the neutrino is neutral, the hadrons must carry the same charge as the τ lepton.

Phase space suppression: The τ mass limits the hadronic states which can be produced. Baryons would have to be pair produced but any baryon-antibaryon pair is heavier than the τ, so only mesons are possible. Only lighter mesons, involving the three lightest quarks and antiquarks (u, d, s, $\overline{u}$, $\overline{d}$ and $\overline{s}$) are

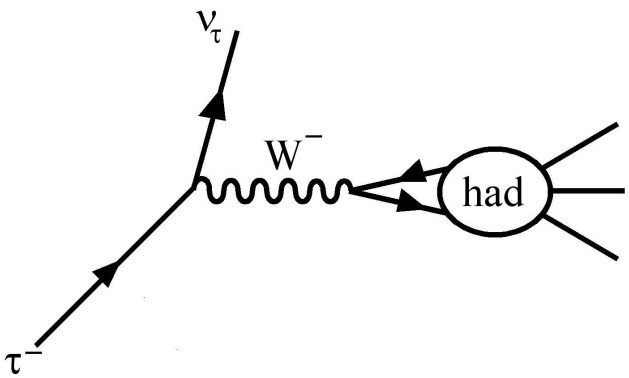

Figure 2.3: Diagram of a hadronic τ decay (from [20]).

produced, and the heavier strange particles suffer from a phase space suppression.

Cabibbo suppression: The intermediate $W^{\pm}$ boson will couple to a $d'\overline{u}$ quark pair, where d' is a mixture of d, s and b quarks, according to the Cabibbo-Kobayashi-Maskawa (CKM) matrix [1, 4]. The amplitude for the production of a $q_1\overline{q_2}$ pair is proportional to the V_{q1q2} element in the CKM matrix. The b quark is too heavy to be produced. The amplitude for the production of $d\overline{u}$ is proportional to $V_{ud} = 0.97418 \pm 0.00027$ and the amplitude for $s\overline{u}$ production is proportional to $V_{us} = 0.2255 \pm 0.0019$, as measured by experiments [15]. The decays which involve the production of strange quarks are therefore said to be Cabibbo suppressed.

Exotic states: Some combinations of J^{PG} quantum numbers cannot be produced by a quark-antiquark pair. Final states with these quantum numbers are called 'exotic' and are associated with objects which have not been observed experimentally, such as molecules ($qq\overline{qq}$) or hybrids (qqg).

Free quark model: The following selection rules are understood by describing hadronic τ decays in terms of free quarks. For the example of the τ decaying into a $d\overline{u}$ pair, a left-handed d quark and a right-handed $\overline{u}$ quark are emitted back-to-back in the rest frame of the intermediate $W^{\pm}$. If quarks were massless, their helicity would be the same as their chirality and a state of total spin-1 would necessarily arise. In fact, quarks are massive so the helicity and chirality eigenstate are no longer identical. This means that one of the quarks can have the 'wrong' helicity; a left-handed quark with a positive helicity or a right-handed quark with a negative helicity. In this case, the state will have a total spin of 0, as shown in figure 2.4. The amplitude for the production of $d\overline{u}$ quark pairs in a spin-0 state are helicity suppressed by a factor [20]:

$$\frac{m_d}{m_{had}} + \frac{m_u}{m_{had}} + \mathcal{O}\left(\frac{m_{d/u}^2}{m_{had}^2}\right), \tag{2.8}$$

where m_d and m_u are the masses of the d and $\overline{u}$ quarks, m_{had} is the mass of the $d\overline{u}$ hadron and $m_{d/u}$ is the average of m_d and m_u. All spin-0 final states of hadronic τ decays are helicity suppressed in this way.

The amplitude for the production of a spin-0 state can be further divided into

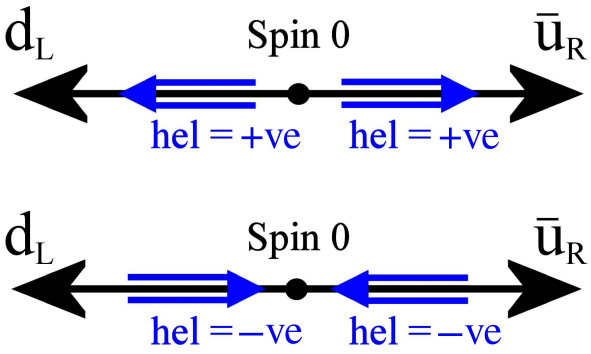

Figure 2.4: The two spin configurations leading to spin-0 hadrons in τ decays (from [20]). The helicity of a particle is defined to be positive if its spin (short arrow) is in the same direction as its motion (long arrow). A massless right-handed particle will always have positive helicity but if the particle has mass, as shown here, the helicity can be negative and a spin-0 state can be formed. The L and R subscripts refer to the left and right handedness of the chirality (rather than the helicity).

scalar ($J^P = 0^+$) and pseudoscalar ($J^P = 0^-$) components. The amplitude for the production of the pseudoscalar component is proportional to the sum of the quark masses (due to helicity suppression), but the amplitude for scalar states is suppressed further by the difference between the quark masses [20]. This is called 'isospin suppression' and in the limit of equal quark masses the amplitude for the production of scalar 0^+ states would vanish.

Current algebra: The previous selection rules have been described in a picture of free quarks, but at lower energies the quarks are strongly bound into mesons, so the hadronic τ decays can be described by a hadronic current coupling to the virtual $W^\pm$ boson. As shown in figure 2.5, the hadronic current comes from the vacuum to produce a hadronic final state. In fact, this picture gives the same pattern of branching fractions as the picture of free quarks.

The hadronic current includes a vector current ($J^P = 1^-$) and an axial-vector current ($J^P = 1^+$). It is observed that Fermi's constant G_F (which characterises the strength of the weak interaction) is the same for leptonic and hadronic weak interactions, which means that the strength of this coupling must not be affected by quantum-chromodynamic (QCD) corrections. This implies that the vector current is conserved [20]. However, a 'conserved vector current' (CVC) can only

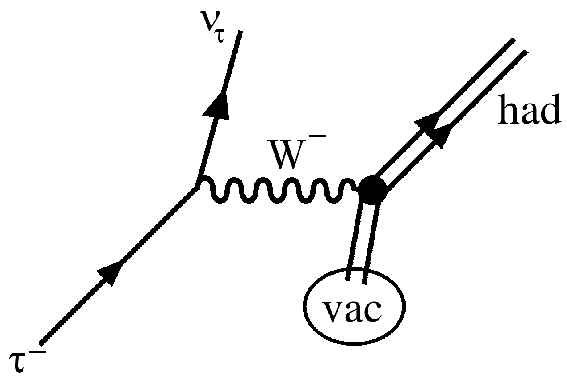

Figure 2.5: Diagram of meson creation through a hadronic current in τ decays. A hadronic current (had) comes from the vacuum (vac) and couples with a $W^{\pm}$ vector boson to produce a hadronic final state (from [20]).

exist if there is no scalar current present (no $J^P = 0^+$ final states). The vector current is completely conserved in the limit of equal quark masses, in which case the scalar current must vanish. Therefore, the $J^P = 0^+$ states are suppressed by a factor proportional to the difference in mass of the light quarks, which is what was described in the free quark model as isospin suppression.

Similarly, the coupling strength of nuclear β decays proceeding through an axial-vector current is similar (but not identical) to the coupling strength of leptonic weak interactions. This 'partially conserved axial-vector current' (PCAC) leads to what was described in the free quark model as helicity suppression. There is a suppressed pseudoscalar current ($J^P = 0^-$ final states) which vanishes in the limit of vanishing quark masses, where the conservation of the axial-vector current becomes exact.

Second-class currents: The final states of τ decays can be further classified according to their G-parity. For each J^P state, only one of the two possible values for G-parity has been observed; these are called first-class currents and have $J^{PG} = \{0^{++}, 0^{--}, 1^{+-}, 1^{-+}\}$. States with the opposite G-parity are called second-class currents and are heavily suppressed. Second-class currents are discussed in greater detail in section 2.6.

Non-strange decays					
J^{PG}	Helicity PCAC	Isospin CVC	Second class	Exotic	
0^{++}		x		x	
0^{+-}		x	x		$a_0(980)$
0^{-+}	x		x	x	
0^{--}	x				π
	x				$\pi(1300)$
1^{++}			x		$b_1(1235)$
1^{+-}					$a_1(1260)$
1^{-+}					$\rho(770)$
					$\rho(1450)$
					$\rho(1700)$
1^{--}			x	x	

Table 2.1: Summary of the non-strange hadronic final states accessible in τ decays and the selection rules which apply to them (as described in section 2.5.1). The final column specifies the accessible resonances but the same selection rules apply to non-resonant decays (taken from [20]).

2.5.2 Summary of selection rules and hadronic final states

In this section the final states which result from the selection rules above are examined. The quantum numbers of the possible hadronic states accessible in τ decays and the selection rules which apply to them are shown in table 2.1 for non-strange decays. For illustrative purposes, table 2.2 lists the experimentally measured values for some of the largest branching fractions for τ decays.

The final state of a hadronic τ decay must have an odd number of charged tracks to carry the charge of the τ. Most of the time the τ decays into a mode with a single charged particle.

The only two channels which have no suppression are $J^{PG} = 1^{-+}$ and 1^{+-}, which correspond to the $\tau^- \to \rho^-\nu_\tau$ and $\tau^- \to a_1(1260)^-\nu_\tau$ decays, and out of these two, phase space favours the ρ mode. To conserve positive G-parity, the ρ always decays into an even number of pions, predominantly $\pi^-\pi^0$. The $\tau^- \to \pi^-\pi^0\nu_\tau$ decay (which is dominated by the ρ resonance), has the largest branching fraction of any τ decay, as shown in table 2.2.

The $a_1(1260)$ resonance always decays into an odd number of pions, conserving negative G-parity. It predominantly produces a final state of three pions, through the intermediate states of $\rho^-\pi^0$ or $\rho^0\pi^-$, followed by $\rho \to \pi\pi$. The decays of

$\tau^- \rightarrow$	Fraction (Γ_i/Γ) (%)
$\pi^-\pi^0\nu_\tau$	25.51 ± 0.09
$\tau^- \rightarrow e^-\overline{\nu_e}\nu_\tau$	17.85 ± 0.05
$\tau^- \rightarrow \mu^-\overline{\nu_\mu}\nu_\tau$	17.36 ± 0.05
$\pi^-\nu_\tau$	10.91 ± 0.07
$2\pi^-\pi^+\nu_\tau(ex.K^0)$	9.03 ± 0.06
$\pi^-2\pi^0\nu_\tau(ex.K^0)$	9.29 ± 0.11
$2\pi^-\pi^+\pi^0\nu_\tau$	4.61 ± 0.06
$\pi^-\overline{K}^0\nu_\tau$	0.84 ± 0.04
$K^-\nu_\tau$	$0.696 \pm 0.023)$
$K^-\pi^0\nu_\tau$	0.429 ± 0.015
$K^-\pi^-\pi^+\pi^0\nu_\tau$	0.136 ± 0.014

Table 2.2: The branching fractions [15] of the most common τ decays and the decays which are selected in the following chapters. The first six decay modes in the table together account for $\sim$90% of τ decays.

$\tau^- \rightarrow 2\pi^-\pi^+$ and $\tau^- \rightarrow \pi^-2\pi^0$ have similar branching fractions as each other (as shown in table 2.2), and are dominated by the $a_1(1260)$ resonance.

Suffering only from helicity suppression, the third most common hadronic decay channel is 0^{--}, which corresponds to the $\tau^- \rightarrow \pi^-\nu_\tau$ decay. Compared to these three modes, all the other hadronic branching fractions are small. The $\tau^- \rightarrow 2\pi^-\pi^+\pi^0\nu_\tau$ decay is one of those that will be selected in the following chapters. This channel can take place through various intermediate states such as $\omega\pi^-$, $a_1\pi$, $\rho\rho$ and $\rho\pi\pi$. The different contributing resonances produce quantum mechanical interference in the mass spectra of the decay products.

Table 2.3 shows the strange hadronic final states which are accessible to the τ. These decays are all Cabibbo suppressed. The mass of the strange quark is significantly greater than the mass of the up or down quarks, which results in increased phase-space suppression, weaker helicity suppression, no isospin suppression and no G-parity classification.

In the strange decays, the $J^P = 1^-$ channel is the most favoured decay, which corresponds to the $\tau^- \rightarrow K^{*-}\nu_\tau$ decay and is the equivalent of the $\tau^- \rightarrow \rho^-\nu_\tau$ decay in the non-strange sector. The K^{*-} predominantly decays into the $\pi^-\overline{K}^0$ and π^0K^- final states, and dominates strange decays into two mesons. As shown in figure 2.2, $\tau^- \rightarrow \pi^-\overline{K}^0\nu_\tau$ has the largest branching fraction of any strange τ-decay while $\tau^- \rightarrow K^-\pi^0\nu_\tau$ has the third largest.

Strange decays			
J^P	Cabibbo	Helicity	
0^+	x	x	$K_0^*(800)$
0^+	x	x	$K_0^*(1430)$
0^-	x	x	K
1^+	x		$K_1(1270)$
	x		$K_1(1400)$
1^-	x		$K^*(892)$
	x		$K^*(1410)$
	x		$K^*(1680)$

Table 2.3: Summary of the Cabibbo suppressed hadronic final states accessible in τ decays and the selection rules (as described in section 2.5.1) which apply to them (taken from [20]).

The 0^- channel is not much less favoured, suffering from weak helicity suppression, and so the second most common strange decay is $\tau^- \to K^-\nu_\tau$. Most decays through the 1^+ and 0^+ channels are close to the limit of phase space and therefore have very small branching fractions. However, the Belle Collaboration recently found evidence for the $K_0^*(800)$ resonance [22] in $\tau^- \to K_S^0\pi^-\nu_\tau$ decays.

The $\tau^- \to K^-\pi^-\pi^+\pi^0\nu_\tau$ decay is the second mode which will be selected in the following chapters. This decay also takes place through various intermediate states, such as ωK^-, $K^*\pi\pi$ and ηK^-.

2.6 Second-class currents

The concept of second-class currents was first defined by Weinberg in 1958 [23] when he divided hadronic weak currents into two groups depending on their G-parity, parity and angular momentum. The first-class currents have $J^{PG} = 0^{++}, 0^{--}, 1^{+-}, 1^{-+}, ..,$ (i.e. $PG(-1)^J = +1$), and the second-class currents carry the opposite G-parity. So far, only first-class currents have been experimentally observed in weak decays. In the Standard Model, second-class currents are suppressed by a factor proportional to the mass difference between the up and down quarks, vanishing in the limit of perfect isospin symmetry.

The classification applies only to the weak vertex so subsequent decays may produce a second-class current because electromagnetic interactions, or the small mass difference between the quarks, can violate G-parity conservation.

2.6.1 Searches for second-class currents in τ decays

There have been many searches for second-class currents in nuclear β decays and muon capture by nuclei [24, 25], but there have been no confirmed signals. The τ lepton provides a clean way to search for second-class currents, through the decay modes:

$$\tau^- \to \eta\pi^-\nu_\tau, \tag{2.9}$$

$$\tau^- \to \eta'(958)\pi^-\nu_\tau \tag{2.10}$$

and

$$\tau^- \to b_1(1235)^-\nu_\tau. \tag{2.11}$$

The $\eta\pi^-$ final state can only be produced through a second-class current, regardless of the intermediate resonance. The η has positive G-parity while the pion has negative G-parity, and both have an intrinsic angular momentum of 0, with negative parity. The overall parity for the $\eta\pi^-$ state is therefore $(-1)^L$ where L is the orbital angular momentum which can have the values $L = 0$ or 1, while the overall G-parity is negative. Consequently, an $\eta\pi^-$ system with $J = 0$ will have $J^{PG} = 0^{+-}$ which is a second-class current and can be mediated by the $a_0^-(980)$ resonance. An $\eta\pi^-$ system with $J = 1$ will have $J^{PG} = 1^{--}$, which is also a second-class current. In the same way, the $\eta(958)'\pi^-$ final state can also only be produced through a second class current, with $J^{PG} = 1^{--}$ or 0^{+-}.

The $b_1(1235)^-$ resonance decays predominantly into $\omega\pi^-$, but the $\omega\pi$ final state can also be produced by a first-class vector current. The s- and d-wave contributions (orbital angular momentum $L = 0$ and 2) to the $\tau^- \to \pi^-\omega\nu_\tau$ decay produce a final state with $J^{PG} = 1^{++}$, which is a second-class current mediated by the $b_1(1235)$ resonance. The p-wave contribution ($L = 1$) can be produced by a $J^{PG} = 0^{-+}$ final state, which is a second-class current, or a $J^{PG} = 1^{-+}$ final vector state, which is a first-class current mediated by the ρ resonance.

Precise estimates of the likely branching fractions are difficult but order of magnitude estimations can be made. The branching fraction of $\tau^- \to a_0^-(980)\nu_\tau$ is expected to be suppressed by a factor of 10^{-4} with respect to $\tau^- \to \pi^-\nu_\tau$ (π has $J^{PG} = 0^{--}$ while $a_0(980)$ has $J^{PG} = 0^{-+}$). Therefore, $\tau^- \to \pi^-\eta\nu_\tau$ decays in a $J^{PG} = 0^{+-}$ state are expected to have branching fractions of order 10^{-5} [26–28]. Decays of $\tau^- \to \pi^-\eta\nu_\tau$ in a $J^{PG} = 1^{--}$ state are expected to be further suppressed, with a branching fraction of order 10^{-6} [26].

A rough estimate of the $\tau^- \to b_1^-(1235)\nu_\tau$ branching fraction can be obtained

by assuming that the suppression factor is similar to that in the $a_0(980)$ case above. By analogy, the branching fraction of $\tau^- \to b_1^-(1235)\nu_\tau$ is expected to be suppressed by the same factor of 10^{-4} with respect to $\tau^- \to a_1^-(1260)\nu_\tau$ ($a_1(1260)$ has $J^{PG} = 1^{+-}$ while $b_1(1235)$ has $J^{PG} = 1^{++}$). This provides an expected branching fraction of order 10^{-5} for the $\tau^- \to b_1^-(1235)\nu_\tau$ decay [29].

The best upper limit on the production of $\tau^- \to \pi^-\eta\nu_\tau$ decays has been made by the CLEO Collaboration [17]. They selected events where the η meson decayed into two photons, which amounts to ∼40% of its total branching ratio. They observed no $\tau^- \to \pi^-\eta\nu_\tau$ signal and found the limit on the branching fraction to be

$$\mathcal{B}(\tau^- \to \pi^-\eta\nu_\tau) < 1.4 \times 10^{-4} \tag{2.12}$$

at the 95% confidence level.

The *BABAR* Collaboration have set an upper limit on the branching fraction of $\tau^- \to \eta'(958)\pi^-\nu_\tau$, with $\eta' \to \eta\pi^+\pi^-$. It is found to be

$$\mathcal{B}(\tau^- \to \eta'(958)\pi^-\nu_\tau) < 7.2 \times 10^{-6} \tag{2.13}$$

at the 90% confidence level [30].

Limits on the second-class current contribution to the $\tau^- \to \pi^-\omega\nu_\tau$ have been obtained by the ALEPH [31], CLEO [32] and *BABAR* Collaborations [33]. They select $\tau^- \to \pi^-\omega\nu_\tau$ events using the dominant $\omega \to \pi^+\pi^-\pi^0$ decay mode and calculate the angle, θ, between the normal to the $\omega \to \pi^+\pi^-\pi^0$ decay plane and the direction of the remaining π^- in the ω rest frame. The distribution of $\cos\theta$ is different for the first and second class components, due to the different angular momentum of each, as discussed above. Therefore, $\cos\theta$ is used to distinguish the first-class vector current p-wave contribution from the second-class current contributions. All analyses have found that the distribution of $\cos\theta$ is consistent with a pure vector current, showing no evidence of a second-class current. The most stringent upper limit on the second-class contribution to this mode is 0.69% at the 90% confidence level, as measured by the *BABAR* Collaboration [33]. Using the $\tau^- \to \pi^-\omega\nu_\tau$ branching fraction [15] this corresponds to an upper limit of

$$\mathcal{B}(\tau^- \to \omega\pi^-\nu_\tau(SCC)) < 1.3 \times 10^{-4} \tag{2.14}$$

at the 90% confidence level, on the second-class current (SCC), non-vector contribution.

2.7 Motivation for this thesis

The *BABAR* Collaboration has recorded a dataset containing 432 million $\tau^+\tau^-$ pairs, over a hundred times the sample that was available to the CLEO Collaboration, who previously set the best upper limit on the $\tau^- \to \pi^-\eta\nu_\tau$ branching fraction. Therefore an improvement on this limit may be possible with the larger *BABAR* dataset. The *BABAR* Collaboration has already set the most stringent upper limit on $\tau \to \eta'\pi\nu_\tau$ decays and the second-class current contribution to $\tau^- \to \pi^-\omega\nu_\tau$ decays, so $\tau^- \to \pi^-\eta\nu_\tau$ is the last of the second-class current modes discussed above to be studied by the *BABAR* Collaboration.

This thesis will also describe a measurement of the $\tau^- \to K^-\eta\nu_\tau$ branching fraction. This measurement can be made in a similar way to the $\tau^- \to \pi^-\eta\nu_\tau$ search, by selecting a kaon in the final state instead of a pion. It is useful to have an accurate measurement of the $\tau^- \to K^-\eta\nu_\tau$ branching fraction because the CKM matrix element $|V_{us}|$ can be determined from the strange hadronic τ decays [34].

The $\tau^- \to K^-\eta\nu_\tau$ branching fraction has previously been measured by the CLEO [17], ALEPH [31] and Belle [16] Collaborations, giving a world average [15] of

$$\mathcal{B}(\tau^- \to K^-\eta\nu_\tau) = (1.61 \pm 0.11) \times 10^{-4}. \tag{2.15}$$

The most recent measurement by the Belle Collaboration found the $\tau^- \to K^-\eta\nu_\tau$ branching fraction to be $(1.58 \pm 0.10) \times 10^{-4}$ [16], which is lower than the previous world average of $(2.7 \pm 0.6) \times 10^{-4}$ from the CLEO [17] and ALEPH [31] results (and the other branching fractions reported in [16] are also lower than previous measurements). The Belle Collaboration say that the difference may be due to the fact that the previous low statistics results had insufficient sensitivity to accurately judge the background contributions, resulting in an underestimation of the background contamination. A measurement of this branching fraction by the *BABAR* Collaboration can help to clarify the situation. This will be the first measurement of the $\tau^- \to K^-\eta\nu_\tau$ branching fraction by the *BABAR* Collaboration.

Chapter 3

The *BABAR* experiment

The *BABAR* detector collected data between October 1999 and April 2008, with the primary aim of measuring CP violation in the decay of neutral B mesons. It was situated at the SLAC National Accelerator Laboratory in California, on the Positron Electron Project II (PEP-II) storage rings, an asymmetric e^+e^- collider which ran at and around the $\Upsilon(4S)$ resonance. Although designed primarily for B physics, the experiment also produced large samples of τ leptons and charm mesons allowing a large secondary physics program in these areas and others.

Section 3.1 describes the main features of PEP-II. An overview of the *BABAR* detector is presented in section 3.2 with the following sections (3.3 to 3.8) detailing the individual subsystems of the detector. Finally, section 3.9 describes how the trigger system selects data to be recorded. Further details can be found in [35].

3.1 PEP-II storage rings

Electrons are produced by an electron gun and the positrons are produced by colliding electrons with a tungsten target to produce e^+e^- pairs. These are accelerated by the 2 mile long linear accelerator which injects into the 1.4 mile circumference PEP-II storage rings, as shown in figure 3.1.

The electrons are stored in the high energy ring (HER) at an energy of 9 GeV while the positrons are stored at an energy of 3.1 GeV in the low energy ring (LER). This produces a CM energy ($\sqrt{s}$) of 10.58 GeV for the e^+e^- collisions, corresponding to the mass of the $\Upsilon(4S)$ resonance.

The $\Upsilon(4S)$ resonance decays exclusively into $B^0\overline{B}^0$ and B^+B^- pairs, providing the large sample of B mesons required for the physics goals. The collision products

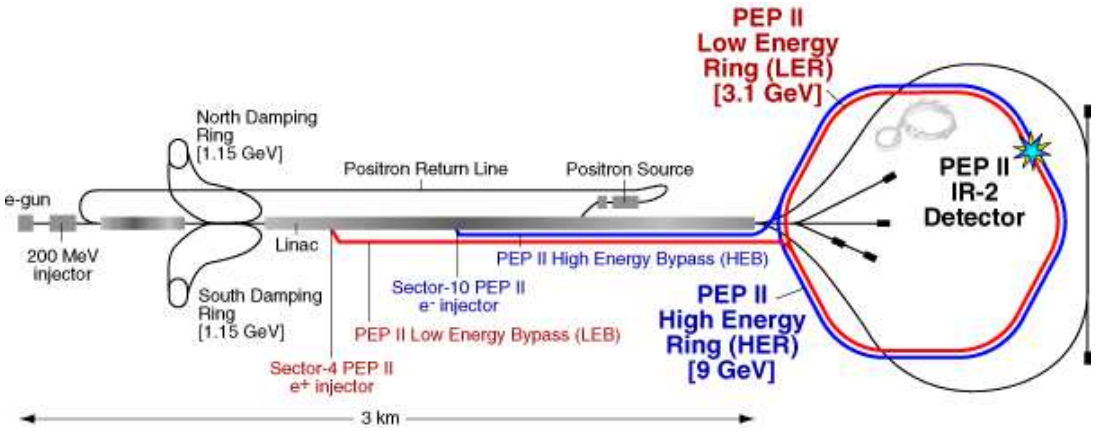

Figure 3.1: Diagram of SLAC illustrating the linear accelerator and the PEP-II storage rings. The *BABAR* detector is at the second interaction region on PEP-II (IR-2) (from [36]).

experience a Lorentz boost of $\beta\gamma = 0.56$ in the laboratory frame which means that the two B mesons may travel a measurable distance ($\sim$250 μm) before decaying. This allows the determination of their relative decay times which enables an analysis of CP violation.

As well as producing many $B\overline{B}$ pairs, running at $\sqrt{s} = 10.58$ GeV produces many pairs of τ leptons and charm mesons. Cross sections for various physics processes are given in table 3.1.

$e^+e^- \rightarrow$	cross section (nb)
$b\bar{b}$	1.05
$c\bar{c}$	1.30
$s\bar{s}$	0.35
$u\bar{u}$	1.39
$d\bar{d}$	0.35
$\tau^+\tau^-$	0.92
$\mu^+\mu^-$	1.16
e^+e^-	$\sim$40

Table 3.1: Physics cross sections at *BABAR* [21, 37].

A small subset of off-resonance (off-peak) data is also taken approximately 40 MeV below the $\Upsilon(4S)$ resonance, below the production threshold for $B\overline{B}$. This is used to study non-$B\overline{B}$ background events for the B physics analyses. Towards

the end of the experiment PEP-II ran at the $\Upsilon(3S)$ and $\Upsilon(2S)$ resonances.

During the running of the experiment, PEP-II delivered an integrated luminosity of 557 fb^{-1}, as shown in figure 3.2. The *BABAR* experiment recorded 96% of this integrated luminosity. The design luminosity of 3.0×10^{33} $\text{cm}^{-2}\text{s}^{-1}$ for the accelerator was surpassed in October 2000. The maximum luminosity achieved was 12.069×10^{33} $\text{cm}^{-2}\text{s}^{-1}$, on August 16th 2006.

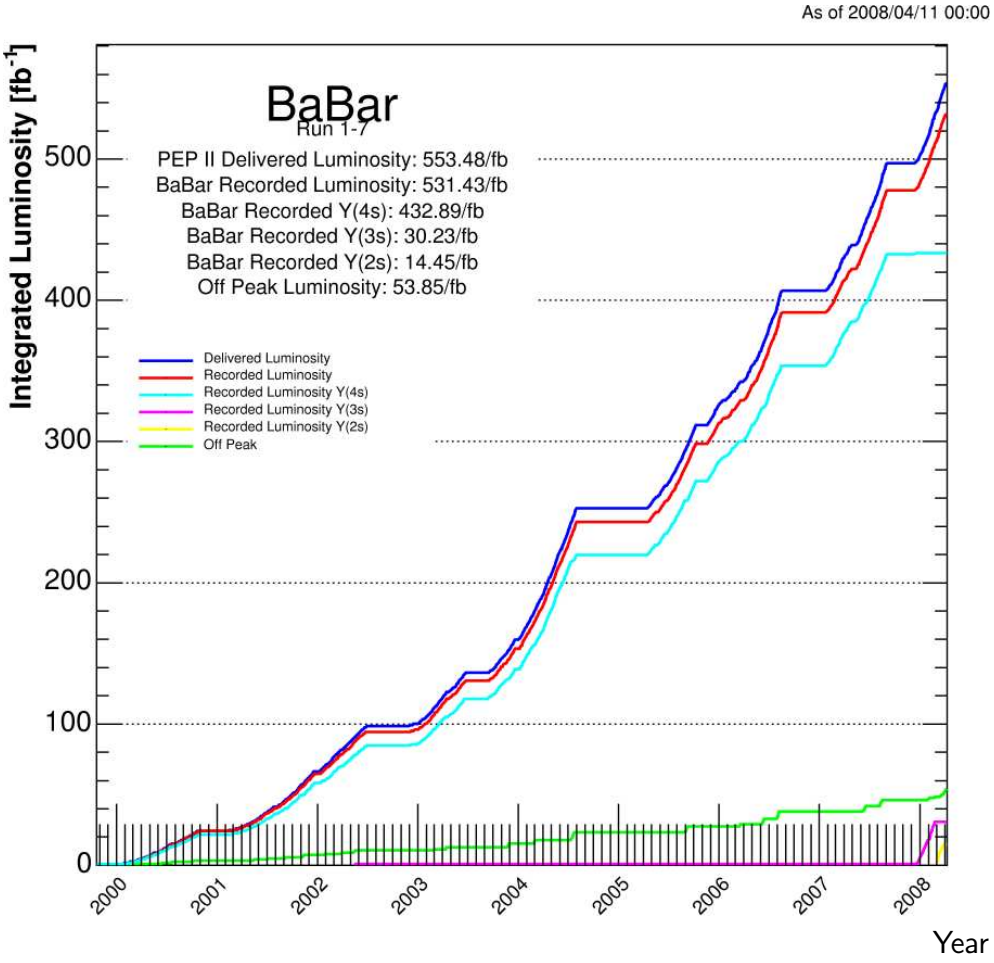

Figure 3.2: Integrated luminosity over the lifetime of the *BABAR* experiment [38].

3.2 Overview of the *BABAR* detector

The *BABAR* physics program requires that the detector has a large and uniform acceptance, especially in the boost direction. It must also have relatively good momentum and vertex resolution. The reconstruction efficiency is important for

charged particles down to 60 MeV/c and for photons down to 20 MeV. The energy and angular resolution are important for photons with an energy between 20 MeV and 2 GeV. There must be efficient and accurate identification of electrons, muons and hadrons.

The detector is made up of several subsystems, as shown in figures 3.3 and 3.4. Starting nearest the beam pipe and working outwards these systems are:

- The silicon vertex tracker (SVT)
- The drift chamber (DCH)
- The ring-imaging Cherenkov detector (DIRC)
- The electromagnetic calorimeter (EMC)
- The superconducting solenoid
- The instrumented flux return (IFR)

The design of each subsystem is driven by the requirements of the physics measurements. Sections 3.3 to 3.8 outline what these requirements are for each subsystem and describe the resulting design.

The SVT and the DCH together make the charged particle tracking system which provides measurements of momentum because it is within the magnetic field of the solenoid. It also measures the ionization loss for charged particles, which helps with particle identification. The DIRC identifies and distinguishes between pions and kaons. The EMC measures the energy of electromagnetic showers allowing it to identify and measure the energy of photons, electrons, π^0 and η mesons. The instrumented flux return identifies muons and K_L^0 hadrons.

The entire detector is offset relative to the interaction point (IP) by 0.37 m in the direction of the lower energy beam in order to contain the Lorentz boosted particles, and some of the individual subsystems also differ in the forward and backward direction for the same reason.

Each subsystem must be able to tolerate significant radiation and high levels of backgrounds, and the components must be robust and reliable as access to much of the detector is difficult. Both end doors of the IFR and the endcap of the EMC are split vertically so that they can open up to give access to some inner components.

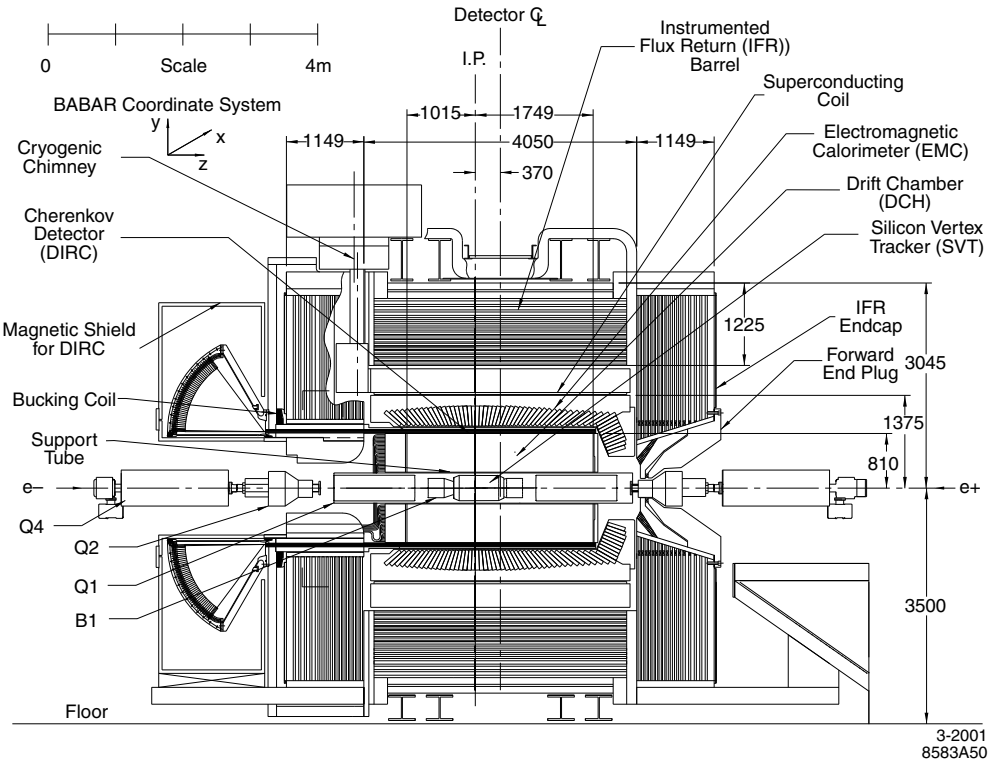

Figure 3.3: Longitudinal section of the *BABAR* detector. Distances are in mm and the components are described in the text (from [35]).

Once the data are taken the trigger system must select the physics events required to achieve the physics goals and reject background events, both with well understood efficiencies. This is done in two sequential stages using information from the DCH, EMC and IFR.

3.2.1 The *BABAR* coordinate system

An orthogonal coordinate system is used to describe the *BABAR* detector. The system is right-handed, with the z-axis aligned to the direction of the magnetic field from the solenoid, pointing in the direction of travel of the electrons. The y-axis points vertically up while the x-axis points horizontally away from the centre of the PEP-II rings. Spherical coordinates are also used, with $\theta = 0$ being on the positive z-axis and $\phi = 0$ on the positive x-axis.

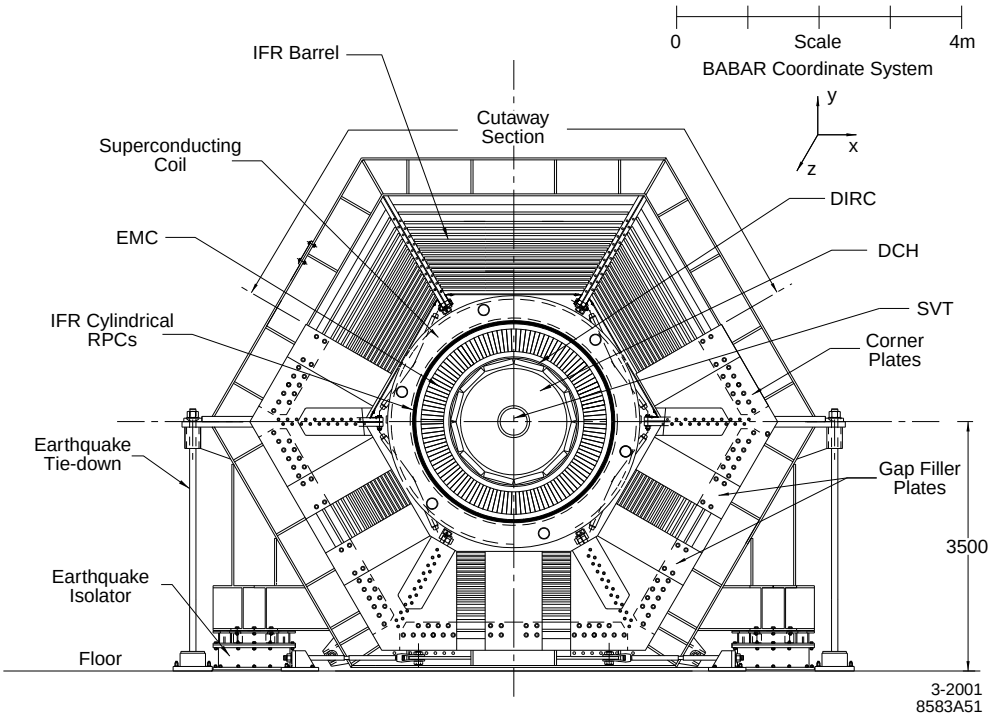

Figure 3.4: Transverse section of the *BABAR* detector. Distances are in mm and the components are described in the text (from [35]).

3.2.2 The PEP-II interaction region

The interaction region has a complex formation of magnets, as shown in figure 3.5. The requirements of asymmetric beam energies and large numbers of closely spaced bunches greatly affects the design of the interaction region.

In order to achieve the required high luminosities, the quadrupole magnets, QF/QD 1-5, tightly focus the beams at the IP. The beams must collide head-on at the IP but immediately separate afterwards to avoid secondary collisions. This is achieved with separation dipole magnets, B1, placed close to the IP to displace the beams horizontally.

The disadvantage of this arrangement is that the B1 dipole magnets and the Q1 quadrupole magnets are within the detector volume. These magnets cause synchrotron radiation as they accelerate the electrons and positrons, leading to one major source of beam induced background. This background is reduced by designing the interaction region to channel the radiation away from the detector and by installing copper masks to stop the radiation interacting with the beam pipe.

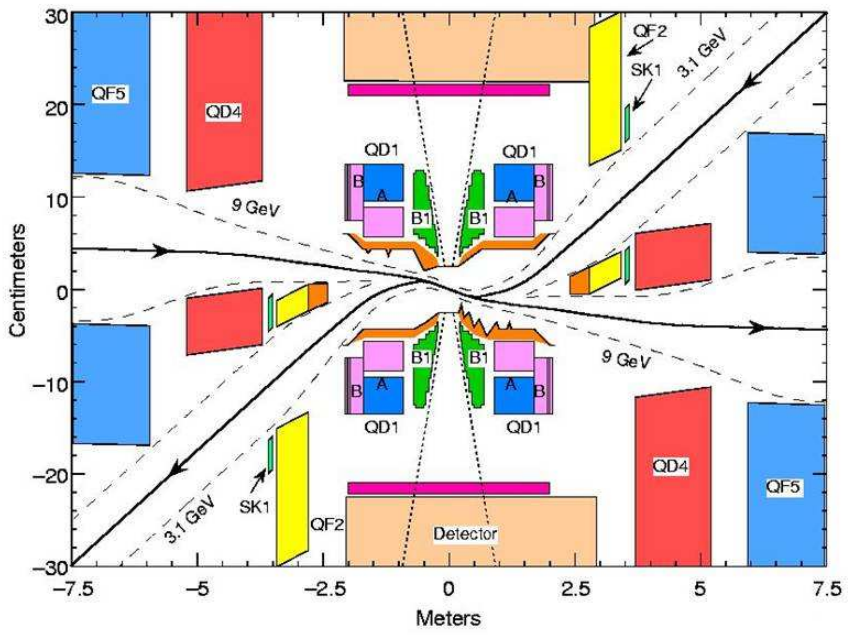

Figure 3.5: Diagram of interaction region showing focusing magnets QF/QD 1-5 and the B1 separation magnets (from [39]).

Another major source of beam induced background is beam-gas scattering, where beam particles lose energy through bremsstrahlung and Coulomb scattering with gas molecules in the beam pipe. With a lower energy, these 'lost' particles are deflected different amounts by the magnets and can interact with the beam pipe causing electromagnetic showers. This background is reduced by maintaining a low average pressure of order 10^{-10} torr in the beam pipe and by installing collimators upstream from the detector.

The final major source of beam background is radiative Bhabha scattering of beam particles at the IP. The resulting energy-degraded particles can interact with the beam pipe, causing electromagnetic showers within a few metres of the IP. This background is directly proportional to the luminosity. In addition there are other sources of background, such as beam-losses or interactions with dust particles in the beam pipe, which can disrupt stable operations.

3.3 Silicon vertex tracker (SVT)

The SVT uses silicon strip sensors to precisely reconstruct the trajectories and decay vertices of charged particles near the interaction point.

3.3.1 The charged particle tracking system

The SVT and DCH are complementary subsystems which make up the *BABAR* charged particle tracking system. The purpose of this system is to efficiently detect charged particles, making accurate position measurements which are reconstructed into 'tracks'. These measurements are essential for reconstructing decay vertices and for extrapolating to other subsystems. The tracking system is inside a 1.5 T magnetic field so the track curvatures also provide the particle momentum. The tracking system also measures the energy lost by ionization ($\mathrm{d}E/\mathrm{d}x$) which assists with particle identification (as explained in section 3.4).

3.3.2 Purpose and requirements of the SVT

The SVT is critical for vertex reconstruction near the IP. For the measurement of CP violation, two B decay vertices must be resolved, creating the requirement that the mean vertex resolution along the z-axis (for a fully reconstructed B meson) must be better than 80 μm. Reconstructing the final states in B, τ and charm decays requires that the resolution in the x-y plane be of order $\sim$100 μm.

The SVT must be able to provide standalone tracking for particles with transverse momentum (p_t) less than 120 MeV/c, as this is the minimum momentum that the DCH can reliably measure alone. Low transverse momentum is a feature of many B meson decay products, as well as slow pions from D_s^- meson decays. It is therefore important to have a tracking efficiency of 70% or more for tracks with transverse momentum between 50-120 MeV/c.

The SVT is important in providing the measurements of track angles, which are critical for the DIRC because the uncertainties in the charged particle track parameters are added to the uncertainty in the measurement of the Cherenkov angle (which is measured by the DIRC).

The SVT helps with particle identification by measuring $\mathrm{d}E/\mathrm{d}x$. It can achieve a 2σ separation between kaons and pions up to a momentum of 500 MeV/c, and between kaons and protons up to a momentum of 1 GeV/c.

Reliability is essential because the SVT it is inaccessible during normal detector operations, so components must be robust and redundancies are built in wherever practical. It must be able to withstand 2 Mrad of absorbed ionizing radiation and operate in a magnetic field of 1.5 T. Optimising the angular coverage of the SVT is important and the relative position of individual silicon sensors should be stable over long time periods in order to achieve the position resolution necessary to perform physics analyses.

3.3.3 Design of the SVT

The SVT consists of 5 layers of double-sided, 300 μm thick, silicon strip sensors. The strips on each side of the sensors are aligned perpendicular to each other, giving ϕ and z coordinates. The sensors are organised into modules arranged in 5 concentric layers, as shown in figures 3.6 and 3.7, resulting in a total active silicon area of 0.96 m^2.

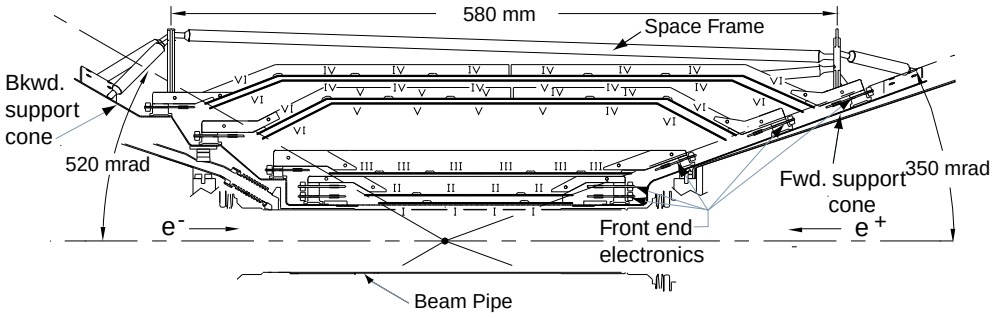

Figure 3.6: Schematic longitudinal section of the SVT (from [35]).

The three inner layers provide angle and position information for the measurement of the vertex position. In order to minimise the effect of multiple scattering in the beam pipe, these layers are mounted as close to the beam pipe as possible, with the innermost layer only 32 mm from the IP. To fulfil the physics requirements, the spatial resolution for perpendicular tracks is 10-15 μm. These layers each have 6 straight modules which are tilted by 5° in ϕ to allow an overlap between adjacent modules. This provides full azimuthal coverage and is advantageous for alignment.

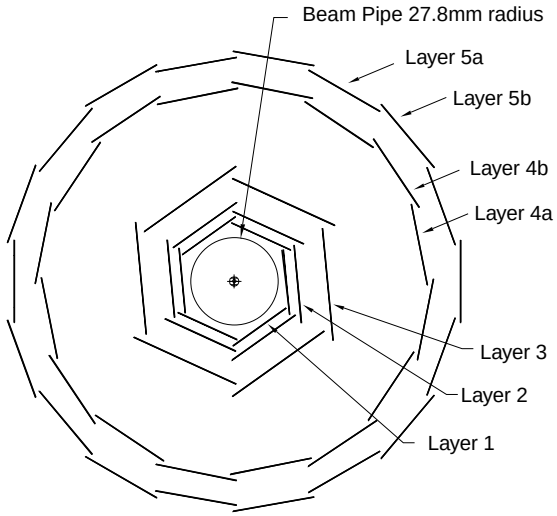

Figure 3.7: Schematic transverse section of the SVT showing how the silicon strip modules are arranged into layers (from [35]).

The outer two layers provide position and angle measurements to link the tracks with the DCH measurements and they are necessary for pattern recognition and low p_t tracking. The spatial resolution for perpendicular tracks in these outer layers is $\sim$40 μm. There are 16 modules in one layer and 18 in the other, all of which are placed at radii between 91 mm and 144 mm from the IP. The modules are arch-shaped, rather than straight, minimising the amount of silicon required to cover the solid angle. However, this means they can not be tilted in ϕ so, to avoid gaps, they are each divided into two sub-layers (a and b) which are placed at slightly different radii.

To optimise the angular coverage, the SVT extends down to 20° in the polar angle from the beam line in the forward direction, and down to 30° in the backward direction. This is limited by the B1 dipole magnets which occupy the region at smaller polar angles. The readout electronics are mounted entirely outside the active detector volume to minimise the material within the acceptance of the detector.

3.4 Drift chamber (DCH)

The function of the DCH is to detect charged particles and measure their momenta and angles. It contains drift cells which provide up to 40 spatial and ion-

ization loss measurements for charged particles with transverse momenta greater than 180 MeV/c.

3.4.1 Purpose and requirements of the DCH

The DCH and the SVT make up the charged particle tracking system which is described in section 3.3.1, with the DCH measurements complementing the SVT measurements near the IP. Decays and interactions which occur outside the SVT volume, such as the K_S^0 decays, must have their interaction vertices reconstructed entirely by the DCH. Therefore, the DCH was designed to be able to measure transverse positions and momenta, as well as longitudinal positions, with a resolution of $\sim$1 mm. The DCH measurements are important for matching the tracks to the signals seen in other subsystems and they also provide the only tracking information available to the trigger system.

The DCH complements the DIRC by providing additional particle identification information for low momentum particles. In the extreme backward and forward directions, outside the acceptance of the DIRC, the DCH provides the only particle identification. It does this by measuring the energy lost by ionization ($\mathrm{d}E/\mathrm{d}x$), which is derived from the measurement of total charge deposited in each drift cell. The type of particle can be determined by the relationship between the value of $\mathrm{d}E/\mathrm{d}x$ and the momentum, as seen in figure 3.8. A $\mathrm{d}E/\mathrm{d}x$ resolution of $\sim$7% allows π/K separation up to a momentum of 700 MeV/c.

There must be as little material in front of and inside the DCH volume as possible, in order to reduce multiple scattering, which is a significant limitation on the track parameter resolution. This is especially important for B-decays where the charged particles produced have an average momentum of less than 1 GeV/c. The track parameter resolutions are not critical for τ decays since, due to the presence of one or more neutrinos, the event cannot be fully reconstructed. Finally, the DCH must operate in the presence of a 1.5 T magnetic field and large beam-generated backgrounds.

3.4.2 Design of the DCH

The DCH is $\sim$0.8 m in diameter and nearly 3 m in length, as shown in figure 3.9. The centre is offset by 370 mm from the IP so that particles with polar angles between 17.2° and 152.6° traverse at least half of the layers of the chamber before

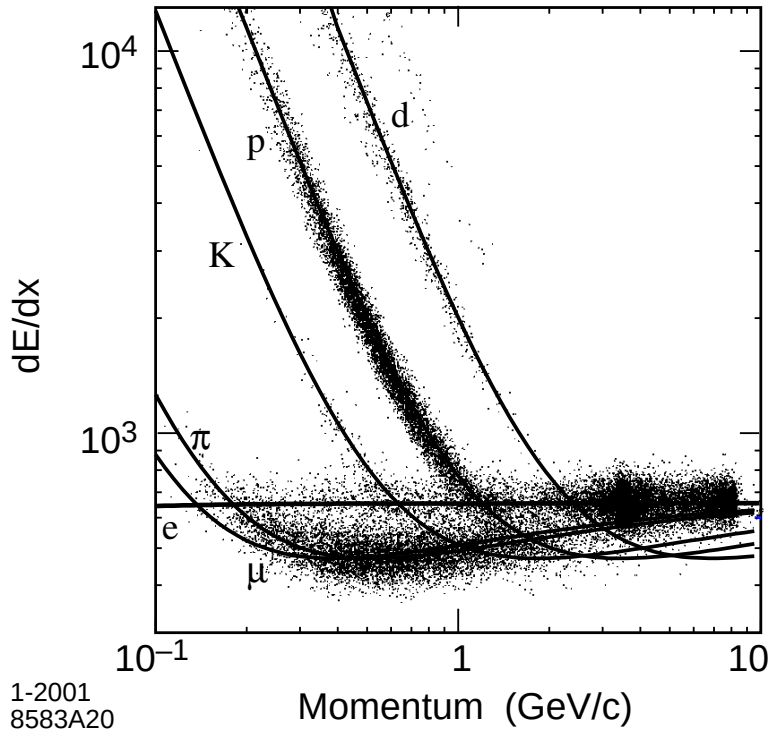

Figure 3.8: Measurement of $\mathrm{d}E/\mathrm{d}x$ in the DCH against track momenta. The superimposed Bethe-Bloch curves for particles of different masses have been determined from selected control samples. The large number of protons and deuterons come from beam-background events (from [35]).

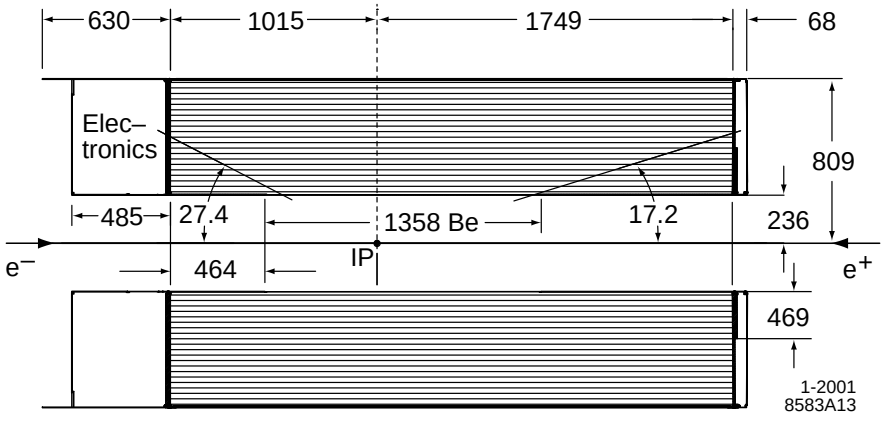

Figure 3.9: Longitudinal section of the DCH with dimensions in mm (from [35]).

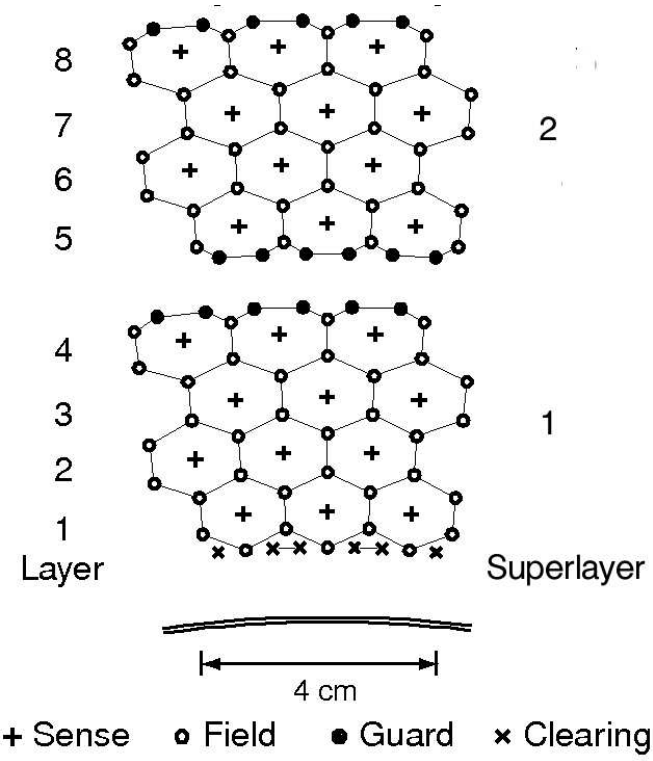

Figure 3.10: Schematic layout of drift cells for the 8 innermost layers (grouped in 2 superlayers). Lines have been added to aid the visualisation of cell boundaries. The four different types of wire are described in the text (from [35]).

exiting.

The inner cylindrical walls of the DCH are kept thin to help match up SVT and DCH tracks, to improve the resolution for high momentum tracks and to reduce the background from photon conversions and other interactions within the DCH walls. The outer wall is also kept thin so as not to degrade the performance of the DIRC or EMC. Therefore the high-voltage distribution and the readout electronics are mounted on the backward endplate of the chamber.

Inside the DCH there are 7104 hexagonal drift cells which are filled with a helium-based gas mixture, the atoms of which ionize when a charged particle passes through. Individual cells are 11.9 mm long in the radial direction and approximately 19.0 mm along the azimuthal direction. Each consists of one sense wire surrounded by six field wires, as shown in figure 3.10. In normal operation a voltage of 1960 V is applied to the sense wire, which is made of tungsten-rhenium with a width of 20 μm and a tension of 30 g. The field wires are made

of aluminium, with a diameter of 120 μm and a tension of 155 g (to match the gravitational sag of the sense wire), and are kept at ground potential.

The drift cells are arranged into 40 layers, which are grouped into 10 superlayers (4 layers per superlayer). Longitudinal position information is obtained by aligning the wires in 24 of the layers at small angles with respect to the z-axis. Sequential layers are staggered by half a cell, enabling left-right ambiguity resolution within a superlayer, even if one of the four signals is missing.

For cells at the boundary of a superlayer, two guard wires are added to improve the electrostatic performance of the cell. Finally, at the innermost boundary of layer 1 and the outermost boundary of layer 40, two clearing wires per cell are added to collect charges created by photon conversions in the wall material.

3.5 DIRC

The DIRC acronym stands for Detector of Internally Reflected Cherenkov radiation. The DIRC uses the properties of Cherenkov light and total internal reflection to provide separation of pions and kaons.

3.5.1 Purpose and requirements of the DIRC

When high energy charged particles pass through a radiator material faster than the speed of light in the material they emit Cherenkov radiation at an angle θ_c, called the Cherenkov angle. The Cherenkov angle depends on the velocity, v, of the particle and the refractive index, n, of the radiator material according to the relation

$$\cos\theta_c = \frac{1}{n\beta}, \tag{3.1}$$

where $\beta = v/c$ and c is the velocity of light. The relationship between the Cherenkov angle (measured by the DIRC) and the particle momentum (measured by the tracking system) depends on the particle mass, as illustrated by figure 3.11, and is therefore used to distinguish between pions and kaons.

There are many analyses at *BABAR* that require the separation of pions and kaons. The τ analysis described in chapter 7 requires pion and kaon identification for background rejection and signal selection. Also, the study of CP violation requires the ability to tag the flavour of one of the B mesons, using kaons which have momenta up to $\sim$2 GeV/c, while fully reconstructing the second.

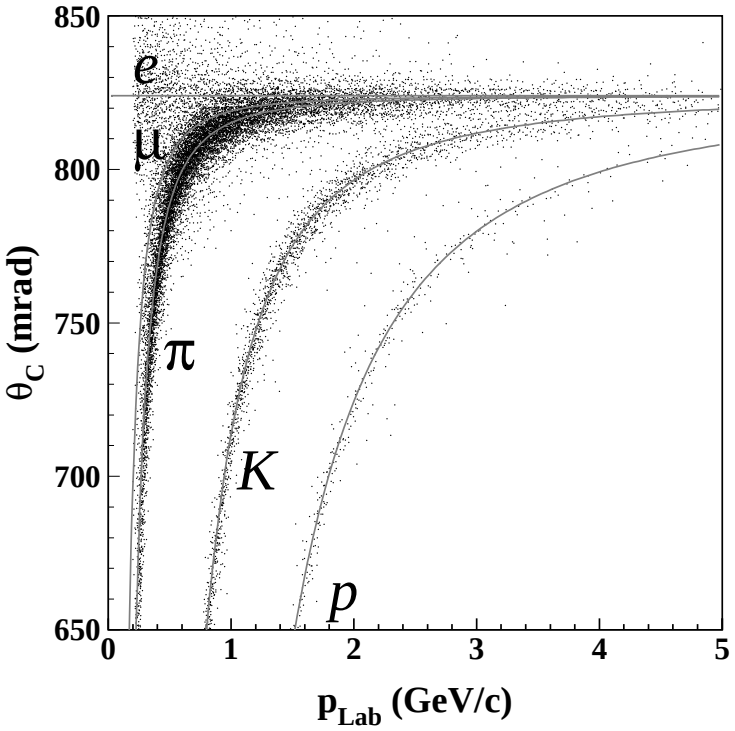

Figure 3.11: The Cherenkov angle, θ_c, of tracks from an inclusive sample of multihadron events plotted against the momentum of the tracks at the entrance to the DIRC. The grey lines are the predicted values of θ_c for different particle species (from [40]).

The Particle Identification (PID) system must provide π/K separation of 4 standard deviations or greater for tracks with a momentum up to about 4 GeV/c. This upper limit is dictated by the requirement to measure rare B decays such as $B^0 \to \pi^+\pi^-$ and $B^0 \to K^+\pi^-$. The DIRC provides the necessary PID for tracks above 700 MeV/c while below this momentum the PID relies mainly on the dE/dx measurements in the DCH and SVT.

The PID system must be thin and uniform in terms of radiation lengths to minimise degradation of the calorimeter energy resolution. The PID system also needs a fast signal response and must be tolerant to high backgrounds.

3.5.2 Design of the DIRC

The DIRC uses the principle that the magnitudes of angles are maintained upon reflection from a flat surface, as shown by the schematic in figure 3.12 of the

DIRC geometry.

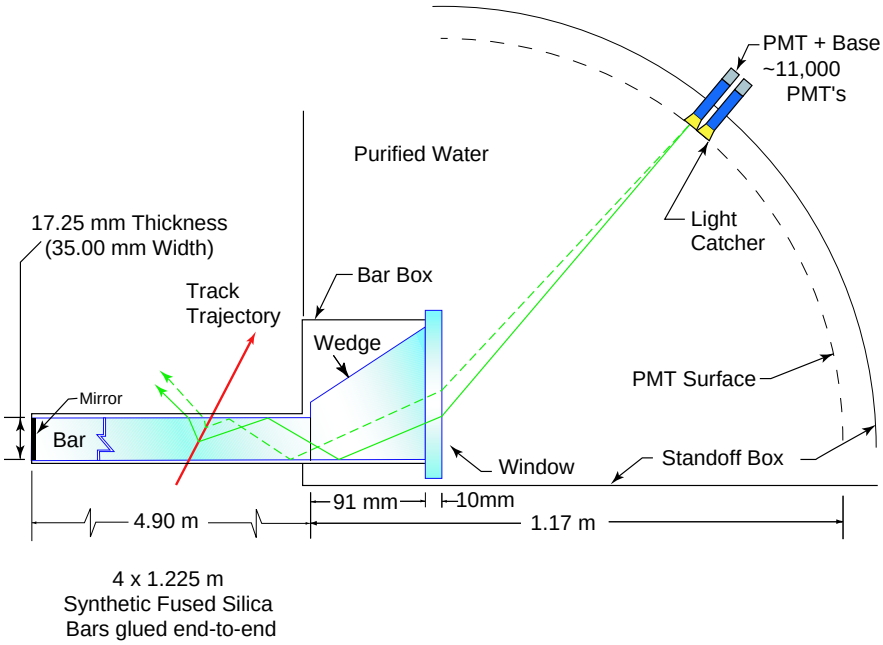

Figure 3.12: Schematic of DIRC fused silica radiator bar and imaging region (from [35]).

The relationship between the Cherenkov angle and the refractive index of the radiator material is shown in equation 3.1. For particles with β approximately equal to one, some photons will always lie within the limit for total internal reflection, so the radiation can therefore be transported via total internal reflection, preserving the Cherenkov angle.

The radiator material is synthetic, fused silica, in the form of bars, each 17 mm thick, 35 mm wide and 4.9 m long (each bar is made of four 1.225 m pieces glued end-to-end). These bars act as radiators and as light pipes to transport the light trapped by total internal reflection. Fused, synthetic silica is used because of its resistance to ionizing radiation, its long attenuation length, large index of refraction ($n = 1.437$), low chromatic dispersion within the wavelength of acceptance of the DIRC and because it allows an excellent optical finish on the surfaces of the bars. There are a total of 144 bars, which are placed into 12 hermetically sealed containers called bar boxes. Within a bar box the 12 bars are optically isolated by a $\sim$150 μm air gap between neighbouring bars. The bar boxes are made of thin aluminium, arranged in a 12-sided polygon barrel.

At *BABAR* particles are produced preferentially in the forward direction be-

cause of the asymmetric beam energies. To avoid interference with other detector systems in the forward region, only the backward end of the bar is instrumented with photon detectors, while a mirror is placed at the forward end to reflect incident photons.

Once photons arrive at the instrumented end of the bar, most of them emerge into a water-filled expansion region called the standoff box. There is a fused silica wedge glued to the readout end of each bar which reflects photons at large angles relative to the bar axis, thereby reducing the size of the required detector surface. The 12 wedges in a bar box are glued to a common 10 mm thick fused silica window which provides the seal to the purified water in the standoff box.

The standoff box is made of stainless steel and contains about 6000 litres of purified water. Water is used because it is inexpensive and has an average index of refraction ($n = 1.346$) and a chromaticity index which are reasonably close to that of the fused silica, thereby eliminating dispersion and minimising total internal reflection at the silica/water interface. The water must maintain good transparency at wavelengths as small as 300 nm, so the water must be ultra-pure, de-ionized, de-gassed and free of bacteria. Purified water attacks many materials so most plumbing components are made of stainless steel or polyvinylidene fluoride, which are selected for their known compatibility with purified water.

At the back of the standoff box, the photons are detected by an array of photomultiplier tubes (PMTs), which are arranged into 12 sectors, each containing 896 densely packed PMTs. Each PMT is 29 mm in diameter and is surrounded by a hexagonal reflecting cone to capture light which would otherwise miss the active area, resulting in $\sim$90% of the surface area actively collecting light. The distance from the end of the bars to the PMTs is about 1.17 m and along with the size of the bars and PMTs, this gives a geometric contribution to the single photon Cherenkov angle resolution of $\sim$7 mrad (the overall single photon resolution is estimated to be 10 mrad).

The Cherenkov light pattern at the surface of the PMT is a conic section, where the cone opening-angle is the Cherenkov production angle modified by refraction at the exit from the fused silica window. The observed space-time coordinates of the PMT signal are reconstructed to give the emission angle and arrival time of the Cherenkov photon, while the tracking system provides the track position and angle. This information is used to determine the Cherenkov angle, which in turn identifies the charged particle type (as electron, muon, pion,

kaon or proton).

3.6 Electromagnetic calorimeter (EMC)

The EMC is made up of 6580 thallium-doped cesium-iodide (CsI(Tl)) crystals, and measures the energy of electromagnetic showers, identifying electrons and photons and measuring their energy.

3.6.1 Purpose and requirements of the EMC

The identification of electrons is important for the τ analysis described in chapter 7 because electron tagging of $\tau^- \to e^-\overline{\nu_e}\nu_\tau$ decays can provide an efficient way of selecting $\tau^+\tau^-$ events. Electrons are also used for the flavour tagging of neutral B mesons and for reconstructing the J/ψ vector meson.

It is important to identify photons from electromagnetic and radiative processes as well as those from π^0 and η decays. Rare τ lepton and B meson decays can contain multiple π^0s and ηs.

The electromagnetic calorimeter measures electromagnetic showers over the energy range from 20 MeV to 9 GeV, where the lower bound is set by a need to efficiently reconstruct the π^0 and η mesons which decay into photons. The upper bound comes from a need to measure quantum electrodynamic (QED) processes (such as $e^+e^- \to e^+e^-(\gamma)$ and $e^+e^- \to \gamma\gamma$) for calibration and luminosity determination.

At higher energies the energy resolution is $\sim$2% and the angular resolution is $\sim$3 mrad while at low energies the energy and angular resolutions are $\sim$5% and $\sim$12 mrad respectively. The tightest requirements on the energy and angular resolution come from measuring rare B meson decays containing π^0s (such as $B^0 \to \pi^0\pi^0$), which require an energy resolution of order 1-2%. Below energies of 2 GeV the π^0 mass resolution is dominated by the EMC energy resolution, while at high energies the angular resolution dominates. To achieve the required resolution the operating conditions must be kept stable, requiring close monitoring of the temperature and radiation exposure, and frequent calibrating of the electronics and energy response.

The reconstructed $\pi^0 \to \gamma\gamma$ mass is measured as 135.1 MeV/c^2 and is stable to better than 1% over the full photon energy range. The width is 6.9 MeV/c^2,

although this improves to 6.5 MeV/c^2 for low occupancy $\tau^+\tau^-$ events with π^0 energy below 1 GeV.

A typical electromagnetic shower spreads over many adjacent crystals, forming a 'cluster' of energy deposits. Pattern recognition algorithms identify these clusters and differentiate between single clusters with one energy maximum and merged clusters with more than one local energy maximum, called 'bumps'. A cluster or bump is associated with a charged particle if the position of the energy-weighted centroid is consistent with an extrapolated track. Otherwise, it is assumed to originate from a neutral particle.

The separation of electrons and charged hadrons is based primarily on shower energy, lateral shower moments and track momentum. Also, $\mathrm{d}E/\mathrm{d}x$ energy loss in the DCH and the DIRC Cherenkov angle are required to be consistent with the values that an electron would be expected to produce. The most important variable for the discrimination of hadrons from electrons is the ratio of the shower energy to the track momentum (E/p).

3.6.2 Design of the EMC

The EMC is a hermetic, total-absorption calorimeter, composed of a finely segmented array of thallium-doped cesium iodide (CsI(Tl)) crystals, which are read out with silicon photodiodes.

The EMC consists of a cylindrical barrel and a forward endcap, as shown in figure 3.13; the barrel contains 5760 crystals arranged in 48 rings, while the endcap holds 820 crystals arranged in 8 rings. The crystals have a tapered trapezoidal cross section and they are longer in the forward direction (32.4 cm) than the backward direction (29.6 cm) to limit shower leakage from the more energetic particles.

The CsI(Tl) crystals have a high light yield which allows sufficient energy resolution, and a short radiation length which allows for shower containment with a relatively compact design. The emission spectrum and light yield also allows the use of silicon photodiodes which perform well in high magnetic fields.

The intrinsic efficiency for the detection of photons in CsI(Tl) is nearly 100% down to a few MeV. However, the minimum measurable energy in colliding beam data is about 20 MeV because of the amount of material in front of the EMC and because of beam- and event-related backgrounds. The π^0 efficiency is sensitive to the minimum detectable photon energy so it is important to reduce the amount

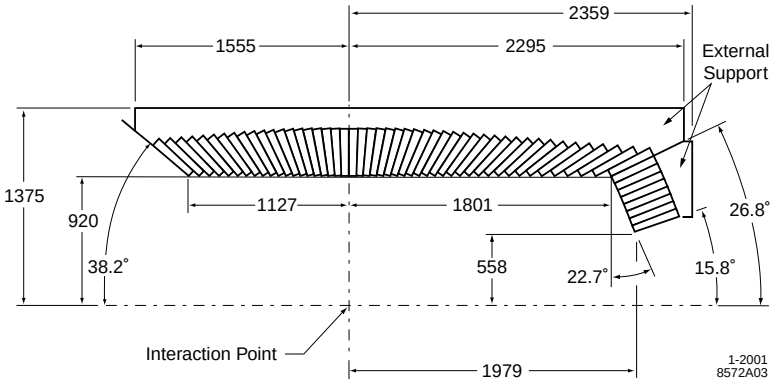

Figure 3.13: A longitudinal section of the EMC showing the crystals (from [35]).

of material in front of the EMC. This is achieved by supporting the crystals at the back, with only a thin gas seal at the front. The barrel and outer rings of the endcap have less than 0.6 radiation lengths of material in front of the crystal faces while the innermost ring of the endcap has 3 radiation lengths of material, due to the SVT support structure and electronics and the B1 dipole magnet.

The crystals not only act as a total-absorption scintillating medium, but also as a light guide to direct light to the photodiodes mounted on the rear surface. Most of the light is internally reflected by the polished crystal surface and the small amount which is transmitted out of the crystal is partly recovered by 2 layers of diffuse white reflector wrapped around the crystal, as shown in figure 3.14. The crystals are also wrapped in aluminium foil to provide a Faraday shield and finally are covered in a layer of mylar to provide electrical insulation from the support structure.

The photon detector consists of two 2×1 cm^2 silicon PIN diodes, each connected to a low-noise preamplifier. Two are used for redundancy in case of failure, because of the inaccessibility of the system. The PIN diodes are glued to the rear face of the crystal using a optical epoxy to optimise light transmission (while the rest of the rear crystal face is covered with a plastic plate coated in reflective paint). This assembly is enclosed in an aluminium frame which is electrically coupled to the foil wrapped around the crystal and thermally coupled to the support structure to dissipate the heat from the preamplifiers.

The analogue signals from the preamplifiers are digitised by analogue-digital boards (ADBs) housed in mini-crates at the end-flanges of the calorimeter (which are accessible for maintenance), as shown in figure 3.15. Each ADB contains 3

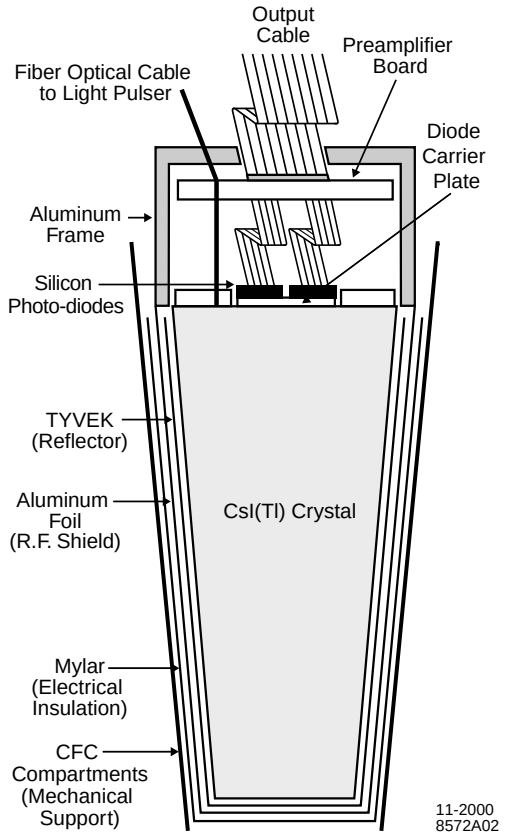

Figure 3.14: A schematic of the wrapped CsI(Tl) crystal and the front-end readout package mounted on the rear surface (not to scale) (from [35]).

custom auto-range encoding (CARE) circuits which each receive signals from 4 crystals and further amplify these signals. The ADBs are connected to input-output boards (IOBs) which transmit the signals to readout modules (ROMs), away from the detector, via 30 m long fibre-optic cables. The barrel has 80 IOBs, each connected to 6 ADBs, while the endcap has 20 IOBs, each connected to 4 ADBs. Each ROM reads out 10 IOBs and each fibre-optic cable carries the data from 24 crystals (2 ADBs) to the ROM. In the ROM the continuous data stream enters a digital pipeline, which is tapped to extract a signal for the calorimeter trigger.

The EMC external support structure is built in 2 sections, a cylinder for the barrel (shown in figure 3.15) and two semi-circular structures for the forward endcap. The structure supports 300 modules which are made from tapered, trapezoidal compartments built from carbon-fibre-epoxy composite (CFC) with 300 μm thick walls. Each compartment holds a single wrapped crystal, en-

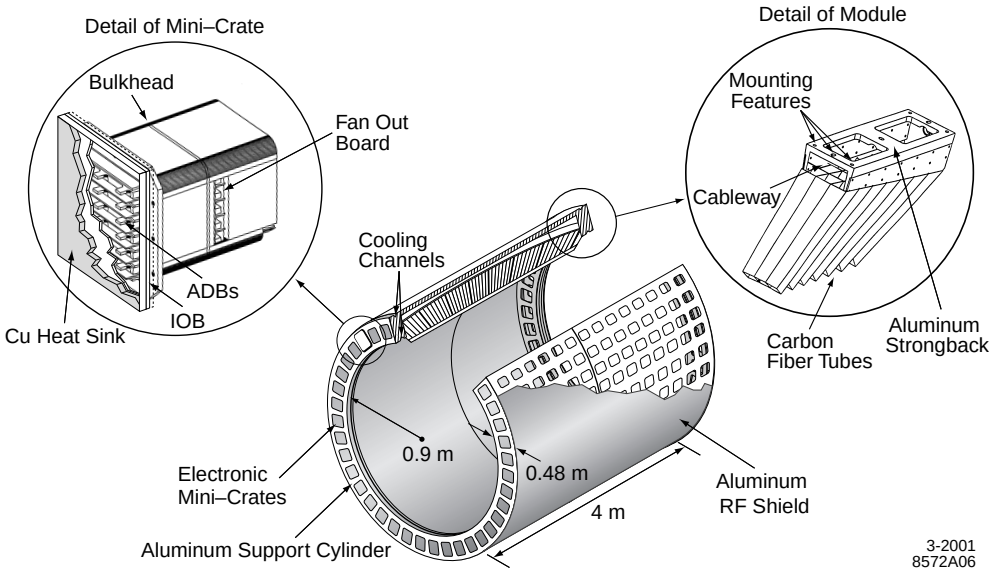

Figure 3.15: The EMC barrel support structure, showing the modules and electronics crates (not to scale) (from [35]).

suring that the force on the crystal surface never exceeds its own weight, thus preventing crystal deformation and surface degradation which could compromise performance. The modules are attached to the support structure at the back, with an open face at the front, reducing the material between and in front of the crystals.

The calorimeter is surrounded by a double Faraday shield, made of two 1 mm thick aluminium sheets, protecting the diodes and preamplifiers from external noise. Inside, the crystals are kept in a dry, temperature controlled nitrogen atmosphere. The temperature must be kept constant because thermal expansion can stress the crystal-diode epoxy joints, and the photodiode leakage current and light yield of CsI(Tl) are temperature dependent. The heat from the electronics is removed by conduction to channels of chilled water and a system of Fluorinert (polychlorotrifluoro-ethylene).

The crystals are individually calibrated at low energies using the 6.13 MeV photons produced by irradiated Fluorinert. At higher-energies (3-9 GeV) the calibration is done using a sample of Bhabha events, where the energy of the detected shower can be predicted from the polar angle of the $e^{\pm}$. From these calibrations (as well as from $\pi^0 \to \gamma\gamma$ and $\chi_c \to J/\psi\gamma$ decays) the energy resolution, σ_E, as

a function of energy, E, is found and fitted with the function

$$\frac{\sigma_E}{E} = \frac{(2.32 \pm 0.30)\%}{\sqrt[4]{E(\mathrm{GeV})}} \oplus (1.85 \pm 0.12)\%, \tag{3.2}$$

where $\oplus$ denotes adding in quadrature.

The light response of the crystals is measured using a light pulser system, which transmits light from a xenon flash lamp to the rear of each crystal, allowing a measurement of the linearity of light collection, conversion to charge, amplification and digitisation. The temperature is monitored by 246 thermal sensors, while the radiation exposure is monitored by 116 real-time integrated dosimeters (RadFETs).

3.7 Solenoid magnet

The magnet system consists of a superconducting solenoid, a segmented flux return and a bucking coil for field compensation. The superconducting solenoid creates a magnetic field of 1.5 T, which is required to achieve the desired momentum resolution for charged particles. The magnitude of the field within the tracking volume is required to be constant within a few percent, in order to simplify track finding and fitting. The solenoid is made of 10.3 km of niobium-titanium filaments, each less than 40 μm in diameter, and a pure aluminium stabiliser. It is cooled to a temperature of 4.5 K using liquid helium.

The solenoid is also designed to minimise disturbance to PEP-II operation which means minimising the leakage of magnetic flux. At the backward end flux leakage is a particular problem as it can disrupt the DIRC photomultipliers and PEP-II quadrupoles. A bucking coil, a conventional, water-cooled, copper coil, mounted on the face of the backward door, is designed to reduce stray field to an acceptable level.

The flux return, made of low-carbon steel, provides structure and support for the detector subsystems. It is designed to withstand earthquakes and the magnetic forces in the event of a magnet quench (a quench in the superconducting magnet would cause eddy currents in conducting components which could generate sizable forces). In addition, the flux return serves as a hadron absorber for muon/hadron separation (as described in section 3.8).

3.8 Instrumented flux return (IFR)

The IFR provides information for the identification of muons and K_L^0 hadrons by using the steel flux return as a muon filter and hadron absorber. Thin layers of detectors inside gaps in the steel detect muons and hadronic showers.

3.8.1 Purpose and requirements of the IFR

Muons are important for determining the luminosity using $e^+e^- \to \mu^+\mu^-$ events. They are important for the τ analysis described in chapter 7 because muon tagging of $\tau^- \to \mu^-\overline{\nu_\mu}\nu_\tau$ decays can efficiently select $\tau^+\tau^-$ events. Muons are also used to reconstruct J/ψ and $\Upsilon(2S)$ and for tagging the flavour of neutral B mesons. The detection of K_L^0 allows the study of exclusive B decays, particularly CP eigenstates.

Muon identification relies on the IFR but does use complimentary information from other subsystems. The charged particle tracks are reconstructed in the SVT and DCH and a muon is required to meet criteria for minimum ionizing particles in the EMC. If a cluster of hits in the IFR is associated with a charged track, it could be either a muon or a charged hadron. These are separated by counting the number of interaction lengths from the interaction point to the outermost detector layer which records a hit; and by comparing the projected track with the energy-weighted centroids of the clusters in different layers.

Neutral hadrons, such as K_L^0, may interact in the steel of the IFR creating showers which are detected as energy clusters which are not associated with a charged track. Since a significant fraction of hadrons interact before reaching the IFR, additional information from the EMC improves the angular resolution. No useful information on the energy of the cluster can be obtained.

The IFR is required to have a large solid angle coverage. The muon identification must have a relatively good efficiency and high background rejection for muons with momenta down to below 1 GeV/c. For neutral hadrons, the most important requirements are high efficiency and good angular resolution.

3.8.2 Design of the IFR

The steel flux return of the magnet (see section 3.7) consists of a hexagonal barrel section and 2 hexagonal end doors, as shown in figure 3.16, which are used as a muon filter and hadron absorber. The steel is segmented into 18 plates, increasing

in thickness from 2 cm for the inner plates to 10 cm for the outer plates. The gaps between the steel plates are 3.5 cm wide in the inner layers of the barrel and 3.2 cm everywhere else, and are filled with detectors.

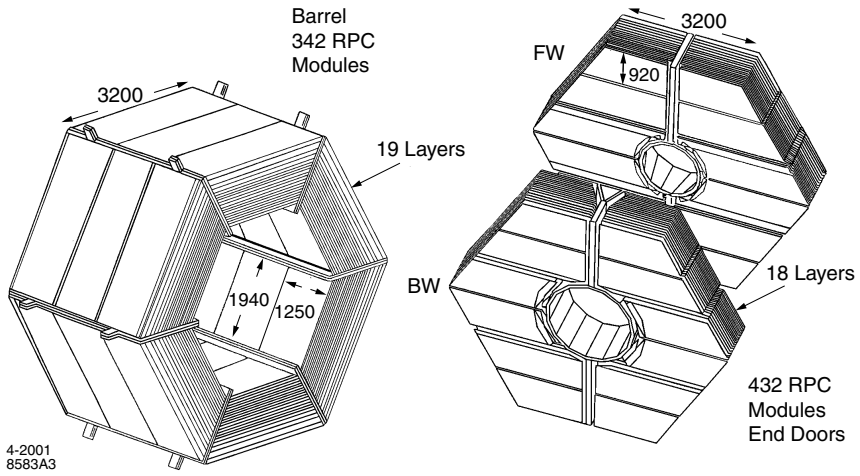

Figure 3.16: Overview of IFR showing the barrel sectors and the forward (FW) and backward (BW) end doors (from [35]).

Originally, all the detectors were chosen to be resistive plate chambers (RPCs) and a total of 806 RPC modules were installed; 19 RPC layers in the barrel, 18 layers in the end doors and 2 layers of cylindrical RPCs between the EMC and the magnet to detect particles exiting the EMC. The RPCs were chosen because they are low cost (important when filling a large area), and they produce large signals and have a fast response, allowing for simple electronics and good time resolution. They can also be constructed to cover irregular shapes so each module was built to match the gaps in the steel with very little dead space (more than 25 different shapes and sizes were built).

An RPC consists of two bakelite (phenolic polymer) sheets, 2 mm thick, separated by a gap of 2 mm which is filled with gas (a mixture of argon, freon and isobutane), as shown in figure 3.17. The bakelite surfaces facing the gap are treated with linseed oil while the external surfaces are coated with graphite, which is connected to high voltage and ground, and protected with an insulating mylar film. When charged particles pass through, the gas is ionized and the ions are accelerated through the high voltage. The signal is read out capacitively, on both sides of the gap, by external electrodes made of aluminium strips. The strips on each side are aligned perpendicular to each other, to give z and ϕ coordinates.

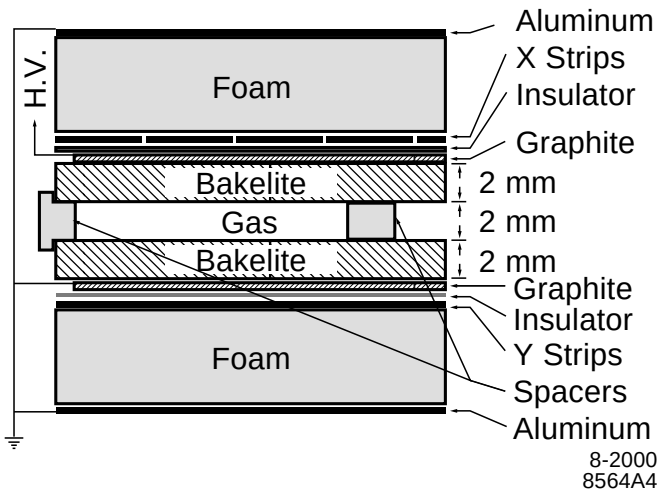

Figure 3.17: Cross section of a planar RPC with schematic of the high voltage (HV) connection (from [35]).

These readout strips are separated from the aluminium plate by 4 mm thick foam sheets, and are connected to the readout electronics at one end and terminated with a resistor at the other.

Unfortunately, during the first summer of operations the temperature in the operating hall frequently exceeded 31°C and a large fraction of RPCs showed some reduction in efficiency. Water-cooling was installed on the barrel and end doors, which succeeded in stabilising the temperature, but the efficiency of the RPCs continued to deteriorate. It is possible that the high temperatures caused the linseed oil to leak from the bakelite surface into the active region.

It was decided to replace many of the barrel RPCs with Limited Streamer Tubes (LSTs). This upgrade was completed in stages, finishing in September 2006. Not every RPC layer was replaced with LSTs; some were not accessible and some were replaced with brass absorbers plates to reduce the contamination from hadron decays and punch through (when a hadron causes only minimum ionization, appearing as a muon).

The LSTs are made from PVC tubes, coated with a layer of graphite paint and filled with gas, with a silver-plated wire running down the centre. Charged particles passing through the tube ionize atoms of the gas, creating a streamer, inducing signals on the capacitive readout strips surrounding the tube. The LSTs have consistently out-performed the RPCs they replaced, achieving muon

identification efficiencies of up to 94%.

3.9 Trigger

The trigger system is required to select the events needed for the physics goals with a high, stable and well understood efficiency, while rejecting background events and keeping the total event rate under 120 Hz. At the design luminosity, beam-induced background rates are ∼20 kHz for events with at least one track in the drift chamber with $p_t > 120$ MeV/c, and ∼20 kHz for events with at least one EMC cluster with $E > 100$ MeV. The total trigger efficiency is required to be at least 99% for $B\overline{B}$ events, at least 95% for continuum events and at least 90% for $\tau^+\tau^-$ events.

The trigger reduces the rate of the main physics sources to ∼90 Hz and also identifies and flags ∼30 Hz of events used for luminosity determination, and diagnostic and calibration purposes.

The trigger is implemented as a two-level hierarchy, the Level 1 (L1) in hardware followed by the Level 3 (L3) in software.

3.9.1 Level 1 trigger system

The L1 trigger decision is based on information from the drift chamber trigger (DCT), the calorimeter trigger (EMT) and the instrumented flux return trigger (IFT), as shown in figure 3.18. These 3 trigger processors generate a summary of the position and energy of particles, which is passed to the global trigger (GLT) every 134 ns. The GLT processes all the information to form triggers which are passed to the Fast Control and Timing System (FCTS) [41], which can then issue an *L1 Accept* signal to initiate event readout.

The L1 trigger decision is made 11-12 μs after the e^+e^- collision (2 μs for the data to reach the DCT and EMT, 4-5 μs for them to process the event, ∼3 μs of processing in the GLT and 1 μs for the trigger to propagate through the FCTS), well within the 12.8 μs buffer capacity limit.

The DCT receives one bit of data for each of the 7104 DCH cells. First, Track Segment Finder (TSF) modules are used to find track segments in groups of 8 cells. These data are then passed to the Binary Link Tracker (BLT) module which links the segments into complete tracks. In parallel, information on high quality track segments are passed to Transverse Momentum Discriminator (TMD)

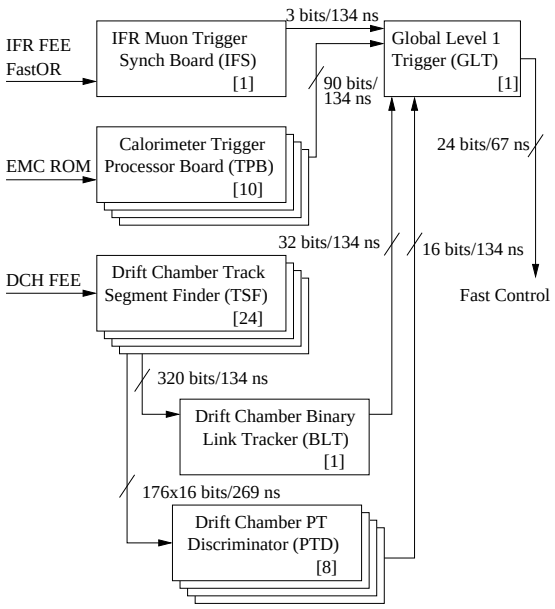

Figure 3.18: Simplified schematic of the L1 trigger system. The number of components are given in the square brackets (from [35]).

modules, which determine if the segments are consistent with a track transverse momentum greater than a preset threshold.

For trigger purposes the EMC is divided into 280 towers, each made of 19-24 crystals. For each tower, all the crystal energies above a threshold of 20 MeV/c are summed and sent to the EMT every 269 ns. The EMT has Trigger Processor Boards (TPBs) which sum the energies of different combinations of towers (for differing ranges of θ) and compare them to preset thresholds.

The IFT is used to trigger on $\mu^+\mu^-$ events and cosmic rays. The IFR is divided into 6 barrel sections and 4 end door sections and the IFT counts which sections have a certain number of hits within a 134 ns time window. Then these sectors are used to categorise the event as one of seven types (e.g. 2 back-to-back signals in the barrel and 1 signal in the forward end door).

The GLT combines the information and sends a 24-bit output to the FCTS every 67 ns for the final decision. The L1 trigger has a typical output rate of 1 kHz, which includes $\sim$130 Hz from Bhabha and annihilation physics events, 100 Hz of cosmic ray triggers and 20 Hz of random beam crossing triggers. The remaining triggers are due to 'lost' particles interacting with the beam pipe or other components.

3.9.2 Level 3 trigger system

The L3 trigger reconstructs, classifies and monitors events and refines the selections made by the L1 trigger. The L3 trigger is made up of independent classification tests and a way of combining the tests. The tests consist of algorithms which construct quantities of interest, followed by filters which determine whether those quantities satisfy specific selection criteria. The filters have access to the complete event data, including the output of the L1 trigger processors, and they perform event classification and background rejection based on the tracks and clusters.

The L3 DCH-based algorithm, L3Dch, begins with the track segments from L1 and improves them with fast pattern recognition and fitting. The fitting is iterated, adding segments close to the track and dropping hits which are further away. The DCH filters select events with either one track with $p_t > 600$ MeV/c or two tracks with $p_t > 250$ MeV/c, all originating from the IP.

The L3 EMC-based algorithm, L3Emc, identifies energy clusters with increased sensitivity, sufficient for finding minimum ionizing particles. Clusters with a total energy above 100 MeV are retained. The EMC filters select events with an event mass greater than 1.5 GeV, where the event mass is the effective mass calculated assuming that all the clusters are due to photons. The event is also required to have either high energy deposits (at least two clusters of $E_{CM} > 350$ MeV) or high cluster multiplicity (at least 4 clusters).

There are also veto filters to reject background events, especially Bhabha events which would otherwise dominate. Bhabha, radiative Bhabha and cosmic ray events are flagged for calibration and offline luminosity measurements. Online monitoring of the luminosity, energy scale and beam energies is also performed by the L3 trigger.

Chapter 4

Data reconstruction and simulation

This chapter describes how the data produced by the *BABAR* detector are transformed into a dataset suitable for physics analysis. This task is accomplished by a complex computing system called 'Computing Model 2' (CM2) which is written primarily in the object-oriented C++ programming language. It is a distributed system, meaning that various tasks described below, such as simulation, skimming and data storage, are done at computing sites around the world, thereby dividing the computing responsibilities among the members of the *BABAR* Collaboration.

The *BABAR* software is organised in terms of packages, which are collections of files designed to perform a well defined task. Some packages work as part of a group, while others function independently, and there are different types of packages for the different computing tasks. The *BABAR* software is constantly evolving so new, self-consistent versions of the software, called 'releases', are implemented periodically; the work detailed in this thesis uses release 22 of the software.

Section 4.1 will describe how the raw data from the detector are collected, reconstructed and stored on disk, while the event reconstruction process is outlined in more detailed in section 4.2. Section 4.3 describes how simulated data are generated and reconstructed, while section 4.4 outlines how the simulation is corrected to more accurately imitate the data. The selection of events which share certain physics characteristics is discussed in section 4.5 and section 4.6 outlines how physics analysis is performed.

4.1 Data collection

As particles pass through and interact with the *BABAR* detector, electronic signals are produced by the different subsystems. These raw detector signals are the first form that the data takes. These signals must be efficiently collected by the online processing system and reliably stored in a form ready for physics analysis.

4.1.1 Data samples

The *BABAR* experiment took data between October 1999 and April 2008, during which time the data taking was split into 7 periods, called 'Runs', with time for detector upgrades and repairs in between. For Runs 1 to 6, data collected at the Υ(4S) resonance are called 'on-peak' data while the 'off-peak' data, which makes up $\sim$ 12% of the data collected, are collected at energies $\sim$ 40 MeV below the Υ(4S) resonance. During Run 7, the on-peak data was collected at the Υ(3S) resonance and then at the Υ(2S) resonance, with the corresponding off-peak data collected at an energy $\sim$ 30 MeV below each resonance. The total integrated luminosity recorded within each Run is given in table 4.1, for on-peak and off-peak data.

Resonance	Run number	Run period	Luminosity (fb^{-1})	
			on-peak	off-peak
Υ(4S)	1	Feb 2000 - Oct 2000	20.4	2.6
	2	Feb 2001 - Jun 2002	61.1	6.9
	3	Dec 2002 - Jun 2003	32.3	2.5
	4	Sep 2003 - Jul 2004	100.3	10.1
	5	May 2005 - Aug 2006	133.3	14.5
	6	Jan 2007 - Aug 2008	78.4	7.8
	1-6	Feb 2000 - Aug 2008	425.7	44.4
Υ(3S)	7	Dec 2007 - Apr 2008	28.0	2.6
Υ(2S)			13.6	1.4
Υ(4S),Υ(3S) and Υ(2S)	1-7	Feb 2000 - Apr 2008	467.3	48.4

Table 4.1: The integrated luminosity recorded during each Run.

4.1.2 Online processing

The purpose of the online computing system, or data acquisition system, is to transfer data from the detector front end electronics (FEE) to storage in computer

farms for further analysis. The system also includes components required for the control of the detector, immediate data quality monitoring and online calibration. It supports a Level 1 (L1) trigger accept rate of up to 2 kHz, with an average event size of $\sim$ 32 kbytes and a maximum output (Level 3 trigger accept) rate of 120 Hz. During normal data taking the online system routinely achieved an efficiency of over 98%.

During data-taking the detector operator had 17 display screens which ran a custom graphic user interface. The displays included detector controls, control panels, strip charts and an alarm handler, with an electronic logbook available through a web browser interface. Each detector subsystem had a set of calibration and diagnostic applications using tools provided by the online system.

The entire online system is coded primarily in the C++ language with some use of Java for graphical user interfaces. The online computing system consists of five subsystems, outlined below.

The Online Dataflow (ODF) provides the interface for data acquisition from, and control of, the detector subsystem front end electronics (FEEs). The ODF system runs on a dedicated collection of hardware: the data from the FEEs are transfered, via optical fibre links, to 157 custom readout modules (ROMs) which are housed in 23 data acquisition VME crates. The ROMs are grouped by detector subsystem and controlled by the ODF software. As described in section 3.9.1, event acquisition is prompted by a trigger decision based on the L1 trigger and formed by the Fast Control and Timing System (FCTS). The ODF system receives the '*L1 Accept*' signals, and distributes them to the ROMs. One ROM in each crate aggregates the data and then the ODF system builds complete events from all the ROMs and delivers them to 32 commercial Unix workstations which are part of the online farm. Data used for monitoring programs that calculate quantities such as luminosity, deadtime and trigger rates are transmitted by the ODF system which also monitors time counters to ensure that the clocks of the FEEs stay synchronised.

The Online Event Processing (OEP) provides the framework for the processing of complete events delivered by the ODF system [42]. It includes operating the L3 trigger software, data quality monitoring and the final stages of online calibrations. Raw data delivered by the ODF system are put into an object-oriented form and made available through the standard data analysis

interface. The 'Fast Monitoring' system provides detailed information for data quality monitoring, including automated comparisons of live monitoring data against defined references. It is viewed using the Java Analysis Studio (JAS) package [43], which displays the histograms on a dedicated operator console.

The Logging Manager receives the events from the OEP system, which have been selected by the L3 trigger, and writes them to disk files which are the input for the Online Prompt Reconstruction processing (described in section 4.1.3). The files are also accessible for other tasks such as offline tests of L3 trigger algorithms and detector system hardware diagnostics.

The Online Detector Control (ODC) controls and monitors the environmental conditions of the detector subsystems and is based on the Experimental Physics and Industrial Control System (EPICS) [44]. EPICS provides a direct connection to the electrical signals of the power supplies and other hardware, with sufficient monitoring and control to allow testing and fault diagnosis. The interface with the operator is provided by the EPICS 'display manager', which shows the online status of all the detector systems, and the EPICS 'alarm handler' which provides the operator with colour coded alarms and warnings. The ODC also provides data transfer between the detector and the PEP-II accelerator to allow safe and efficient data collection.

The Online Run Control (ORC) oversees the other online components, sequencing their operations and providing a graphical user interface for operator control. It is implemented as an application in SMI++, a toolkit for designing distributed control systems [45]. The system is highly automated with the operator only needing to initialise the system, start and stop the data-taking and handle unusual error conditions. The ORC will only start data-taking if all the various systems are in a state suitable for production-quality data-taking.

4.1.3 Prompt reconstruction

The online and offline systems are connected by the 'Prompt Reconstruction' software, which uses the `ELF` application. This system reads the raw data recorded to disk by the Logging Manager and, operating on a farm of 150 Unix processors,

it performs selection, calibration, monitoring and reconstruction of physics events before saving them to the event store database (described in section 4.1.4).

First, the raw data are digitised (using the `TCtoDigiConversion` module), meaning that the data are converted into `digis` which each represent a hit in a detector subsection.

The 'Prompt Calibration' is a *rolling calibration* process, which runs `ELF` over a subset of events to generate calibration constants, which are applied to the processing of subsequent events. Monitoring data are also collected at this stage and used to ensure the quality of the data.

Finally, the 'Event Reconstruction' process runs `ELF` over all events. The `digis` are reconstructed into particle tracks, energy clusters and candidate particles, as described in detail in section 4.2, which are then ready for use in physics analysis.

4.1.4 Data storage

There are several databases used at *BABAR* for the storage of information. The databases most relevant to this work are the event store and the conditions database.

The `Root`-based *BABAR* event store database manages and tracks the data from the initial raw data, produced by the detector or by simulations, through event reconstruction and physics analysis. It handles the creation of sub-samples of events that meet different criteria and the reprocessing of data following updated conditions information.

The conditions database manages and tracks the conditions under which experimental data were acquired. It includes electronic calibrations, detector calibrations (e.g. drift-time relationships) and detector alignments. It is designed to allow for a complete description of the detector as a function of time, where different components of the detector may exhibit different time variances. This database was implemented using the commercial object-oriented database management system Objectivity [46].

4.2 Event reconstruction

As described in section 4.1.3, the 'Event Reconstruction' process reconstructs raw data from the online event processing (OEP). Each detector subsystem has its own

event reconstruction packages, containing reconstruction modules which dictate the particle objects to be formed. Hits in the SVT and DCH are reconstructed into charged particle tracks, while hits in the EMC and IFR are reconstructed into energy clusters. The tracks and clusters are then reconstructed, along with particle identification information from the DIRC, into candidate particles, which are compiled into 'candidate particles lists'. The final reconstructed data constitute the `AllEvents` data set and are written to the event store database for use in physics analyses.

4.2.1 Charged particle tracking

Tracks left by charged particles passing through the detector (know as 'charged tracks') are reconstructed from hits in the SVT and DCH subsystems. The offline track reconstruction software builds on the information from the Level 3 (L3) trigger (as described in section 3.9.2), refining it with more complex algorithms. The resulting tracks are compiled into 'charged track lists', shown in table 4.2, according to their properties. The particles associated with the tracks are assigned a mass according to a stable particle hypothesis. For the most general tracks list, *chargedTracks*, the default choice is the pion hypothesis.

Charged track list	Description
chargedTracks	Charged particle tracks in SVT and/or DCH with pion mass hypothesis assigned.
goodTracksVeryLoose	*chargedTracks* with: momentum < 10 GeV/c; $DOCA$ in xy-plane < 1.5 cm; $DOCA$ in $z < 10$ cm.
goodTracksLoose	*goodTracksVeryLoose* with: transverse momentum > 0.1 GeV/c; number of DCH hits ≥ 12.
goodTracksTight	*goodTracksLoose* with: number of DCH hits ≥ 20; $DOCA$ in xy-plane < 1 cm; $DOCA$ in $z < 3$ cm.

Table 4.2: Lists of reconstructed charged particle tracks stored in the *BABAR* event store database, where $DOCA$ is the distance of closest approach of a track to the interaction point.

4.2.2 Neutral candidates

Particles passing into the EMC and IFR can leave energy deposits which are reconstructed into energy clusters (a continuously connected region of hits) and bumps (a local maximum within a cluster). Track-matching algorithms determine whether a cluster or bump is associated with any track. Tracks are only produced by charged particles, so any cluster associated with a track is assumed to be the energy deposit of a charged particle and any cluster not associated with a track is assumed to be due to a neutral particle.

These candidate neutral particles are assigned to a 'neutral list', as shown in table 4.3. The most general list of neutral particles is the *calorNeutral* list.

Neutral list	List description
calorNeutral	Single EMC bumps and single-bump clusters, which are not matched with any track. Photon mass hypothesis applied.
calorClusterNeutral	Single-bump and multi-bump neutral clusters, which are not matched with any track.
neutralHad	Neutral candidates with IFR hits but no associated track or EMC bumps/clusters.
goodPhotonLoose	*calorNeutral* candidates with: $E_{lab} > 30$ MeV; $LAT < 0.8$.
goodPhotonDefault	*goodPhotonLoose* candidates with: $E_{lab} > 100$ MeV.

Table 4.3: Lists of reconstructed neutral objects stored in the *BABAR* event store database, where E_{lab} is the energy of the candidate in the laboratory frame and LAT is the lateral moment of the cluster.

One variable used to distinguish between different kinds of neutral particle is the lateral moment, LAT, which is defined as

$$LAT = \frac{\Sigma_{i=3}^{N} E_i r_i^2}{\Sigma_{i=3}^{N} E_i r_i^2 + E_1 r_0^2 + E_2 r_0^2}, \tag{4.1}$$

where r_0 is the distance between 2 crystals ($\sim$5 cm for the *BABAR* EMC), N is the number of crystals associated with the cluster, E_i is the energy deposited in the ith crystal (where the crystals are numbered such that $E_1 > E_2 > ... > E_N$),

and r_i is the distance from the cluster centre to the ith crystal.

Electromagnetic showers have a small lateral moment as they deposit most of their energy in two or three EMC crystals. This distinguishes them from hadronic showers, such as those caused by K_L^0 mesons, which deposit their energy over a larger number of crystals resulting in a lateral moment closer to one: this variable is therefore used to help identify photons.

Another method used to identify photons in the EMC comes from the fact that an electromagnetic shower is expected to produce a rotationally invariant shape while hadronic showers are more irregular and less isotropic in ϕ.

Neutral hadrons, such as K_L^0 mesons, are also identified using the fact that they may leave an energy deposit in the IFR, while photons usually only deposit energy in the EMC.

4.2.3 Charged particle identification

The aim of particle identification (PID) is to identify stable particles, that is, those that live long enough to leave a track or energy deposit in the detector. The stable particles are electrons, muons, pions, kaons, protons and photons. Other particles decay too quickly and must be reconstructed by combining the detected particles to form composite candidates.

The identification of the stable neutral particles, such as the photon and K_L^0, is described in the previous section, while this section focusses on PID for charged particles. Various 'PID selectors' are used to select charged particle candidates that are likely to be of a certain type. The PID selectors use 'PID variables' to accept or reject a given track as an electron, muon, pion, kaon or proton.

Electrons are identified using the variables $\mathrm{d}E/\mathrm{d}x$, E/p and other observables recorded by the EMC. Muons are identified as minimum ionising particles which deposit a small amount of energy in the EMC and register hits in several layers of the IFR. At momenta below 700 MeV/c pions and kaons are identified using $\mathrm{d}E/\mathrm{d}x$ (described is section 3.4) while at higher momenta identification is made using the Cherenkov angle and the number of Cherenkov photons, as recorded by the DIRC (described in section 3.5).

The PID selector can be changed to produce a looser or tighter selection, where the chosen level of a selector will be a compromise between the sample purity and selection efficiency. The purity of a sample is the fraction of particles within the sample which are of the desired particle type. The selection efficiency

is the fraction of particles of the desired type which are successfully selected.

There are several kinds of PID selector used at *BABAR*:

- Cut-based (Micro) selectors impose simple cuts of the PID variables, with different levels of selector corresponding to the tightness of the cuts.
- Likelihood (LH) selectors use PID variables to compute Likelihood functions for different PID hypotheses. Different levels of selector correspond to tighter or looser cuts on the likelihood function.
- Neutral network (NN) selectors use PID variables as inputs to a neutral network algorithm, which predicts outcomes on the bases of previous examples. The algorithms are 'trained' on large samples of simulated data to find how the PID variables behave for different particles; the selection is optimised based on this training.

4.2.4 Composite candidates

Many particles are not directly detectable because they decay before they can be detected or because they are neutral and do not leave a track or energy deposit. Their presence can still be inferred from the detection of their decay products (known as 'daughters', 'granddaughters', etc.). Particles which are reconstructed from their daughters in this way are called 'composite candidates'.

For a sample of data containing a composite particle, the simplest way of reconstructing the composite candidate is to calculate the invariant mass for each possible combination of daughters. The resulting mass spectrum has a peak at the mass of the composite particle. Each combination of correctly combined daughters will contribute to this peak while the incorrect combinations create a flat continuum background underneath.

More sophisticated ways of reconstructing composite candidates, on an event-by-event basis, use fitting procedures to determine whether a particular combination of particles are likely to be daughters. A 'geometric' fitter requires that the tracks of the (charged) daughters meet at a common point in space, returning the most likely common vertex position and momentum. A 'kinematic' fitting procedure requires that the four momentum at the vertex is conserved, returning the best fit to the momenta, masses and energies of the daughters.

The `SimpleComposition` package uses fitting and PID to create lists of reconstructed composite candidates from existing lists of tracks, neutral particles

and other composite candidates. It can also make lists by merging two other lists or by applying tighter cuts to an existing list. Further constraints can be applied to the fit, such as constraining the mass of any of the particles involved to the known mass. Alternatively, the production vertex of the mother can be constrained to be at a certain point (such as the interaction point or the decay vertex of another particle), or the energy of the mother in the CM frame can be constrained to be half the CM energy of the collider.

Although there are various fitting algorithms available, two which are maintained by the `SimpleComposition` package are `Add4` and `TreeFitter` [47]. The `Add4` fitter does four vector addition for kinematic fits and correctly deals with mass constraints, making it sufficient for most composite candidates, while for geometric fits `TreeFitter` is used.

Some of the most widely used composite candidate lists include lists of neutral K_S^0 and short-lived D and B mesons, but most important for this work are the π^0 lists. Neutral pions leave no tracks but, almost 99% of the time, they decay with a lifetime of 10^{-16} s into two photons. These are detected as energy deposits in the EMC and reconstructed into π^0 candidates. Pairs of neutral objects from a neutral candidates list are combined into π^0 candidates. Selections are applied to create the different π^0 lists shown in table 4.4. It is also possible for the two photons to appear as two bumps in a single cluster; the resulting π^0 candidates are called 'merged' π^0 s and appear in their own composite candidate lists.

4.3 Monte Carlo simulation

Monte Carlo (MC) simulations are vital for nearly all *BABAR* analyses. The simulated events should include all the information that is known about the modelling of physics processes and the *BABAR* detector, so that useful comparisons with data events can be made.

The MC samples are scaled individually by Run number according to the appropriate luminosity for each Run. This is done separately for each Run because the background conditions and experimental setup can vary between Runs and the MC samples are generated with these conditions taken into consideration.

The MC simulation of events happens in three stages. First the events are generated by modelling known physics processes, then the effect of the *BABAR* detector is simulated and finally the simulation is reconstructed into events, as

π^0 list	List description
pi0VeryLoose	Two *goodPhotonLoose* candidates with: 0.090 GeV $< m_{\pi^0} <$ 0.165 GeV.
pi0Loose	*pi0VeryLoose* candidates with: 0.10 GeV $< m_{\pi^0} <$ 0.16 GeV; $E_{lab} > 0.2$ GeV.
pi0LooseMass	*pi0Loose* candidates with: `Add4` fitter used to constrain mass, momentum and primary vertex.
mergedPi0Loose	Two *calorClusterNeutral* candidates with: merged π^0 consistency $> 1\%$.
pi0AllLoose	Combination of *pi0LooseMass* and *mergedPi0Loose*.

Table 4.4: A selection of the composite π^0 candidate lists stored in the *BABAR* event store database, where m_{π^0} is the mass of the π^0 candidate and E_{lab} is the candidate energy in the laboratory frame.

described below.

4.3.1 Event generator

The event generators simulate which particles are produced in an e^+e^- collision event and how they decay. There are several event generator packages for different physics processes. They are all controlled by the `GenFwkInt` package, which is the interface between the event generators and the *BABAR* framework. Any generator can also be run independently, without the detector simulation, using the `GeneratorsQA` package. The event generators output a set of 4-vectors to represent the decay products near the e^+e^- interaction. For all decay processes, the simulation of the photon radiative corrections are performed by the `PHOTOS` [48] algorithm. The generators most relevant to this work are:

- `JetSet`: Simulates the hadronic continuum ($u\overline{u}$, $d\overline{d}$, $s\overline{s}$ and $c\overline{c}$) events [49].
- `EvtGen`: Provides the default simulation of the decays of B mesons [50]. Different decay models, such as models which generate CP violating processes, can be added. It is also used to simulate the decays of charmed particles produced in the $c\overline{c}$ events generated by `JetSet`.

- `KK2F`: The `KK2F` package [51] generates $\tau^+\tau^-$, $\mu^+\mu^-$ and Bhabha events and the decays of the τ leptons are simulated by the `TAUOLA` [52] library. The `TAUOLA` package also simulates interference effects between resonances in τ decays.

- `AfkQed`: Simulates events which contain a hard initial state photon [53].

4.3.2 Detector simulation

The propagation of particles through the detector is simulated by the `Bogus` (*BABAR* Object-oriented `GEANT4`-based Unified Simulation) package, which is based on the `GEANT4` [54] toolkit. It takes as input the 4-vectors provided by the event generators, representing the decay products of the e^+e^- collision. `Bogus` simulates the energy loss, multiple scattering, interactions and decays of the generated particles as they pass through the simulated detector. `GEANT4` provides the physics processes and the means to describe the detector geometry. As these simulated particles pass through regions of the detector, their properties are used to calculate positions and idealised energy deposits in the detector, which are called '`GHits`' and are stored in the event store database.

The response of the detector to these particles is simulated by the `SimApp` application. It digitises the idealised `GHits`, transforming them into signals which mimic those created by the detector electronics. Real background events can be mixed in with the simulated signal events to reproduce the data signal more closely. The final output is a set of raw data objects called '`digis`', which each represent a simulated hit in the detector and are stored in the event store database.

4.3.3 Monte Carlo event reconstruction

The `Bear` package reconstructs the simulated events from the raw `digis`, retrieved from the events store database. The `digis` are combined into candidate events consisting of particle tracks, energy clusters and probable particle identifications. Most modules of the `Bear` package are shared with `ELF`, the equivalent reconstruction application for data (described in section 4.1.3).

There are two differences between `ELF` and `Bear`, the first being that `Bear` does not need to run the `TCtoDigiConversion` because the input is already in `digi` format. The second is that for the simulated events, the generated properties of the particles are known from before any detector simulation is applied. The

particles at the generator level are known as 'true' particles and their true particle type, momentum, energy and position are known as the 'MC truth information'. This information is retained throughout the reconstruction process and saved with the reconstructed simulated events in the event store.

4.3.4 `Moose`

The previous two sections have described an event simulation based on running three applications over the generated events: `Bogus`, `SimApp` and `Bear`. Each of these can be run separately, so long as the previous stage has been completed. To improve the speed of the simulation these are combined into a single executable called `Moose` (Monolithic Object-Oriented Simulation Executable). This allows the intermediate stages to be stored internally, so only the final event candidates are transfered to the event store.

4.4 Monte Carlo corrections

The simulated events do not perfectly imitate the data, resulting in differing reconstruction efficiencies between data and MC. In general, the simulation tends to reconstruct particles more efficiently, which may be due to problems during data taking that are not included in the simulation but do affect the data.

To adjust for this, various data/MC correction factors are applied to simulated events. The correction factors are calculated for each particle within the reconstructed event and they are multiplicative so the product of the corrections is used as the overall correction factor for the event.

Each correction has an associated uncertainty, which must be included in the overall systematic uncertainty of any measurement which uses these corrections.

4.4.1 Tracking efficiency corrections

The tracking efficiency and the associated data/MC correction factor is provided by a study of $\tau^+\tau^-$ pair events [55]. No tracking efficiency corrections need to be applied but there is a systematic uncertainty, of order 0.5% per track, which must be applied to each event. This systematic error does not need to be applied on an event-by-event basis, but can be included in the final systematic uncertainty at the end of an analysis. A systematic error on the reconstruction efficiency

correction is also required when using objects from the K^0_S composite candidate lists because they are reconstructed from tracks ($\pi^+\pi^-$).

4.4.2 Charged particle identification corrections

The PID selectors for charged particles are more efficient for MC than data. High purity samples of charged particles are used to calculate the PID selection efficiency and misidentification rates for different PID selectors in data and MC, and relative efficiencies are calculated to correct the MC simulation. The correction factor is a function of charged particle momentum and the polar angle in the lab frame, and is applied on a track by track basis. The systematic uncertainty on the PID correction is different for each PID selector and is applied at the end of the analysis.

4.4.3 Neutral particle reconstruction corrections

The reconstruction efficiency for neutral particles is higher in MC than in data. The neutral particle correction factor most relevant to this analysis is the correction on the π^0 detection efficiency. The correction is found by a study which calculates the ratio of the number of observed $\tau^- \to \rho^-\nu_\tau$ decays to the number of observed $\tau^- \to \pi^-\nu_\tau$ decays [56]. This is proportional to the π^0 reconstruction efficiency, and therefore taking the double ratio of this for data/MC produces the correction factor. The correction, C, is found as a function of π^0 momentum in the lab frame, $p_{\pi^0}(\mathrm{GeV}/c)$;

$$C = 0.9735 + 0.0062 p_{\pi^0}, \tag{4.2}$$

and is applied for each π^0 on an event-by-event basis. The associated systematic uncertainty on this correction is found by the same study to be 3% per π^0. Chapter 5 describes a new study of the π^0 correction efficiency which reduces the associated systematic uncertainty.

4.5 Skims

Once the event reconstruction detailed in the previous sections has been completed, the events are saved to the *BABAR* event store as the `AllEvents` data set.

Then the process of 'tagging' creates a database of boolean logic flags, called 'tag bits', which indicate whether or not an event has a particular characteristic. The `AllEventsSkim` data set is created when each event in the `AllEvents` data set is labelled with over one hundred tag bits.

The tag bits are used to quickly select events which share common characteristics; the resulting subset of data is called a 'skim'. To create a skim, the `SkimMini` package runs over the output from both `Bear` and `ELF`, selecting events which contain the desired set of tag bits. Many different skims are created and stored at *BABAR* computing sites across the world, with each designed to select the events required for a particular type of physics analysis. In the following chapters two skims are used, the `IsrLooseGamma` skim and the `Tau1N` skim, described below.

4.5.1 `IsrLooseGamma` skim

The `IsrLooseGamma` skim selects events intended for initial state radiation studies of light quark events. An event is selected if the following requirements are satisfied:

- The number of tracks in the *goodTracksLoose* list is at least 2.
- The total energy of the event is less than 14 GeV.
- The highest energy photon (in the *goodPhotonDefault* list with more than one EMC crystal hit) has energy above 3 GeV in the CM frame.

Approximately 1.21% of `AllEventsSkim` are selected by the `IsrLooseGamma` skim.

4.5.2 `Tau1N` skim

In $e^+e^- \to \tau^+\tau^-$ events the two τ leptons are produced back-to-back in the CM frame; therefore it is useful to divide the event into two hemispheres, with the decay products of each τ lepton in opposite hemispheres. The hemispheres are defined using a quantity called the 'thrust', where the 'thrust axis' of an event is defined as that along which the projected longitudinal momenta of the particles is maximised [57]. The magnitude of an event's thrust represents the alignment of particles within that event along a common thrust axis. When the magnitude of the thrust takes its lowest value, 0.5, it indicates a spherical distribution of

particles around the axis, whereas its maximum value of 1.0 indicates a jet-like arrangement along the thrust axis.

At *BABAR*, $\tau^+\tau^-$ events have a high thrust because a large amount of energy is available to each τ when they are produced, boosting the decay products in one direction and making the event more jet-like. On the other hand, $B\overline{B}$ events are produced almost at rest in the CM frame, giving them an isotropic, spherical distribution around the decay vertex, resulting in a low thrust. Therefore, thrust is an important variable for selecting $\tau^+\tau^-$ events, and the thrust axis of the τ decay products points roughly along the direction in which the τ was travelling when it decayed.

For the `Tau1N` skim, the thrust axis is defined using all the objects in the *calorClusterNeutral* list which have an energy above 50 MeV and all the objects in the *chargedTracks* list. In the CM frame, the events are divided into two hemispheres which are defined by the plane normal to the thrust axis. The 'hemisphere mass' is defined as the combined mass of all particles within each hemisphere which are used to define the thrust axis.

The `Tau1N` skim aims to select $\tau^+\tau^-$ events with a single track reconstructed in one hemisphere and three or more tracks in the other, which is referred to as a 1-N topology, where N is at least three. The topology of an event is a description of the multiplicity and distribution of tracks.

An event is selected for the `Tau1N` skim if the following requirements are satisfied:

- The number of tracks in the *chargedTracks* list is 10 or less.
- The number of neutral particles (with energy above 50 MeV) in each hemisphere is 6 or less to allow for up to three π^0s from each τ.
- The number of tracks in the *goodTracksVeryLoose* list is 1 in one hemisphere and at least 3 in the other.
- The hemisphere mass is less than 3 GeV per hemisphere.

Tracks from photon conversions are included in the *chargedTracks* list but most are not in the *goodTracksVeryLoose* list which requires the track to originate at the interaction point.

Approximately 4.37% of `AllEventsSkim` are selected by the `Tau1N` skim. The skim selection rates for the `Tau1N` skim are provided in table 4.5.

	Skim rate
Data sample	4.4%
MC samples	
$\tau^+\tau^-$	16.0%
$\mu^+\mu^-$	0.1%
$b\overline{b}$	1.3%
$c\overline{c}$	5.7%
$u\overline{u}$ $d\overline{d}$ $s\overline{s}$	7.3%
Bhabha	1.5%

Table 4.5: The selection rates of the `Tau1N` skim[58] for data and various MC samples.

4.6 Physics analysis

The different types of physics analysis are divided between a number of Analysis Working Groups which each have their own packages, skims and computing resources. The tools that are needed to perform analysis, such as those discussed throughout this chapter, are developed and maintained by various Tools Groups. The Data Quality Group is responsible for checking the data, the construction of the datasets and validating new MC releases, while the validation of new releases or new Run periods is coordinated by the Validation Board.

Physics analysis at *BABAR* is mostly done using `Root` [59], an object-oriented data analysis framework written in the C++ language. It is designed to efficiently handle large volumes of data, providing the set of tools and features required for High Energy Physics analysis. Particle candidates are written as objects and the properties are accessed using different methods.

Chapter 5

The π^0 detection efficiency

This chapter describes how initial-state radiation (ISR) events of the type $e^+e^- \to \gamma\pi^+\pi^-\pi^0$, with 3π final states near the ω resonance, have been used to measure the π^0 detection efficiency at *BABAR*. Section 5.1 outlines the motivation for this study while section 5.2 provides the required theory on initial-state radiation. The selected events are described in section 5.3 while the features and fitting of the $\pi^+\pi^-\pi^0$ mass spectra are outlined in section 5.4. Section 5.5 explains how the π^0 efficiency is calculated, section 5.6 describes the systematic uncertainties and section 5.7 summarises the study.

5.1 Motivation for the study

When a π^0 candidate list is used in an analysis, a correction may need to be applied to the MC to correct for any difference between MC and data, as described in section 4.4. Previous studies [56] have indicated that the MC simulation overestimates the π^0 detection efficiency of *BABAR*. Currently a correction factor of $\sim$0.98 is applied to each MC event, for each π^0 in the event. The systematic uncertainty on this correction factor is 3%, and so there is a contribution to the overall systematic uncertainty on any *BABAR* measurement of 3% per π^0, due to the limited knowledge of the π^0 detection efficiency.

This systematic uncertainty needs to be reduced to make many *BABAR* measurements more competitive with previous experiments, and with the Belle experiment. This is particularly important in τ physics; LEP, for example, measured several τ branching fractions with uncertainties well below 1%. *BABAR* has much higher statistics and so can compete in measurements of small branching frac-

tions. However the errors on many τ decay modes with relatively small branching fractions are dominated by the systematic errors, and where the modes involve π^0 particles, these systematic uncertainties can be dominated by the uncertainty on the π^0 detection efficiency correction. For the analysis described in chapter 7, this is an important source of systematic uncertainty.

The aim of the work presented in this chapter is to reduce the systematic uncertainty on the π^0 detection efficiency down to 1% or less, using the very high statistics samples of ISR events available at *BABAR*.

5.2 Initial-state radiation

The e^+e^- annihilation cross section as a function of CM energy is shown in figure 5.1. The e^+e^- beam particles at *BABAR* may annihilate to produce a virtual photon which couples to neutral vector meson resonances, as shown in figure 5.2. With initial-state radiation the effective CM energy of the hadronic system is reduced. In $e^+e^- \to \pi^+\pi^-\pi^0\gamma$ the 3π amplitude is a sum of the contributions from the isoscalar vector meson resonances which have the same quantum numbers as a photon: $\omega(782)$, $\phi(1020)$, higher mass ω' states and other possible contributions. The ω has an 89% branching fraction to $\pi^+\pi^-\pi^0$, so this study uses the mass region in the $\pi^+\pi^-\pi^0$ final state dominated by the $\omega(782)$ amplitude. The $\pi^+\pi^-\pi^0$ mass region between 0.7 GeV and 0.86 GeV will be referred to as the ω region and the peak (which is affected by interference terms from the higher resonances, and particularly the $\phi(1020)$) is called the ω peak.

ISR events can be generalised as $e^+e^- \to X + \gamma$. In the CM frame, the ISR photon has an energy (E_γ) given by

$$E_\gamma = \frac{1}{2\sqrt{s}}(s - m_X^2), \tag{5.1}$$

where $\sqrt{s}$ is the invariant mass of the entire system and m_X is the mass of the hadronic final state.

The Lorentz boost to the system from the asymmetric beam energies imposes a relationship between the photon energy and its polar angle θ in the laboratory frame. Figure 5.3 shows the photon energy in the laboratory frame versus $\cos\theta$ and the relationship is observed as the dense curved region. From kinematics the ISR photons must have laboratory energy between 3 GeV and 9 GeV. The "ISR

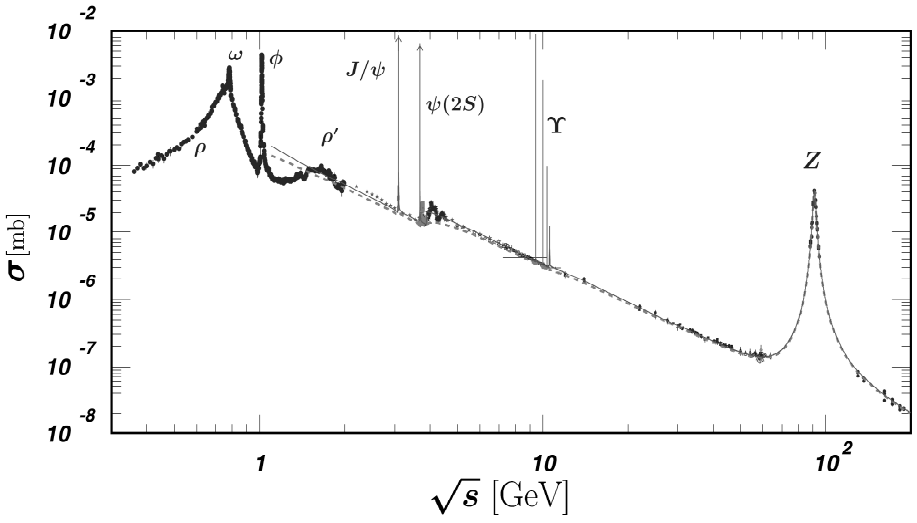

Figure 5.1: World data on the total cross section, σ, of $e^+e^- \to hadrons$ versus the CM energy, $\sqrt{s}$. The large cross section for the regions dominated by low-mass vector mesons is shown. At *BABAR*, initial-state radiation can lower the effective CM energy to these energies [15].

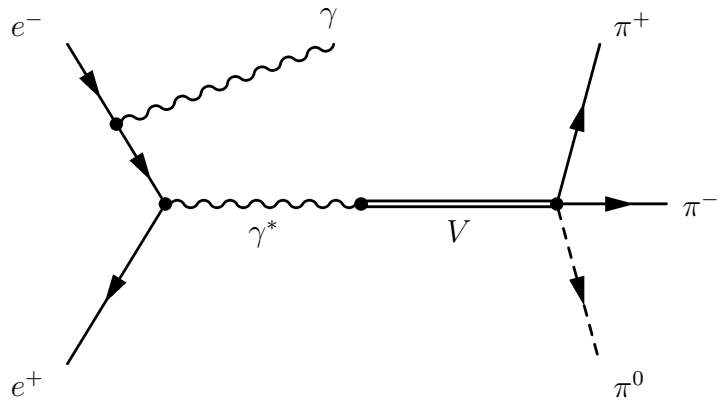

Figure 5.2: Diagram of an initial-state radiation event producing three pions. After emitting the initial-state photon (γ) the e^+e^- pair annihilate, producing a virtual photon (γ^*) which decays via neutral vector resonances, V. The overall amplitude is the sum of the resonance contributions, including ω, ϕ and others. Note that the resonances, V, must have the same quantum numbers as the virtual photon.

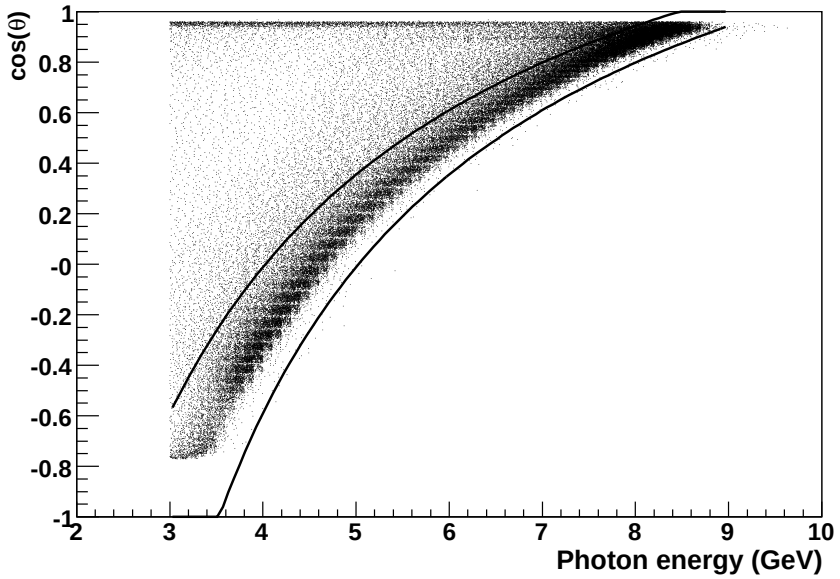

Figure 5.3: The photon energy versus the cosine of the polar angle of the photon in the laboratory frame, for reconstructed MC events, selected as described in section 5.3.3. The ISR photons are evident as the curved dark band. The two solid lines define the ISR region, the area within 0.5 GeV of the expected ISR curve.

region" is defined as the area on figure 5.3 within 0.5 GeV of the expected ISR curve, indicated by the two solid lines. All events with a photon in the ISR region are selected as potential ISR events.

5.3 Event selection

5.3.1 Overview of analysis procedure

In essence the analysis procedure is as follows. ISR events with one positive and one negatively charged track are selected, and a 1C kinematic fit is performed, also using the beam parameters, to the hypothesis of a single missing π^0. Events which have a fit probability greater than 5% are deemed to have an "inferred" π^0. Within this sample events are classified as either "seen" or "unseen", depending on whether the inferred π^0 matches with a reconstructed π^0 candidate. The ω peaks in the $\pi^+\pi^-\pi^0$ mass spectra, for ranges of π^0 energy, are then fitted simultaneously in the seen and unseen samples in order to count the numbers of

contributing ω events. When constructing effective masses, only the inferred π^0 energies and momenta are used; the properties of the reconstructed π^0 candidates are only used to match with the inferred π^0.

The π^0 detection efficiency is taken as the ratio of the number of seen to (seen + unseen) ω events. These efficiencies are found for both data and MC, and the ratios of the data efficiencies to the MC efficiencies are taken to give the π^0 detection efficiency correction factors, needed to correct the MC simulation to the data. For this study the detection efficiency is defined as the probability of finding a π^0 candidate in the *pi0Loose* candidate list (described in section 4.2.4) when a true π^0 is present.

5.3.2 Data and Monte Carlo Samples

This study uses 398 fb^{-1} of on-peak ($\sqrt{s}$ = 10.58 GeV) e^+e^- collision data taken in *BABAR* Runs 1 to 6 (described in section 4.1.1). Less data are used than described in section 4.1.1 because this study was performed before the end of Run 6. With an integrated luminosity of 132.6 fb^{-1}, Run 5 has the highest statistics; since the results are consistent for all Runs, some of the plots are shown for Run 5 only.

MC samples of $e^+e^- \to \pi^+\pi^-\pi^0\gamma$ were generated using the `AfkQed` generator which is described in section 4.3.1. In total 9.7×10^6 events were simulated and processed through the full detector simulation and reconstruction software. Again, some of the plots are shown for Run 5 only (a sample of 3.3×10^6 generated events) for direct comparison with the data.

5.3.3 Event selection

The *IsrLooseGamma* skim, as described in section 4.5, is used. The tracks are assigned as π^+ and π^- particles (according to their charge) if they meet the following criteria:

- the track is included in the *chargedTracks* candidate list (comprising all reconstructed tracks, as described in section 4.2.1).
- the polar angle of the track is between 0.4 radians and 2.42 radians.
- the track has a ratio of energy to momentum (E/p) which is less than 0.9 (to suppress radiative Bhabha events).

- the track has transverse momentum greater than 0.1 GeV/c.

The neutral clusters are assigned as ISR photons if they meet the following criteria:

- the neutral cluster is included in the *calorNeutral* list (comprising single energy clusters with no associated track, as described in section 4.2.2).
- the neutral cluster has an energy in the laboratory frame of at least 3 GeV.
- the angle between the energy-weighted centroid of the neutral cluster and the z-axis is within the 'ISR region' defined in section 5.2.

Events are selected for further analysis if they have exactly one π^+, one π^- and one ISR photon.

For this study the *pi0Loose* candidate list provides a list of reconstructed π^0 candidates for each event, as described in section 4.2.4. The π^0 candidates in the *pi0Loose* list are referred to as "detected" π^0s (recognising of course that many such candidates do not come from true π^0s). There are no requirements on the number of detected π^0s in each event so selected events may have any number of such candidates, including zero.

5.3.4 Kinematic fitting

The $\pi^+\pi^-\gamma$ system for the selected events is reconstructed (ignoring any detected π^0 particles), with the missing 4-momentum calculated as that of the original e^+e^- system minus the the 4-momentum of the $\pi^+\pi^-\gamma$. Kinematic fitting is then performed (using TreeFitter, as described in section 4.2.4), constraining the missing 4-momentum to belong to a single π^0. The distribution of the resulting fit probability is shown in figure 5.4 for Run 5 data and MC events. Events are required to have a fit probability greater than 0.05. All selected events at this stage therefore have exactly one inferred π^0, but may have any number of detected π^0s in the *pi0Loose* candidate list.

5.4 The $\pi^+\pi^-\pi^0$ mass spectrum

The $\pi^+\pi^-\pi^0$ system is now reconstructed using the inferred π^0, and the mass spectra are plotted in bins of inferred π^0 energy: 13 bins between 0.2 GeV and

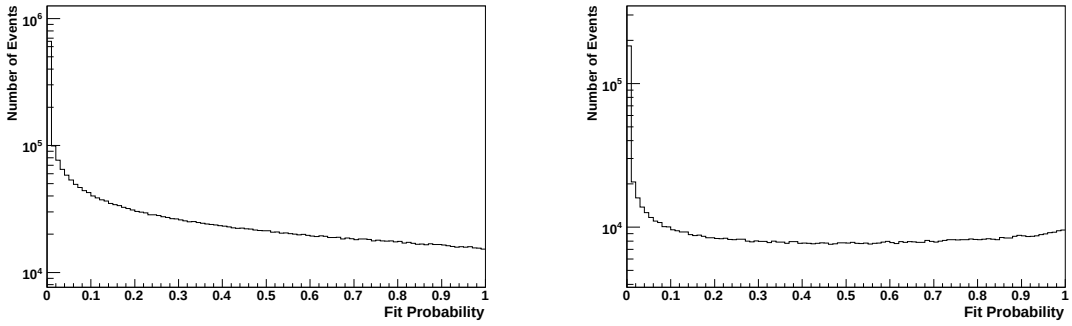

(a) (b)

Figure 5.4: The fit probability for the kinematic fit to a single missing π^0 for Run 5 (a) data and (b) MC events, on a logarithmic scale.

4.0 GeV. Examples of these spectra are shown for Run 5 in figures 5.6 and 5.7, where the mass peaks are seen in the ω and ϕ resonance regions. In order to count a sample of true (i.e. genuine) π^0s in the inferred samples, the mass spectra are fitted to obtain the intensity of the peak within the ω region. To find the π^0 efficiency, the events are divided into two subsets: events where the π^0 is "seen" in the list of reconstructed π^0 candidates, and events where the π^0 is "unseen" i.e. not in the list of π^0 candidates. The efficiency, ϵ, of detecting the π^0 is then given by

$$\epsilon = \frac{S}{S+U}, \tag{5.2}$$

where S is the number of events in the ω resonance peak for which the π^0s are seen and U is the number for which the π^0s are unseen. This can be rearranged to give a relationship between S and U in terms of ϵ:

$$\epsilon S = (1-\epsilon)U. \tag{5.3}$$

The 3π mass spectra for the seen and unseen samples are fitted simultaneously including the efficiency, ϵ, as a fit parameter.

5.4.1 The matching region

To recap, each selected event has a single inferred π^0, obtained from the kinematic fit. The seen π^0 events are defined to be those where the inferred π^0 was detected and reconstructed, and the unseen π^0 events are those where there is no matching

π^0 candidate in the *pi0Loose* list. Each event may have any number of detected π^0 s, any of which could match the inferred π^0. The matching criteria need to be defined to decide whether a detected π^0 is deemed to be the same particle as the inferred π^0.

The two-dimensional distribution of difference in energy, ΔE, versus angle in space, α, between the inferred and detected π^0 s is shown in figure 5.5 for data, where each point on the plot represents one detected π^0. A rather loose "matching region" is defined as ΔE from -0.6 to 0.6 and α from 0.0 to 0.6. Within this region the inferred and detected π^0 s are deemed to match, and the event is marked as a "seen" π^0 event. If none of the detected π^0 s matches the inferred π^0 (or if there are no detected π^0 s), then the event is marked as an "unseen" π^0 event.

It is possible for more than one detected π^0 to match the inferred π^0, but only the inferred π^0 s are used to reconstruct the $\pi^+\pi^-\pi^0$ system. The size of the matching region will affect the resulting value of the efficiency: the smaller the region, the lower the measured efficiency. However, since the primary interest is in efficiency ratios between data and MC, as long as the matching region is the same in MC and data, the final results are relatively insensitive to the matching criteria (see section 5.6).

5.4.2 The line shape in the ω peak region

The 3π mass resolution is obtained using the MC truth information (as described in section 4.3.3). For this, MC events must pass the selections described in sections 5.3.3 and 5.3.4 and contain one true π^+, one true π^- and one true π^0. Histograms are made of the difference between the reconstructed $\pi^+\pi^-\pi^0$ mass (using the inferred π^0 from the kinematic fit) and the true $\pi^+\pi^-\pi^0$ mass (using the truth particles). Since the mass resolution varies with mass, only events with true $\pi^+\pi^-\pi^0$ mass between 0.7 GeV and 0.86 GeV (the ω region) are used. These mass resolution distributions are made in bins of π^0 energy. To reduce the statistical variations the histograms are smoothed using the multiquadratic smoothing procedure [60].

To obtain the shape of the peak in the ω mass region, the `AfkQed` generator (described in section 4.3.1), without the detector simulation, is used to generate the required ISR process and simulate the $\pi^+\pi^-\pi^0$ mass spectra around the ω mass. Within the `AfkQed` generator, the relative phase between the ω and ϕ

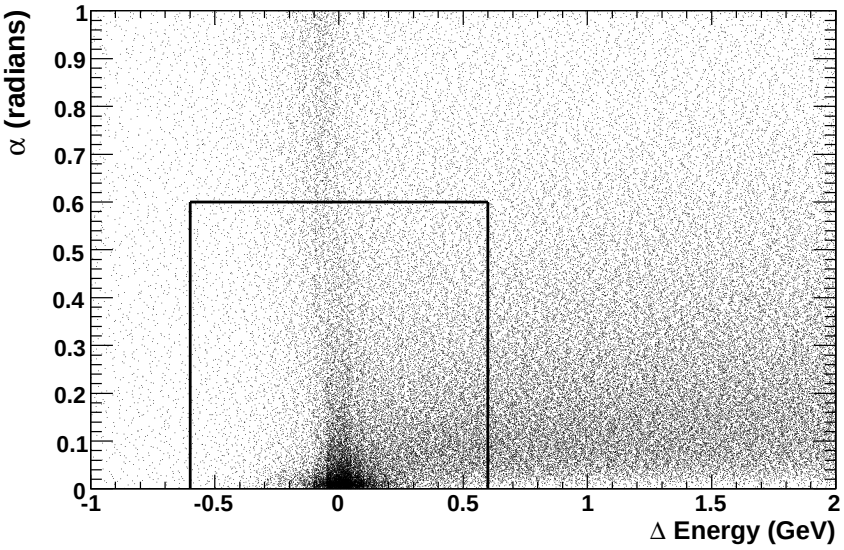

(a)

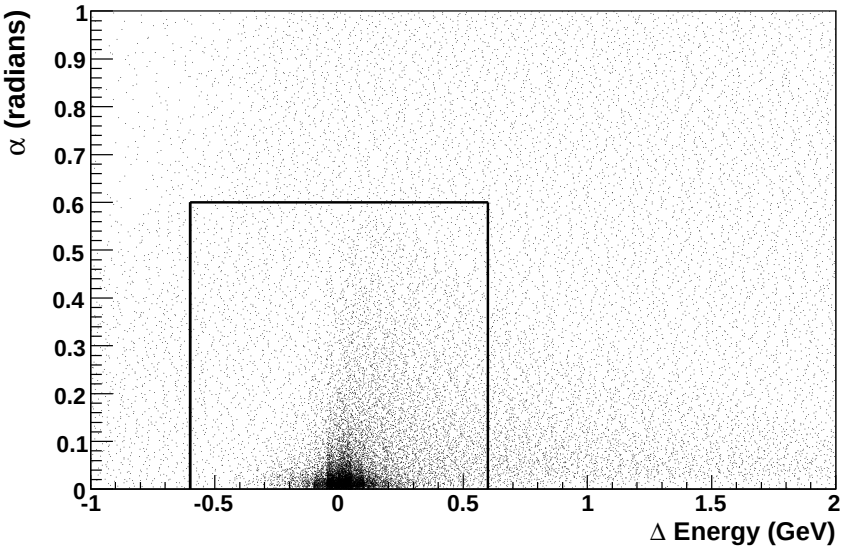

(b)

Figure 5.5: The difference in energy, ΔE, against the angle, α, between the inferred and detected π^0 particles for Run 5 (a) data and (b) MC events. The lines define the matching region, in which the inferred and detected π^0s are considered to be the same particle.

amplitudes is 155°. These generated spectra need to be folded with the detector resolution before being used as input to the fits to the reconstructed 3π mass spectra in data and Monte Carlo. So for each bin of π^0 energy, the generated $\pi^+\pi^-\pi^0$ mass spectrum is convoluted with the smoothed mass resolution. The area under the curve is normalised to unity to give the expected shapes of the resonance peaks.

The $\pi^+\pi^-\pi^0$ mass binning is chosen to be 1 MeV for each of the mass resolution, smoothed mass resolution, generated mass spectra and the convolved spectra. The reconstructed $\pi^+\pi^-\pi^0$ mass spectra have bins of 0.01 GeV over a range from 0.6 GeV to 0.95 GeV.

Attempts were made to describe the mass resolution by various functions, including a Cauchy distribution, which could be folded analytically with the expected 3π line shape. However, they do not describe the shape of the mass resolution sufficiently well, and the numerical approach described above is required to obtain good fits to the MC mass spectra.

5.4.3 Fitting the $\pi^+\pi^-\pi^0$ mass spectra

For the $\pi^+\pi^-\pi^0$ mass spectra, the position of the ω peak is found initially by fitting the region around the peak with a Gaussian function. The difference in ω peak position between the reconstructed and generated $\pi^+\pi^-\pi^0$ mass spectra is called the 'mass shift', and is found to be independent of π^0 energy. For the MC sample the mass shift is 0.4 MeV while no mass shift is seen in the data.

The shape determined as described in section 5.4.2 is fitted simultaneously to the ω region peaks in each of the seen and unseen samples, for each bin of π^0 energy, for each Run, for the data and MC samples. In the fits, the fitted function is shifted along the x-axis by the 'mass shift' described above. A free parameter ϵ represents the π^0 detection efficiency (as described at the start of section 5.4), and is applied as a factor ϵ multiplying the peak intensity in the seen π^0 event samples and as a factor of $1-\epsilon$ in the unseen π^0 event samples. Thus the efficiency and the error on the efficiency come directly from the simultaneous fits to the seen and unseen samples. There is one free parameter, N, for the overall scale of the resonance peaks, and a further three free parameters to define the backgrounds, which are modelled by Weibull functions[1]. This gives a total of 8 free parameters

[1]The Weibull distribution is $A(x/b)^{a-1}e^{-(x/b)^a}$ where x is the $\pi^+\pi^-\pi^0$ mass minus the threshold mass, a and b are parameters which define the shape and A is the normalisation

for each simultaneous fit. The fits are done over a relatively narrow mass range to avoid the influence of the $\phi(1020)$ and higher mass resonances. Since the peak shapes are fixed in the fits, restricting the mass range in this way does not allow any significant additional freedom in the shapes of the backgrounds.

Figures 5.6 and 5.7 show examples of the fits to the mass spectra for the Run 5 MC and data samples. Each figure shows the lowest and highest π^0 energy bins as well as a mid-range π^0 energy bin. For each π^0 energy bin there are two mass spectra, for the seen and unseen π^0 events, and the ratio of χ^2 to the number of degrees of freedom (χ^2/NDF) is given underneath each pair. There is a total of 156 independent simultaneous fits for all Runs of data and MC.

5.5 The π^0 efficiency correction factor

The π^0 detection efficiencies, ϵ, are shown as a function of π^0 energy in figure 5.8 for data and MC events. There are enough events to measure the efficiency for π^0 energies between 0.2 GeV and 4.0 GeV.

Figure 5.9(a) shows the π^0 efficiency correction factor as a function of π^0 energy for Run 5, where the efficiency correction factor is the ratio of the efficiency found for data divided by the efficiency for MC. The overall correction efficiency factor is found to be 1.01 ± 0.01, assuming it is constant with energy.

5.5.1 Number of matching neutral clusters

In this procedure, fake π^0 s may match the inferred π^0, potentially causing events to be falsely classified as seen. Indeed some events with low inferred π^0 energy, below about 1 GeV, have several matches, although as long as one of the matches is correct then the event will be correctly classified. However, some events will be classified as seen even when the π^0 is not properly reconstructed. To first order, this effect should cancel in the ratio of data to MC efficiencies, although the relative numbers of fake reconstructed π^0 s are slightly different in data and MC.

To investigate further, the number of neutral clusters, N_γ, with the following properties is counted:

- the neutral cluster has an energy greater than 30 MeV.

parameter.

Seen π^0 events: Unseen π^0 events:

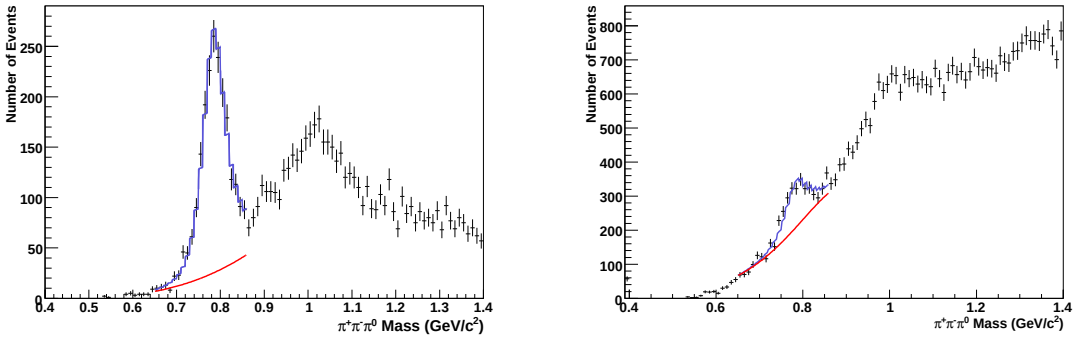

(a) π^0 energy between 0.2 GeV and 0.4 GeV. The χ^2/NDF is 48/37.

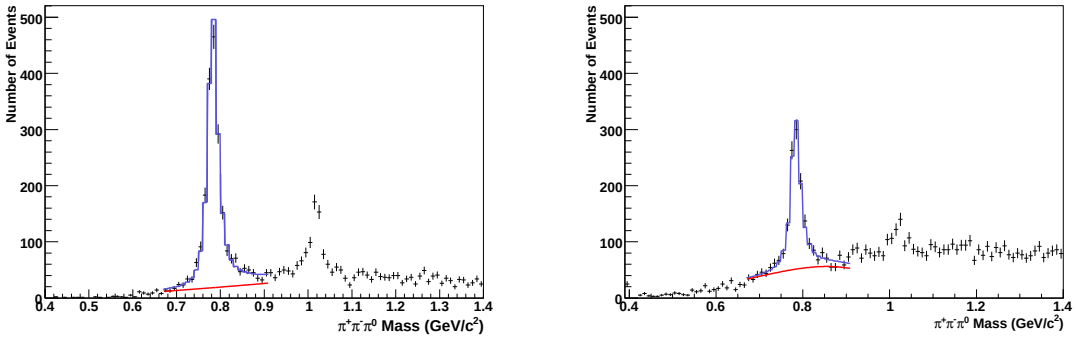

(b) π^0 energy between 1.8 GeV and 2.0 GeV. The χ^2/NDF is 37/40.

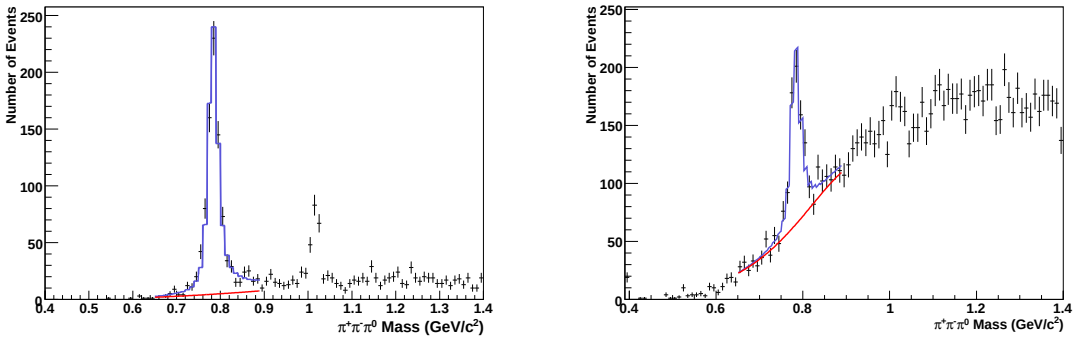

(a) π^0 energy between 3.5 GeV and 4.0 GeV. The χ^2/NDF is 48/38.

Figure 5.6: A selection of $\pi^+\pi^-\pi^0$ mass spectra from the Run 5 data sample, using seen and unseen π^0 events for different π^0 energies. The black crosses show the data, the blue histogram is the fitted function and the red curve is the background component of the fit.

Seen π^0 events: Unseen π^0 events:

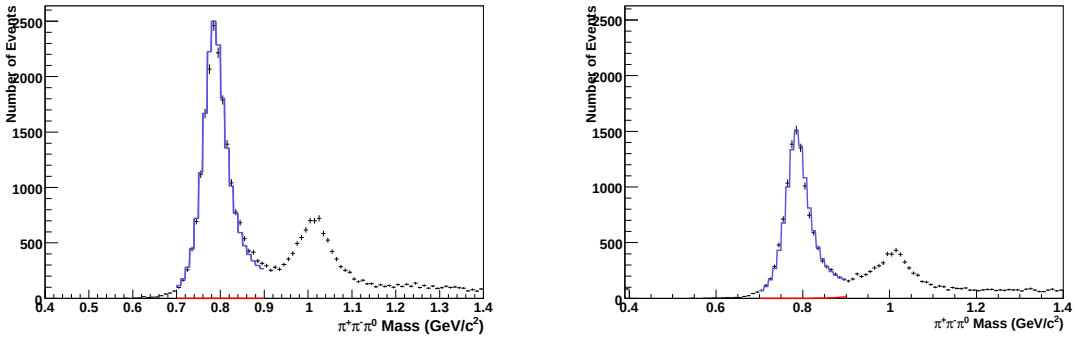

(a) π^0 energy between 0.2 GeV and 0.4 GeV. The χ^2/NDF is 101/35.

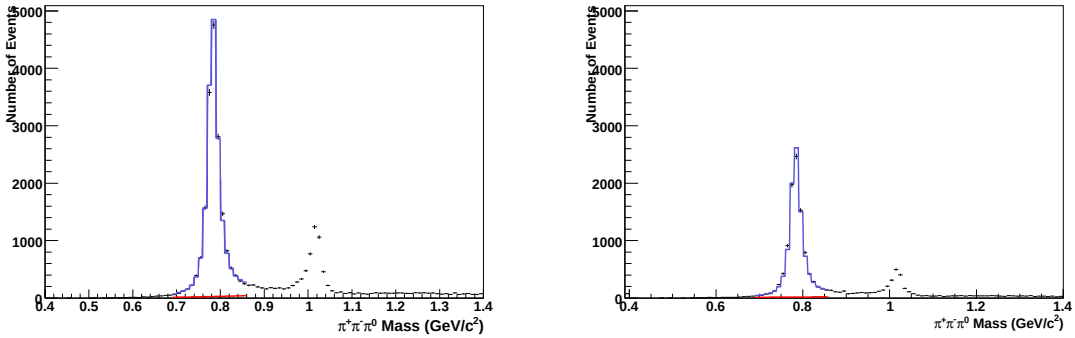

(b) π^0 energy between 1.8 GeV and 2.0 GeV. The χ^2/NDF is 66/26.

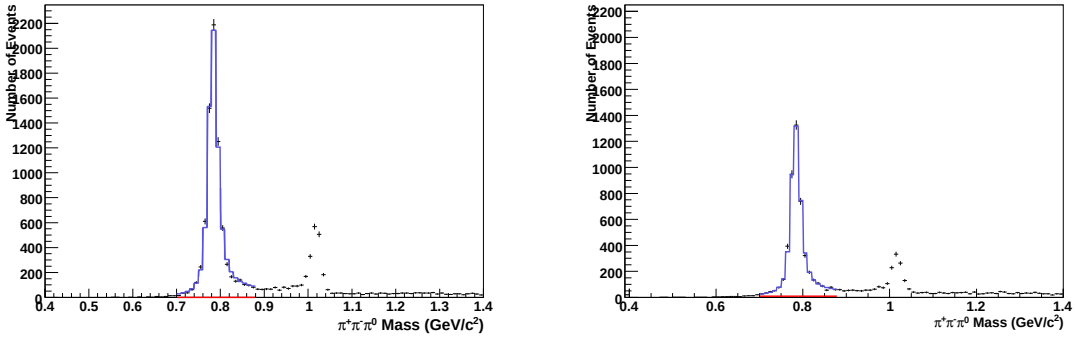

(a) π^0 energy between 3.5 GeV and 4.0 GeV. The χ^2/NDF is 59/28.

Figure 5.7: A selection of $\pi^+\pi^-\pi^0$ mass spectra from the Run 5 MC sample, using seen and unseen π^0 events for different π^0 energies. The black crosses show the MC, the blue histogram is the fitted function and the red curve is the background component of the fit.

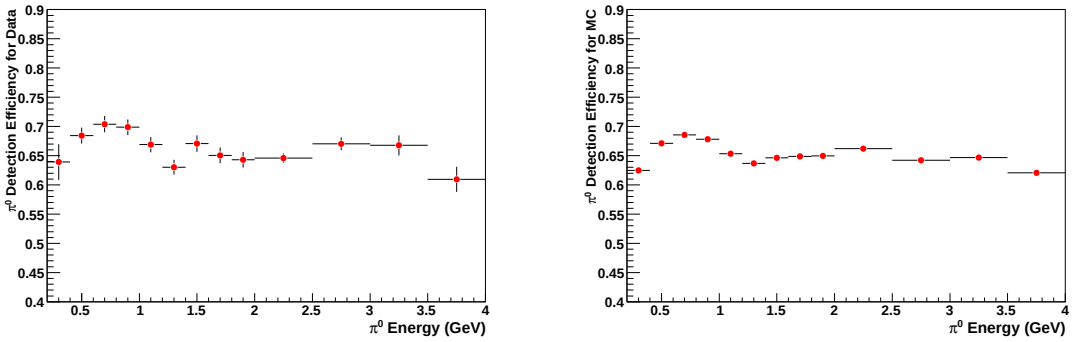

(a) (b)

Figure 5.8: The Run 5 π^0 detection efficiency versus π^0 energy for (a) data and (b) MC events.

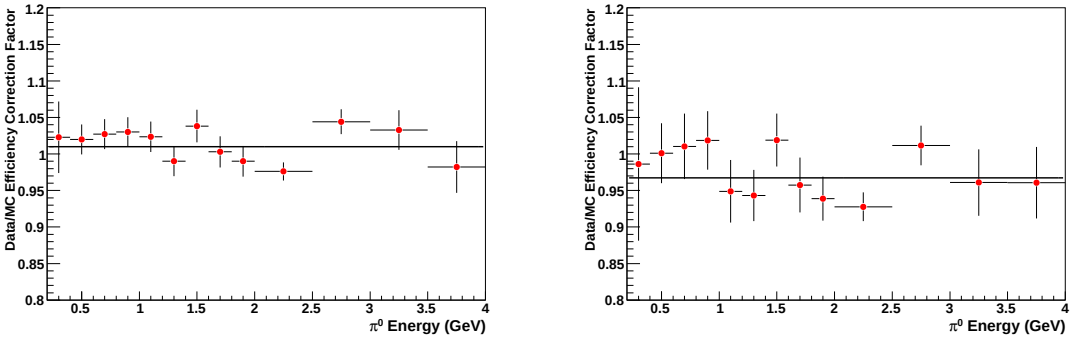

(a) (b)

Figure 5.9: (a) Run 5 π^0 detection efficiency correction versus π^0 energy (the fitted constant is 1.01 ± 0.01 and χ^2/NDF is 18.8/12); (b) for $N_\gamma \leq 2$, where N_γ is the number of neutral clusters in the event, excluding the ISR photon (the fitted constant is 0.97 ± 0.01 and χ^2/NDF is 13.6/12).

- the neutral cluster has an energy less than 3 GeV (the cut-off to define ISR photons).
- the polar angle of the neutral particle is between 0.24 and 2.4 radians.

The analysis is repeated for Run 5 with the requirement $N_\gamma \leq 2$ (in addition to the previous cuts). Thus there can only be a single π^0 in each event, and multiple matches cannot occur (though it could still be the "wrong" π^0).

Figure 5.9 shows the Run 5 efficiency ratio with and without the cut on N_γ. The overall correction factor shifts down from 1.01 ± 0.01 to 0.97 ± 0.01 when

the cut is applied, constant across the range of π^0 energy. Any effect from the multiple matches or false matches would only be seen at lower energies, but no extra effect is seen. The lower value for the efficiency ratio is presumably due to the fact that data tends to have more additional background neutral clusters than MC, and so restricting to a sample with few neutral clusters reduces efficiency in data by slightly more than it does in MC. Since the primary aim is an unbiased measure of the efficiency correction factor for the *pi0Loose* candidate list, the cut on N_γ is not used.

5.5.2 The π^0 efficiency correction factor over Runs 1 to 6

Figure 5.10 shows the efficiency correction factor versus Run number for each bin of π^0 energy, over Runs 1 to 6. There is no evidence for any Run-by-Run variation; each plot is fitted with a horizontal line.

A histogram of the χ^2 values from these 13 fits is shown in figure 5.11. The dotted line shows the expected distribution of the χ^2 for 13 independent fits with 5 degrees of freedom. The good agreement is an indication that the efficiency correction is indeed constant over Runs 1 to 6, and suggests that the fits to determine the efficiency ratios, as well as their statistical uncertainties, are generally reliable (although this is discussed further below).

In figure 5.12 the weighted average of the efficiency correction over Runs 1 to 6 is plotted against π^0 energy. The question arises as to whether the efficiency correction is consistent with being constant with π^0 energy. A fit to a constant value gives a χ^2/NDF of 37/12. While there is evidence in figure 5.12 for a rise in the efficiency correction factor at low energies, this is less evident when the six Runs are examined individually. The efficiency correction for Run 5 (as seen in figure 5.9(a)), which has the largest statistics, appears flat at low π^0 energies. The other Runs each have one bin which has a higher efficiency correction at a low π^0 energy. This may be due to statistical fluctuations, or could be a genuine dependence on the π^0 energy.

Without clear evidence for a π^0 energy dependence of the efficiency correction, it is assumed that there is none, and the error scaling procedure used by the Particle Data Group [15] is adopted to take into account the possibility that the individual fit errors may be too small or that there is a small energy dependence.

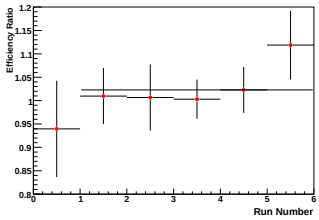

(a) 0.2 GeV to 0.4 GeV.

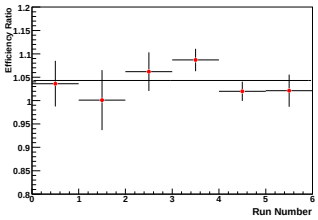

(b) 0.4 GeV to 0.6 GeV.

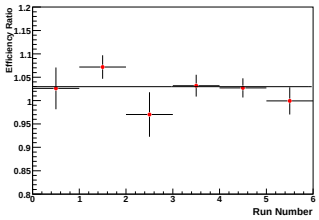

(c) 0.6 GeV to 0.8 GeV.

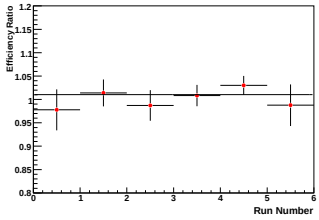

(d) 0.8 GeV to 1.0 GeV.

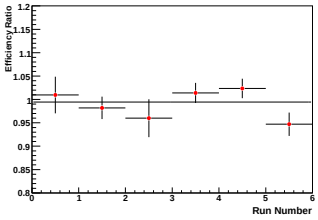

(e) 1.0 GeV to 1.2 GeV.

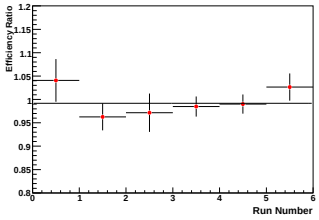

(f) 1.2 GeV to 1.4 GeV.

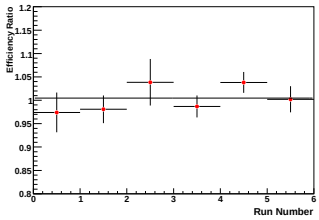

(g) 1.4 GeV to 1.6 GeV.

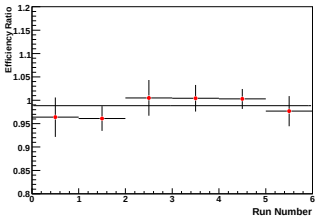

(h) 1.6 GeV to 1.8 GeV.

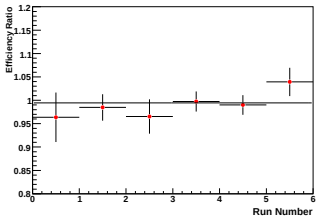

(i) 1.8 GeV to 2.0 GeV.

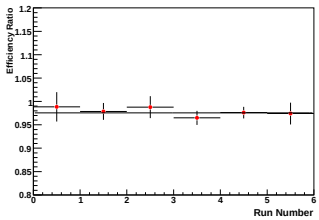

(j) 2.0 GeV to 2.5 GeV.

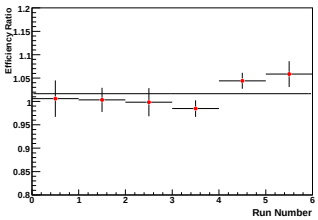

(k) 2.5 GeV to 3.0 GeV.

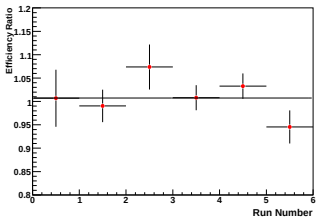

(l) 3.0 GeV to 3.5 GeV.

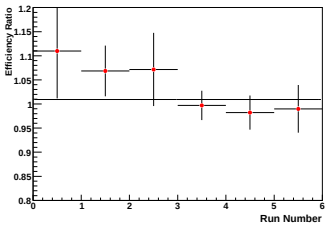

(m) 3.5 GeV to 4.0 GeV.

Figure 5.10: The efficiency correction factor as a function of Run number, for different ranges of π^0 energy (given underneath each plot). The plots are each fitted with a constant; the χ^2 values are shown in figure 5.11 and the fitted constants are shown in figure 5.13.

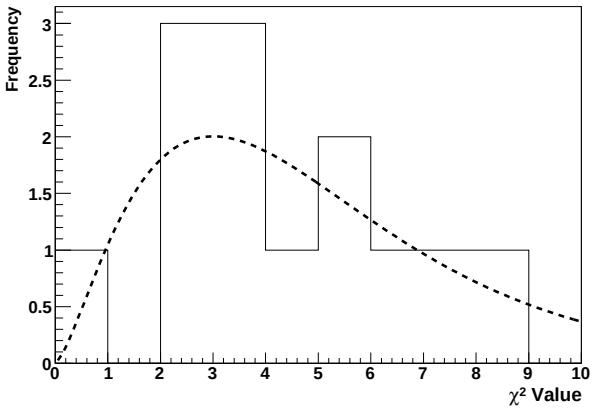

Figure 5.11: A plot of the χ^2 values from the fits of the efficiency correction over Runs 1 to 6 (from figure 5.10). The dotted line shows the expected distribution of χ^2 values from 13 independent fits with 5 degrees of freedom.

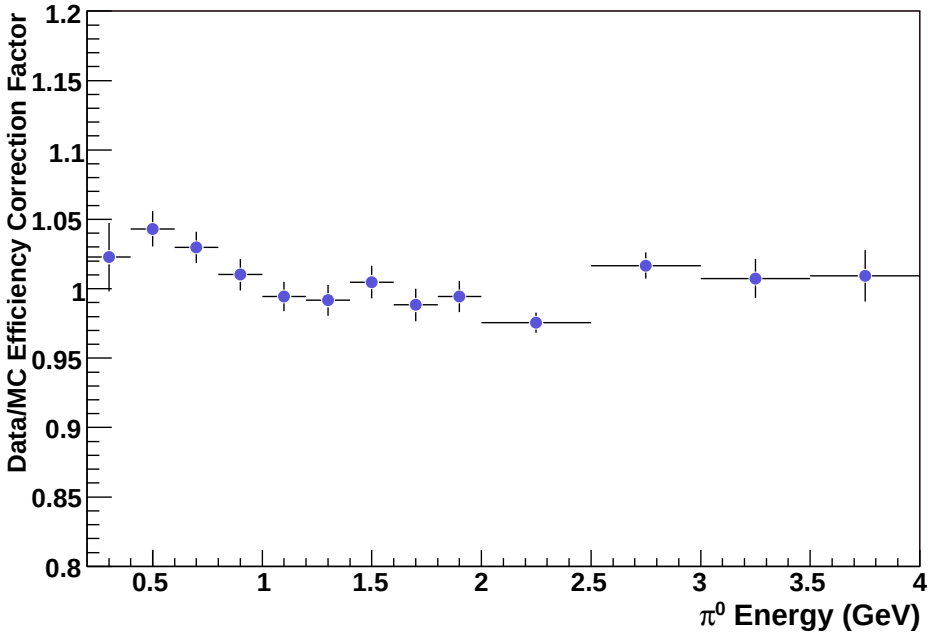

Figure 5.12: The *pi0Loose* list efficiency correction factor for Runs 1 to 6.

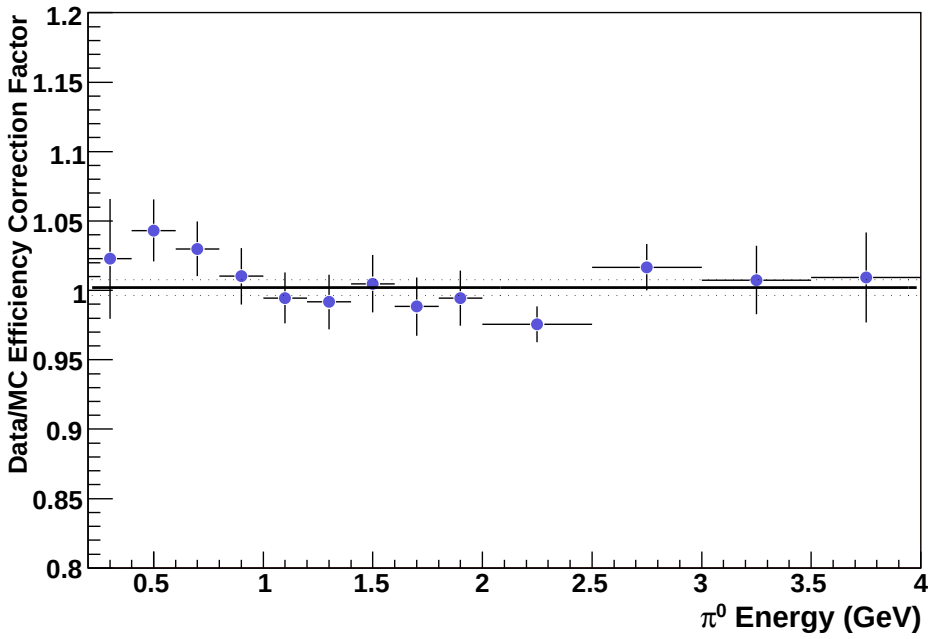

Figure 5.13: The *pi0Loose* list efficiency correction factor for Runs 1 to 6, with scaled errors. The errors are scaled by 1.75 to give χ^2/NDF equal to 12.0/12. The distribution is fitted with a constant of 1.0020 ± 0.0055.

The scale factor, S, is given by

$$S = \sqrt{\frac{\chi^2}{NDF}} = \sqrt{\frac{37}{12}} = 1.75. \tag{5.4}$$

All the input errors from figure 5.10 are scaled by S, giving the result shown in figure 5.13. The χ^2 becomes 12.0, equal to the value of NDF. The fit gives an overall efficiency ratio of 1.0020 ± 0.0055; the central value is unchanged while the uncertainty is scaled by S. The statistical error of 0.55% takes into account the uncertainty in the shape of the energy dependence.

5.6 Systematic uncertainties

The following variables are investigated as possible sources of systematic uncertainty on the efficiency correction:

- The fit probability cut (introduced in section 5.3.4).

- The size of the matching region, defined by ΔE and α (introduced in section 5.4.1).
- The ω-ϕ phase (introduced in section 5.4.2); the most precise recent experimental measurement of the ω-ϕ phase is 164±3° [61], and the ω-ϕ phase is therefore changed to a value of 170° as a systematic check.
- The 'mass shift' in MC and data (introduced in section 5.4.3).
- The fitting range for the fit to the ω peak in the $\pi^+\pi^-\pi^0$ mass spectra (introduced in section 5.4.3).
- The $e^+e^- \to u\overline{u}/d\overline{d}/s\overline{s}$ (known generally as $e^+e^- \to uds$) and $e^+e^- \to \omega\pi^0\nu$ background modes.

These checks are done using the Run 5 data and MC samples, with the errors treated following the recommendations of [62]. Let the overall efficiency correction factor be $a \pm \sigma_a$. One at a time, each quantity is varied to give a new value of the efficiency correction factor, $b \pm \sigma_b$. The difference is $D = a - b$, and the values of a and b are of course correlated. The error on D is computed as $\sigma_D = \sqrt{\sigma_a^2 - \sigma_b^2}$.

The value of D is obtained for each π^0 energy bin, and no clear systematic pattern with π^0 energy is found for any of the quantities studied. The weighted averages of D are taken over all π^0 energies and shown in figure 5.14 for each systematic check.

As a percentage variation, $100|D|/a$, all systematic effects on the overall efficiency correction factor are below the 1% level. Figure 5.14 shows that most of the values of D are consistent with zero. However, fitting with a constant gives a χ^2/NDF of 32.5/14, indicating that some values are significant.

Three of the variables have values of D which are more than two standard deviations away from zero: the mass shift in data; ΔE for the matching region; and $e^+e^- \to \omega\pi^0$ background events. These cause percentage variations in the efficiency correction ($100|D|/a$) of 0.26%, 0.57% and 0.05% respectively. Removing these three lowers the χ^2/NDF to 11.7/11, and gives a fitted constant of 0.0004 ± 0.0004. Therefore, it is concluded that these three should be treated as significant systematic uncertainties and the percentage variations for these values are added in quadrature to give an overall systematic uncertainty of 0.63%.

The three sources of systematic uncertainties found to be significant are discussed further in sections 5.6.1 to 5.6.3.

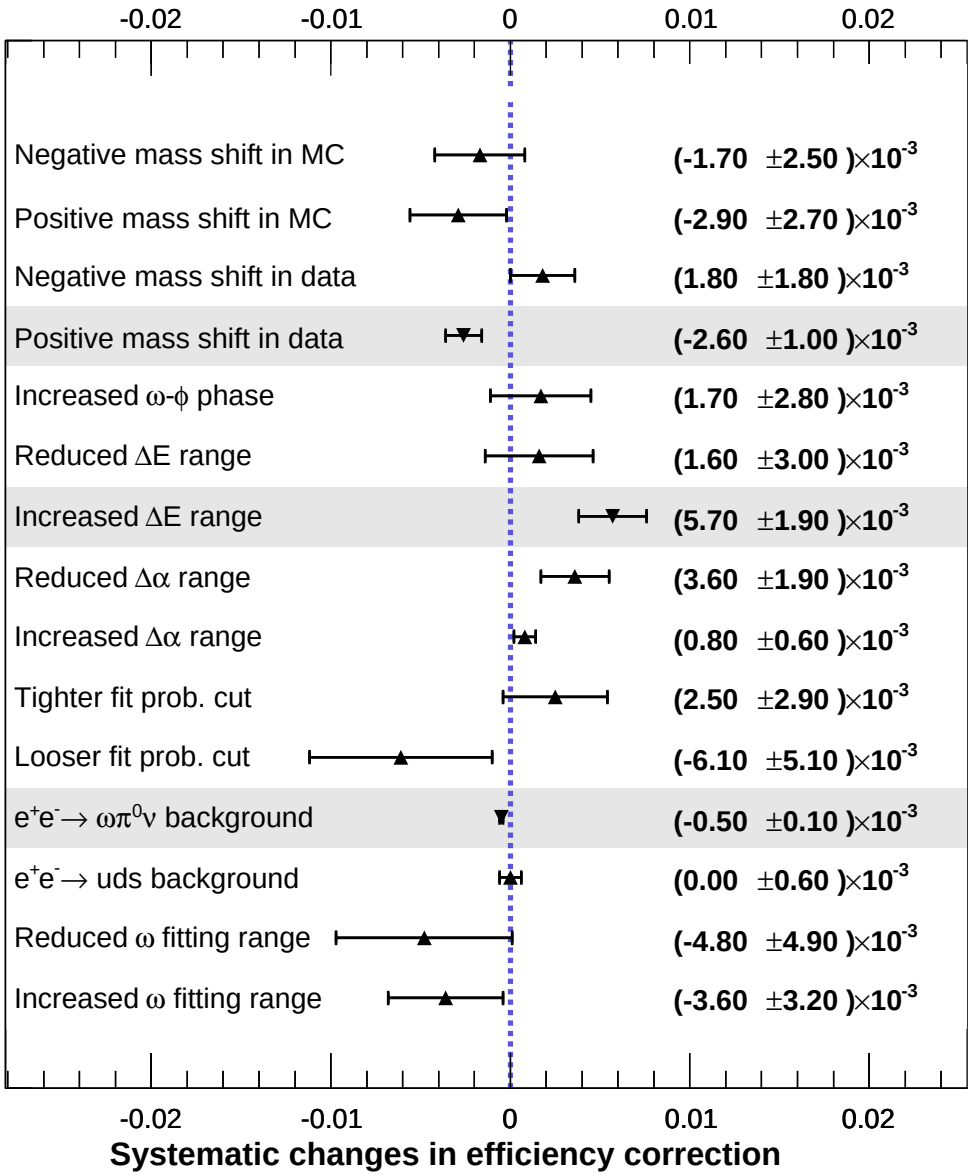

Figure 5.14: Systematic changes, D, for each systematic check. The shaded variables are the significant sources of systematic uncertainty (where D is more than 2 standard deviations away from zero) which make up the overall systematic uncertainty of 0.63%

5.6.1 The mass shift in data

The difference in peak mass between the reconstructed and generated $\pi^+\pi^-\pi^0$ mass spectra is called the 'mass shift', as introduced in section 5.4.3. There is no mass shift in the data so mass shifts of -1.0 MeV and 1.0 MeV are introduced in turn. These are the largest mass shifts which can be applied to the data before the χ^2 values of the fit become substantially larger. Introducing a mass shift of 1.0 MeV results in a 0.26% variation in the efficiency correction, which is included in the overall systematic uncertainty.

5.6.2 ΔE for the matching region

The matching region (as defined in section 5.4.1) is partly defined in terms of ΔE, the difference in energy between an inferred and a detected π^0. The chosen range of ΔE is ± 0.6 GeV, which is reduced to ± 0.4 GeV and increased to ± 0.8 GeV, always keeping the range the same for data and MC. If the range is reduced or increased any further, the χ^2 values of the fit become substantially larger. Increasing ΔE results in a 0.57% variation in the efficiency correction, which is included in the overall systematic uncertainty.

5.6.3 Background channels

It is possible that ω resonances in background channels may contribute at a small level to the selected event samples, and this would affect the efficiency determination if the matched π^0 is not the one from the ω decay. However, such events would be most unlikely to pass the kinematic fit and to have a match between the inferred π^0 and a detected one.

In order to check for this, a sample of 1.3×10^6 $\pi^+\pi^-\pi^0\pi^0\gamma$ events and a sample of 7.4×10^6 (313×10^6 before the *IsrLooseGamma* skim) $e^+e^- \to uds$ events are simulated. Figures 5.15 and 5.16 show the raw $\pi^+\pi^-\pi^0$ spectra for $\pi^+\pi^-\pi^0\pi^0\gamma$ events and uds events respectively, before any cuts are made, showing, as expected, significant ω production in both. Figures 5.17 and 5.18 show the $\pi^+\pi^-\pi^0$ spectra once the event selections and kinematic fits have been made and the events have been divided into seen and unseen samples. The ω peaks are very much reduced after the event selections.

To quantify the systematic effect, each sample is added to the 133 fb^{-1} Run 5 signal MC sample and the efficiency correction factor is re-evaluated. With a

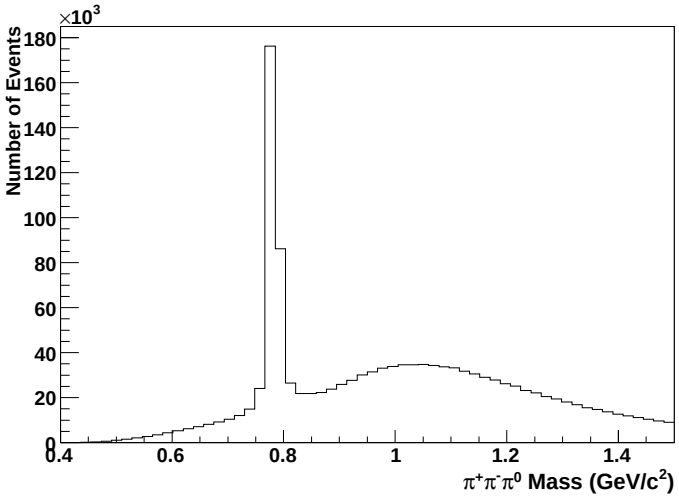

Figure 5.15: The $\pi^+\pi^-\pi^0$ mass spectra for Run 5 $e^+e^- \to \pi^+\pi^-\pi^0\pi^0\gamma$ MC events. This shows events with a π^0 energy between 0.0 and 2.0 GeV.

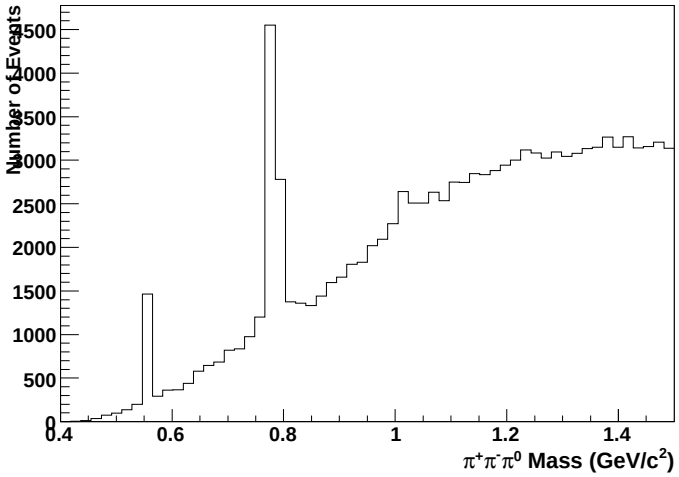

Figure 5.16: The $\pi^+\pi^-\pi^0$ mass spectra for Run 5 $e^+e^- \to uds$ MC events which have passed the *IsrLooseGamma* skim. This shows events with a π^0 energy between 0.0 and 2.0 GeV.

cross section of 3.9 pb [63] the $\pi^+\pi^-\pi^0\pi^0\gamma$ sample has an effective integrated luminosity of 330 fb^{-1} while the *uds* sample has a cross section of 2.1 nb [37] and an integrated luminosity of 150 fb^{-1}. Adding the $e^+e^- \to \omega\pi^0\gamma$ background mode results in a 0.05% variation in the efficiency correction, which is included in the overall systematic uncertainty.

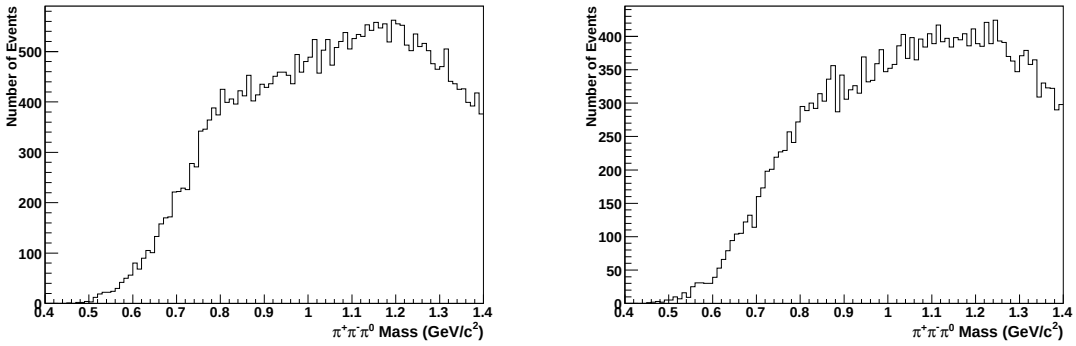

(a) (b)

Figure 5.17: The $\pi^+\pi^-\pi^0$ mass spectra for Run 5 $e^+e^- \to \pi^+\pi^-\pi^0\pi^0\gamma$ MC events selected as (a) seen or (b) unseen samples. These show events with a π^0 energy between 0.0 and 2.0 GeV.

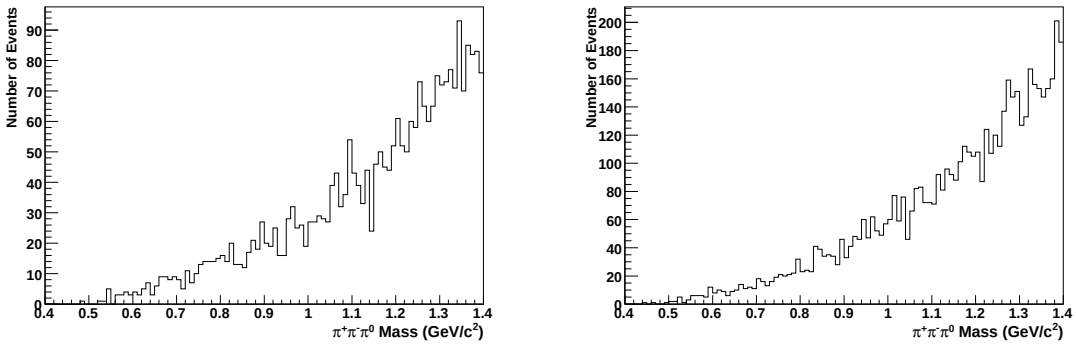

(a) (b)

Figure 5.18: The $\pi^+\pi^-\pi^0$ mass spectra for Run 5 $e^+e^- \to uds$ MC events selected as (a) seen or (b) unseen samples. These show events with a π^0 energy between 0.0 and 2.0 GeV.

5.7 Summary

The ratio of π^0 detection efficiency in data relative to MC has been measured for *BABAR* by counting entries in the ω resonance region of ISR events $e^+e^- \to \gamma\pi^+\pi^-\pi^0$. The efficiency correction factor for the *pi0Loose* candidate list is found to be independent of Run and of π^0 energy, with an overall value of $1.002 \pm 0.006(\text{stat}) \pm 0.006(\text{syst})$. This indicates that the MC produces a reliable simulation of the π^0 efficiency for the *pi0Loose* candidate list. The statistical error has been scaled to take into account the possibility of a small π^0 energy dependence, although evidence for such a dependence is inconclusive. The combined statistical and systematic error on the overall efficiency correction factor is thus 0.85%.

This study is one of several being done at *BABAR*, each within a different physics environment: for example using $D_s^- \to D^0\pi^-$ decays with $D^0 \to K^-\pi^-(\pi^0)$; or $\tau^- \to h^-\nu_\tau$ decays where h^- is a π^- or ρ^- meson; or $e^+e^- \to \omega\pi^0\gamma$ decays with $\omega \to \pi^+\pi^-\pi^0$; or decays of K^{*0} and K^{*-} into combinations of π^0, π^-, K_S^0 and K^-. The results of all these studies will be used to decide on the final systematic uncertainty on the π^0 detection efficiency correction for *BABAR* measurements.

Chapter 6

Event selection

Chapter 4 described how data collected by the *BABAR* detector are processed into a data set ready for physics analysis. Chapter 7 will describe the measurement of the $\tau^- \to K^-\eta\nu_\tau$ and $\tau^- \to \pi^-\eta\nu_\tau$ branching fractions. To make these measurements, using the $\eta \to \pi^+\pi^-\pi^0$ decay mode. Therefore τ leptons which decay into the $(\pi^-/K^-)\pi^+\pi^-\pi^0\nu_\tau$ final state are required for the analysis. This chapter describes the selections which are used to produce a sample of these events.

The event selection process is done over several stages. Section 6.1 outlines what experimental and simulated data are used for this analysis and section 6.2 presents the strategy used to choose the selections. Section 6.3 explains the selection of events which may contain $\tau^- \to (\pi^-/K^-)\pi^+\pi^-\pi^0\nu_\tau$ decays and section 6.4 outlines the efficiency of these selections.

6.1 Data and Monte Carlo samples

This analysis uses $425.7\,\text{fb}^{-1}$ of on-peak collision data collected at the $\Upsilon(4S)$ resonance ($\sqrt{s} = 10.58$ GeV) and $44.4\,\text{fb}^{-1}$ of off-peak data collected at an energy ~ 40 MeV below the $\Upsilon(4S)$ resonance. The data were collected by the *BABAR* detector over Runs 1 to 6, as described in section 4.1.1.

The cross section for $e^+e^- \to \tau^+\tau^-$ is 0.919 ± 0.003 nb [21] at the $\Upsilon(4S)$ resonance, as determined using events simulated by the `KK2F` MC generator (introduced in section 4.3.1). Thus, the total number of $\tau^+\tau^-$ events produced is expected to be 4.32×10^8 events.

The MC samples of $e^+e^- \to \tau^+\tau^-$ events are generated using the `KK2F` generator with τ decays simulated by the `TAUOLA` package (also introduced in

Dedicated sample	Number of events ($\times 10^6$)
$\tau^- \to \pi^- \eta \nu_\tau$	1.650
$\tau^- \to \pi^- \eta \pi^0 \nu_\tau$	1.654
$\tau^- \to \pi^- \eta \overline{K^0} \nu_\tau$	1.654
$\tau^- \to K^- \eta \nu_\tau$	3.548
$\tau^- \to K^- \eta \pi^0 \nu_\tau$	1.678

Table 6.1: The number of events generated in the dedicated MC samples.

Sample	Number of events ($\times 10^8$)	Cross section (nb)	Effective integrated luminosity (fb^{-1})
$\tau^+ \tau^-$	3.6765	0.919	400
$u\overline{u}$,$d\overline{d}$,$s\overline{s}$	8.4153	1.39, 0.35, 0.35	403
$c\overline{c}$	10.8328	1.30	833
B^0 $\overline{B}^0$	6.6479	0.535	1243
B^+ B^-	6.7822	0.535	1268

Table 6.2: The number of events generated in the background MC samples, with the cross sections and effective integrated luminosities at $\sqrt{s} = 10.58$ GeV [21, 37].

section 4.3.1). This is called the 'generic τ-decay sample' and has a $\tau^- \to \pi^-\pi^+\pi^-\pi^0\nu_\tau$ branching fraction of 4.365%, which includes decays via ρ and ω resonances. The only τ decay mode included in the generic τ-decay sample which contains an η meson is $\tau^- \to \pi^- \eta \pi^0 \nu_\tau$.

Other τ decay modes containing η mesons are not included in the generic τ-decay sample so dedicated MC $e^+e^- \to \tau^+\tau^-$ samples of events in which the τ leptons decay through $\tau^- \to \pi^- \eta \nu_\tau$, $\tau^- \to \pi^- \eta \pi^0 \nu_\tau$, $\tau^- \to \pi^- \eta \overline{K^0} \nu_\tau$, $\tau^- \to K^- \eta \nu_\tau$ and $\tau^- \to K^- \eta \pi^0 \nu_\tau$ are produced using `KK2F` and `TAUOLA`. In each event, one τ decays via the signal mode, while the other τ is decayed generically. The η meson always decays generically, with an $\eta \to \pi^+\pi^-\pi^0$ branching fraction of 23.2%. The details of these dedicated samples are given in table 6.1.

Non-τ MC samples of e^+e^- collisions producing $u\overline{u}$, $d\overline{d}$, $s\overline{s}$ (collectively referred to as the *uds* sample), $c\overline{c}$, $B^0\overline{B}^0$ and B^+B^- are used to model the non-τ backgrounds. These samples are simulated using the `EvtGen` and `JetSet` generators, as described in section 4.3.1. The details of these MC samples, as well as the generic-τ sample, are given in table 6.2. All simulated events are processed through the full detector simulation and reconstruction software.

For reference, the branching fractions of relevant decay modes as given by the Particle Data Group [15] (PDG), a recent paper from the Belle Collaboration [16] and as set in TAUOLA are listed in table 6.3. In the following sections the differences between the branching fractions as set in TAUOLA and the measured (PDG) branching fractions are accounted for when required.

All simulated samples are generated with approximately the same proportion of events in each Run as in the data. For comparisons with data, the simulated samples for each Run are normalised to the data luminosity. The dedicated τ-decay modes are normalised to the data luminosity using the branching fractions measured by Belle and the $\tau^- \to K^-\eta\nu_\tau$ branching fraction measured in this analysis, as explained in chapter 7.

Mode	PDG BF [15]	Belle BF [16]	TAUOLA BF
$\pi^0 \to \gamma\gamma$	$(98.798 \pm 0.032) \times 10^{-2}$	-	98.8×10^{-2}
$\eta \to \pi^+\pi^-\pi^0$	$(22.7 \pm 0.4) \times 10^{-2}$	-	23.2×10^{-2}
$\tau^- \to \pi^-\eta\pi^0\nu_\tau$	$(1.39 \pm 0.10) \times 10^{-3}$	$(1.35 \pm 0.08) \times 10^{-3}$	1.8×10^{-3}
$\tau^- \to K^-\eta\nu_\tau$	$(1.61 \pm 0.11) \times 10^{-4}$	$(1.58 \pm 0.10) \times 10^{-4}$	-
$\tau^- \to \pi^-\eta\overline{K^0}\nu_\tau$	$(9.3 \pm 1.5) \times 10^{-5}$	$(8.8 \pm 1.5) \times 10^{-5}$	-
$\tau^- \to K^-\eta\pi^0\nu_\tau$	$(4.8 \pm 1.2) \times 10^{-5}$	$(4.6 \pm 1.2) \times 10^{-5}$	-

Table 6.3: The branching fractions (BF) used in this analysis, as given by the Particle Data Group (PDG), a recent Belle paper [16] and as set in TAUOLA. The PDG branching fractions are averages of previous measurements, which include the Belle branching fractions.

6.2 Selection strategy

Events are selected according to various selection variables so that relatively more events from the background modes are rejected, compared to the signal mode. In this way the overall proportion of signal events is increased.

To provide the information on potential selection variables, distributions of selection variables are plotted for events which have had all other selections applied. These are called '$N-1$' distributions and a selection of some important ones are shown in appendix A. The $N-1$ distributions are made for the signal and background modes so that the selections which will best reduce the relative proportion of the background modes can be determined by eye. The $N-1$ plots ensure that selections are not applied to a variable if the rejected events are al-

ready rejected by selections made on another variable, allowing the number of selections to be kept to a minimum.

In addition, selections must only be made on a variable if the values of the variable for the rejected events lie in a region of the $N-1$ distribution where the data and MC distributions agree well. This results in signal efficiencies and background rejection rates which are well understood.

6.3 Selecting $\tau^- \to (\pi^-/K^-)\pi^+\pi^-\pi^0\nu_\tau$ candidates

6.3.1 Preselection

The preselection process aims to select $e^+e^- \to \tau^+\tau^-$ events with the desired topology, that is, the desired multiplicity and distribution of tracks. To achieve this, the `Tau1N` skim, which is described in section 4.5, is used to make initial selections on the data and MC samples. The `Tau1N` skim divides the events into two hemispheres which are separated by the plane normal to the thrust axis in the CM frame.

The `Tau1N` skim selections are further refined using a package which is called `TauTo4PiUser`. This uses the `SimpleComposition` application (described in section 4.2.4) to select events with overall charge neutrality and exactly four tracks in the *goodTracksVeryLoose* list (defined in section 4.2.1). One hemisphere, called the 'tag' side, is required to have exactly one track while the other hemisphere, called the 'signal' side, is required to have exactly three tracks. At least one π^0 from the *pi0LooseMass* list, as defined in section 4.2.4, is required on the signal side. The preselection process also constructs variables which are used for further selections. After the preselection, the reconstructed events are saved in large `ntuples` (a type of list which is convenient for event storage).

6.3.2 Photon conversions

Events where two of the signal side tracks come from photon conversions can be rejected using the effective mass squared, m^2_{ee}. The electron mass hypothesis is applied to the three signal side charged tracks and the invariant mass of the two possible 'e^+e^-' pairs are calculated; the smallest of the two is called m^2_{ee}. However, the $N-1$ distributions for m^2_{ee} show that selecting events according to their value of m^2_{ee} would remove approximately equal proportions of signal

and background events. Therefore, this is not an effective cut variable and no selections are applied to it. This means that Bhabha events with a converted photon can pass the selections, but since they do not contain any η mesons they will only contribute to the continuum background in the $\pi^+\pi^-\pi^0$ mass spectrum.

6.3.3 Event level selections

Three event level variables are useful for the selection of $e^+e^- \to \tau^+\tau^-$ events and the values of the selections are summarised in table 6.4.

Cut Variable	Selection Value
$E_{total}(GeV)$	$< 0.8E_{initial}$
Thrust	> 0.95
$cos\theta_{thrust}$	< 0.8

Table 6.4: Event level selections used for the τ analysis. The variables are described in the text.

The variable E_{total} is the total measured energy of an event in the lab frame. Since $\tau^+\tau^-$ events have missing energy carried by ν_τ, E_{total} will be less than the initial-state energy, $E_{initial}$ (12.1 GeV). The $N-1$ distributions for $E_{total}/E_{initial}$ are shown in figures A.2 and A.3 in appendix A. Events are required to have E_{total} below 80% of $E_{initial}$ in order to reduce the proportion of the $q\overline{q}$ background, especially uds, when compared to the signal modes. This selection also rejects some of the Bhabha events with converted photons.

The thrust axis is calculated using the *calorClusterNeutral* and *chargedTracks* candidates for the event, as described in section 4.5.2. The $\tau^+\tau^-$ events are highly collinear and therefore have a large thrust magnitude, as shown by the $N-1$ distributions for the thrust magnitude in figures A.4 and A.5. Selections made on the thrust magnitude help discriminate against the $q\overline{q}$ background, especially the $c\overline{c}$ events.

The angle θ_{thrust} is defined as the angle between the thrust axis and the beam axis. Rejecting events with a large value of $cos\theta_{thrust}$ does not discriminate against any background, but it does ensure that the selected events are well reconstructed, removing those that pass through the edge of the active detector region near the beam pipe.

6.3.4 Tagging

The τ leptons decay before entering the active detector volume so their existence must be inferred from the detection of their decay products. The $e^+e^- \to \tau^+\tau^-$ events are divided into two hemispheres so that there is one τ candidate in each hemisphere (as explained in section 4.5.2). Therefore, if it can be shown that there is a τ lepton in one hemisphere, it follows that there must be a τ lepton in the other hemisphere as well. This process of deduction is called 'tagging'; the single track in the tag side is identified as a τ decay product so that the existence of a τ on the signal side can be inferred.

The most common τ decay modes which contain only a single track are $\tau \to e^-\bar{\nu}_e\nu_\tau$, $\tau \to \mu^-\bar{\nu}_\mu\nu_\tau$, $\tau \to \pi^-\nu_\tau$ and $\tau \to \pi^-\pi^0\nu_\tau$ which have branching fractions of $17.84\pm0.05\%$, $17.36\pm0.05\%$, $10.91\pm0.07\%$ and $25.51\pm0.09\%$ [15] respectively. Therefore, tagging requires that the single track in the tag hemisphere is identified as either an electron, muon or pion.

To identify the particle type of the track, the PID selectors defined in section 4.2.3 are used. Three samples of events are created; for each sample the tag track is required to pass the selector for either the electron, muon or pion. The three tag samples of events are defined as:

- e-tag events require that the tag track passes *PidLHElectron*.
- μ-tag events require that the tag track passes *muNNTight*.
- π-tag events require that the tag track passes *piLHTight*.

The e-tag and μ-tag samples are the cleanest samples and are therefore used for the branching fraction measurements, as well as the $c\bar{c}$ background studies (described in chapter 7). The π-tag events have a higher level of *uds* backgrounds included and are therefore only used for the *uds* background studies, as described in section 7.2.1.

Each tag track is weighted to correct for differences in the PID selection efficiencies between the data and simulations, as described in section 4.4. A systematic uncertainty on this correction is applied to the final measurements.

6.3.5 Photon and π^0 selections

The signal-side τ is selected to decay via the signal $\tau^- \to (\pi^-/K^-)\pi^+\pi^-\pi^0\nu_\tau$ mode. Therefore a single π^0 candidate is required on the signal side, as well as

the three tracks already required.

The number of π^0 candidates in the event which meet the following criteria are counted:

- π^0 candidate is included in the *pi0LooseMass* list (defined in section 4.2.4).
- π^0 candidate has a mass within 0.015 GeV of the known π^0 mass [15].
- π^0 candidate and both daughter photons are in the signal-side hemisphere.

A selection is made which requires that events contain exactly one such π^0 candidate.

Various properties of the photons (*goodPhotonLoose* candidates) within the event are examined as possible cut variables. The $N-1$ distributions for the distance of closest approach between the signal-side photons and the nearest charged track are similar for background and signal modes, so no selections are made on this quantity. These distributions also show that photons caused by split-offs (when a charged particle interaction produces a photon) are well simulated by the MC.

The $N-1$ distributions of the energy of the two daughter photons from the π^0 candidate are also considered. Only photons with an energy above 30 MeV are included in the *goodPhotonLoose* list and no further selections on the energy of these photons are required.

The signal-side photons that are not daughters of the π^0 candidate are more useful for rejecting backgrounds. The number that have an energy above 100 MeV are counted for each event, as shown by the $N-1$ distribution in figures A.6 and A.7 in appendix A. Events are required to have no such photons; this is effectively the same as requiring that the energy of signal-side photons which are not the daughters of the π^0 candidate is between 30 MeV and 100 MeV. This is the only selection that significantly reduces the proportion of $\tau^- \to \pi^-\eta\pi^0\nu_\tau$ decays, which is useful because the $\tau^- \to \pi^-\eta\pi^0\nu_\tau$ mode contributes more background events to the $\tau^- \to \pi^-\eta\nu_\tau$ analysis in the next chapter than any other.

6.3.6 The $\pi^+\pi^-\pi^0$ mass spectra

The previous sections describe how events with three tracks and a π^0 in the signal hemisphere are selected. This section describes the final requirements which select signal $\tau^- \to (\pi^-/K^-)\pi^+\pi^-\pi^0\nu_\tau$ candidates.

Initially, all three signal-side tracks are assumed to be pions, but they have not been required to pass any PID selectors (described in section 4.2.3). Each event therefore has two possible $\pi^+\pi^-\pi^0$ combinations. The remaining track associated with each $\pi^+\pi^-\pi^0$ combination is called the 'bachelor' track.

If the bachelor track passes the *piLHTight* PID selector it is identified as a pion, while if it passes the *KLHTight* PID selector it is identified as a kaon.

Each bachelor track is weighted to correct for differences in the PID selection efficiencies between the data and simulation, as described in section 4.4. The systematic uncertainty on this correction is applied to the final measurements. In order to minimise the systematic uncertainty resulting from the PID selectors, no PID requirements are applied to the tracks used for the $\pi^+\pi^-\pi^0$ combination.

To select $\tau^- \to \pi^-\pi^+\pi^-\pi^0\nu_\tau$ candidates the bachelor track is required to be identified as a pion and the $\pi^\pm\pi^+\pi^-\pi^0$ mass is required to be less than the τ mass. To count the number of η mesons in the sample the $\pi^+\pi^-\pi^0$ mass spectrum is fitted to obtain the intensity of the peak within the η region, as described in chapter 7. When the $\pi^+\pi^-\pi^0$ mass spectrum is formed, both possible $\pi^+\pi^-\pi^0$ combinations are included as entries if the corresponding bachelor is a pion. Figure 6.1 shows the invariant $\pi^+\pi^-\pi^0$ mass spectrum for the dedicated $\tau^- \to \pi^-\eta\nu_\tau$ MC sample once all selections have been applied and the bachelor has been required to be a pion.

Figure 6.2 shows the same invariant $\pi^+\pi^-\pi^0$ mass distribution for the total MC and data samples. This shows that the $\pi^+\pi^-\pi^0$ mass spectrum is dominated by the ω resonance, which has a mass of 782.65 ± 0.12 MeV/c^2 [15]. The simulation of the $\pi^\pm\pi^+\pi^-\pi^0$ mass spectrum for the $\tau^- \to \pi^-\omega\nu_\tau$ decay mode is not correct in `TAUOLA`; however this does not affect the analysis presented here.

Figure 6.3 is made using events in the MC samples where at least one of the two possible bachelors is identified as a pion. It shows the $\pi^\pm\pi^+\pi^-\pi^0$ mass distributions, for events where the mass of at least one $\pi^+\pi^-\pi^0$ combination lies between 0.52 GeV and 0.57 GeV (the η window).

In the following sections the 'sideband subtraction' method is used to make $\eta\pi^-$ mass distributions for illustrative purposes. The bachelor is required to be a pion and the corresponding $\pi^+\pi^-\pi^0$ combination is classified as part of the 'η peak' if the invariant 3π mass is between 0.530 GeV/c^2 and 0.560 GeV/c^2. It is classified as part of the 'η sideband' if the invariant 3π mass is between 0.505 GeV/c^2 and 0.520 GeV/c^2 or between 0.570 GeV/c^2 and 0.585 GeV/c^2.

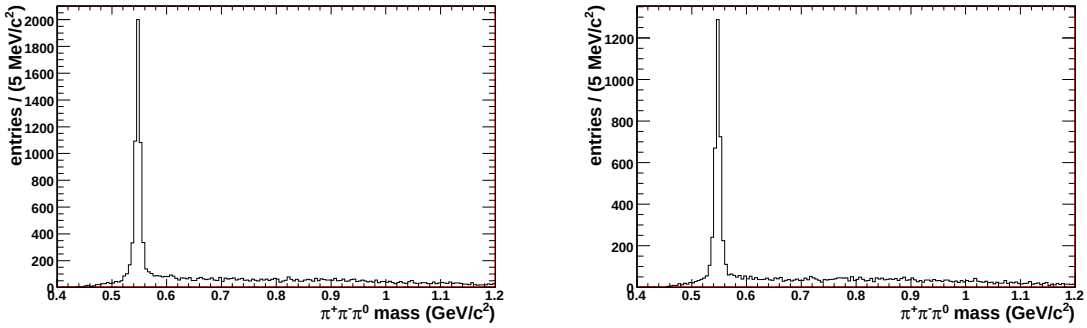

(a) e-tag events (b) μ-tag events

Figure 6.1: The $\pi^+\pi^-\pi^0$ mass distribution for the $\tau^- \to \pi^-\eta\nu_\tau$ signal MC sample, when the corresponding bachelor is identified as a pion. There are up to two possible entries per event, one for each possible $\pi^+\pi^-\pi^0$ combination. The peak is made up of the $\pi^+\pi^-\pi^0$ combinations which genuinely decayed through an η meson while the continuum background is made of entries from the other combinations. The number of $\eta \to \pi^+\pi^-\pi^0$ decays can be found by fitting the spectrum.

The $\pi^\pm\pi^+\pi^-\pi^0$ mass spectrum made up of all the η sideband entries is subtracted from the $\pi^\pm\pi^+\pi^-\pi^0$ mass spectrum made up of all the η peak entries, resulting in the $\eta\pi^-$ mass spectrum.

To select $\tau^- \to K^-\pi^+\pi^-\pi^0\nu_\tau$ candidates the bachelor track is required to be identified as a kaon and the $K^-\pi^+\pi^-\pi^0$ mass is required to be less than the τ mass.

To count the number of η mesons in the sample the $\pi^+\pi^-\pi^0$ mass spectrum is fitted to obtain the intensity of the peak within the η region, as described in chapter 7. When the $\pi^+\pi^-\pi^0$ mass spectrum is formed, both possible $\pi^+\pi^-\pi^0$ combinations are included as entries if the corresponding bachelor is a kaon. Figure 6.4 shows the invariant $\pi^+\pi^-\pi^0$ mass spectrum for the dedicated $\tau^- \to K^-\eta\nu_\tau$ MC sample once all selections have been applied and the bachelor is required to be a kaon. Figure 6.5 shows the same invariant $\pi^+\pi^-\pi^0$ mass distribution for the total MC and data samples. The e-tagged events clearly have higher background from Bhabha events.

In the following sections the 'sideband subtraction' method is used to make ηK^- mass distributions for illustrative purposes. The bachelor is required to be a kaon and the corresponding $\pi^+\pi^-\pi^0$ combination is classified as part of the

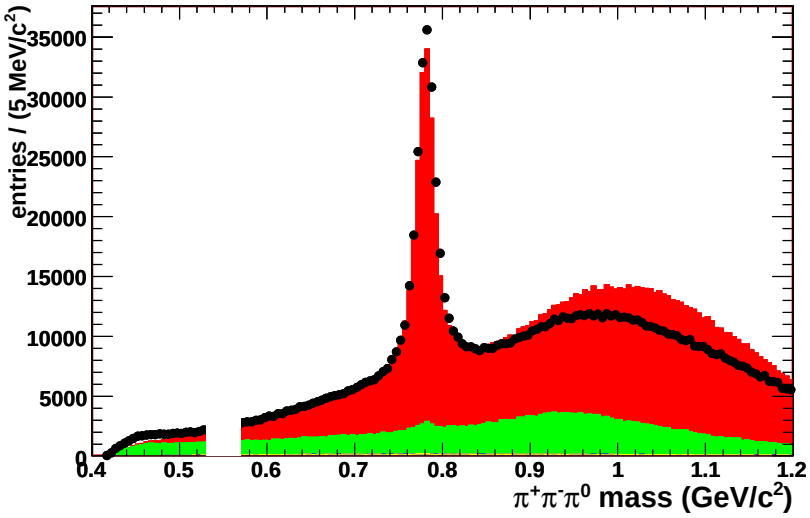

(a) e-tag events

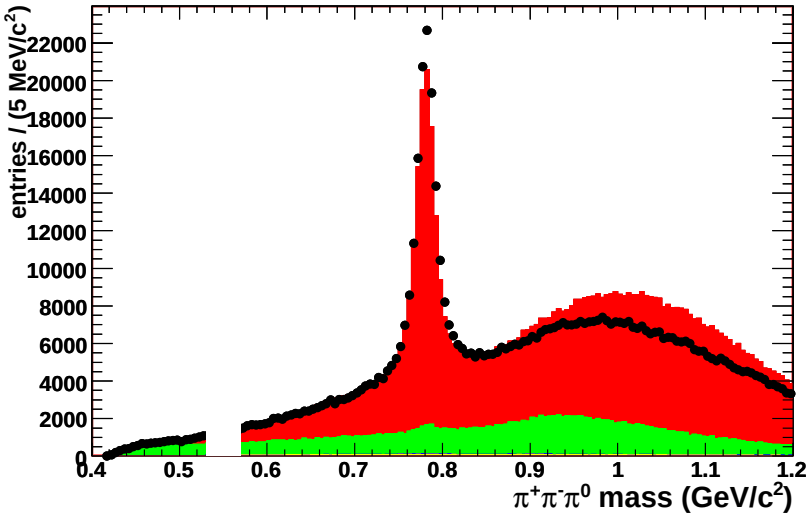

(b) μ-tag events

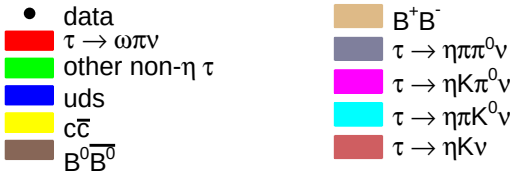

Figure 6.2: The $\pi^+\pi^-\pi^0$ mass distribution for the MC and data events, when the corresponding bachelor is identified as a pion. There are up to two possible entries per event. The region around the η peak has been hidden because the $\tau^- \to \pi^-\eta\nu_\tau$ analysis is performed blind. The MC samples are normalised to the data luminosity.

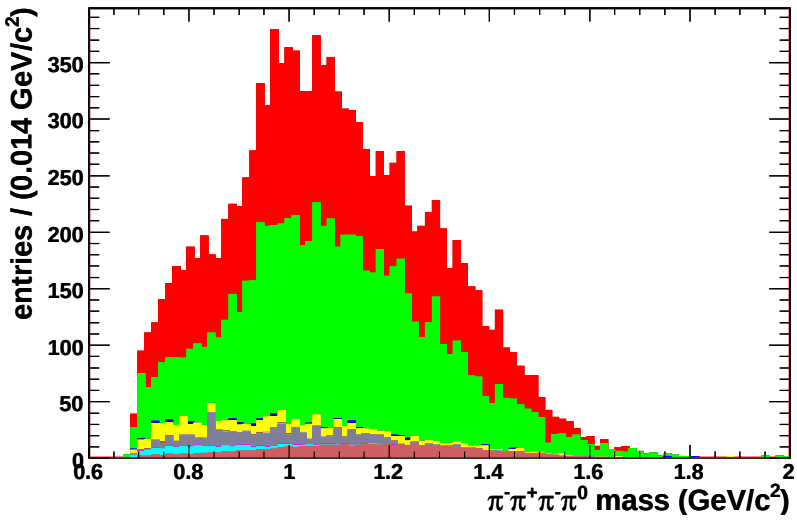

(a) e-tag events

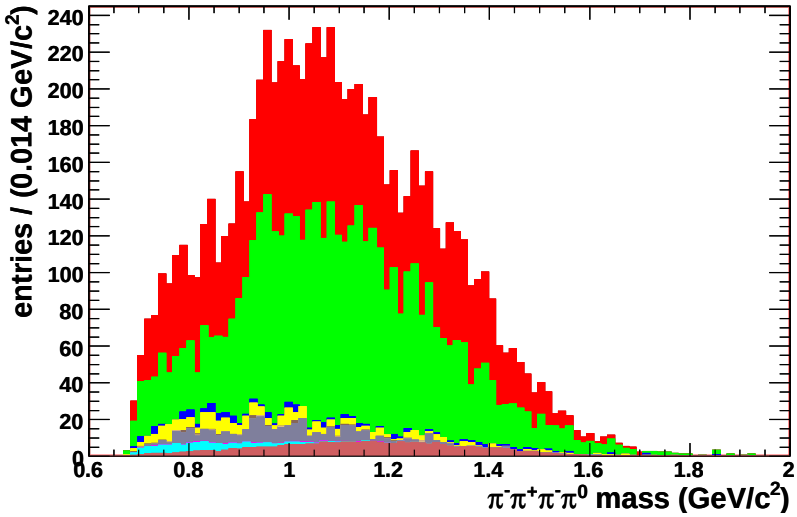

(b) μ-tag events

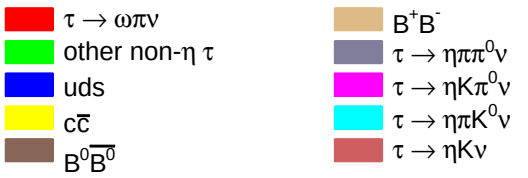

Figure 6.3: The $\pi^\pm\pi^+\pi^-\pi^0$ mass distribution for MC events when at least one of the two possible bachelors is identified as a pion and the mass of at least one possible $\pi^+\pi^-\pi^0$ combination lies between 0.52 GeV and 0.57 GeV. There is one possible entry per event. The MC samples are normalised to the data luminosity.

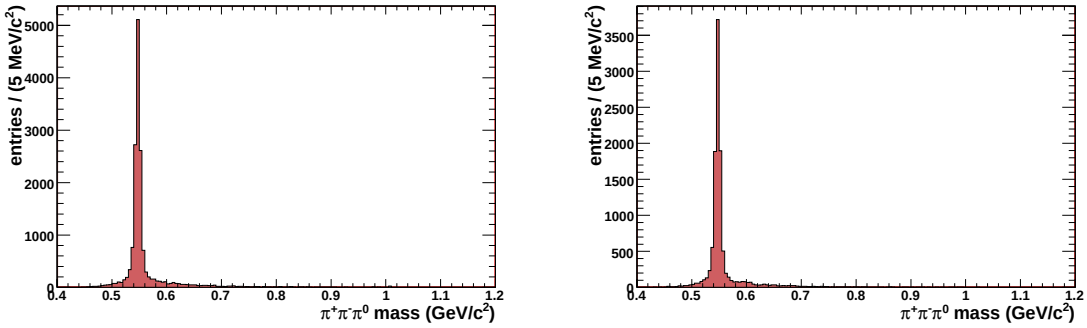

(a) e-tag events (b) μ-tag events

Figure 6.4: The $\pi^+\pi^-\pi^0$ mass distribution for the $\tau^- \to K^-\eta\nu_\tau$ signal MC sample, when the corresponding bachelor is identified as a kaon. There are up to two possible entries per event, one for each possible $\pi^+\pi^-\pi^0$ combination. The peak is made up of $\pi^+\pi^-\pi^0$ combinations which genuinely decayed through an η meson while the continuum background is made of entries from the other combinations. The number of $\eta \to \pi^+\pi^-\pi^0$ decays can be found by fitting the spectrum.

'η peak' if the invariant 3π mass is between 0.530 GeV/c^2 and 0.560 GeV/c^2. It is classified as part of the 'η sideband' if the invariant 3π mass is between 0.505 GeV/c^2 and 0.520 GeV/c^2 or between 0.570 GeV/c^2 and 0.585 GeV/c^2. The $K^-\pi^+\pi^-\pi^0$ mass spectrum made up of all the η sideband entries is subtracted from the $K^-\pi^+\pi^-\pi^0$ mass spectrum made up of all the η peak entries, resulting in the ηK^- mass spectrum. Figure 6.6 shows the ηK^- mass distribution in data and MC samples, obtained using the sideband subtraction method.

6.4 The selection efficiency

The numbers of events which pass each of the selections described above, given as a percentage of the total events, are shown in table 6.5 for the data and generic MC samples and in table 6.6 for the dedicated MC samples. Note that the final row in the table lists the percentage of events within the $\pi^+\pi^-\pi^0$ fitting range, which is not applied as a selection.

The $\eta\pi^-$ mass dependence of the selection efficiency is also studied. The `TAUOLA` package is used to generate the $\eta\pi^-$ mass spectrum for the $\tau^- \to \pi^-\eta\nu_\tau$ MC, before any selections are made. The reconstructed $\eta\pi^-$ mass spectrum for the signal $\tau^- \to \pi^-\eta\nu_\tau$ MC events is made using the sideband subtraction method after all the above selections have been applied. Taking the ratio of the

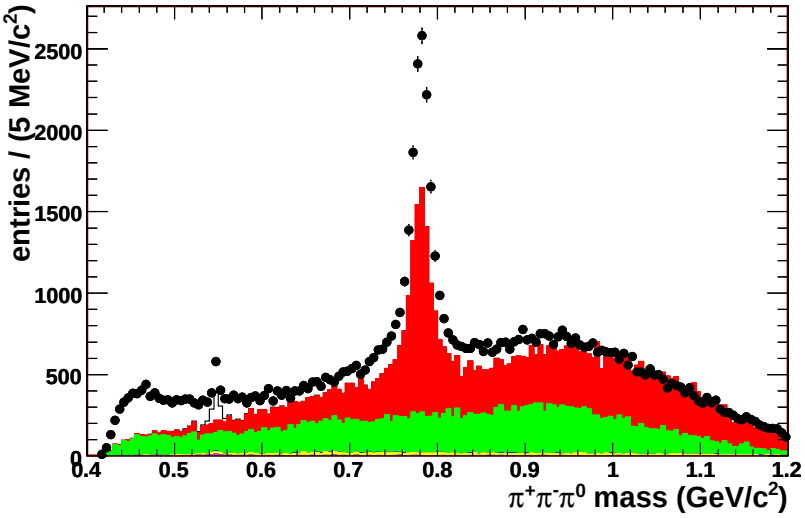

(a) e-tag events

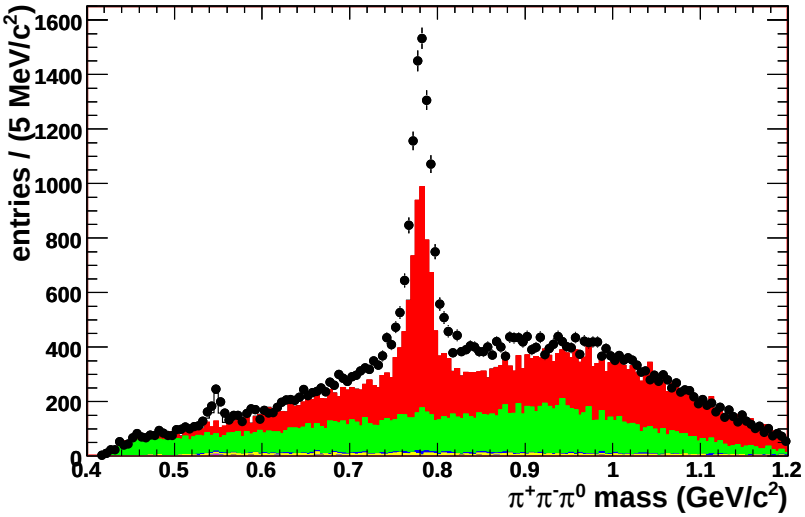

(b) μ-tag events

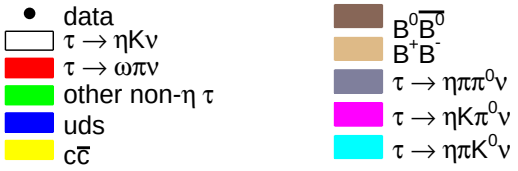

Figure 6.5: The $\pi^+\pi^-\pi^0$ mass distribution for the MC and data events, when the corresponding bachelor is identified as a kaon. There are up to two possible entries per event. The MC samples are normalised to the data luminosity; in particular the $\tau^- \to K^-\eta\nu_\tau$ sample is normalised to luminosity using the branching fraction reported in the following chapter in equation 7.4.

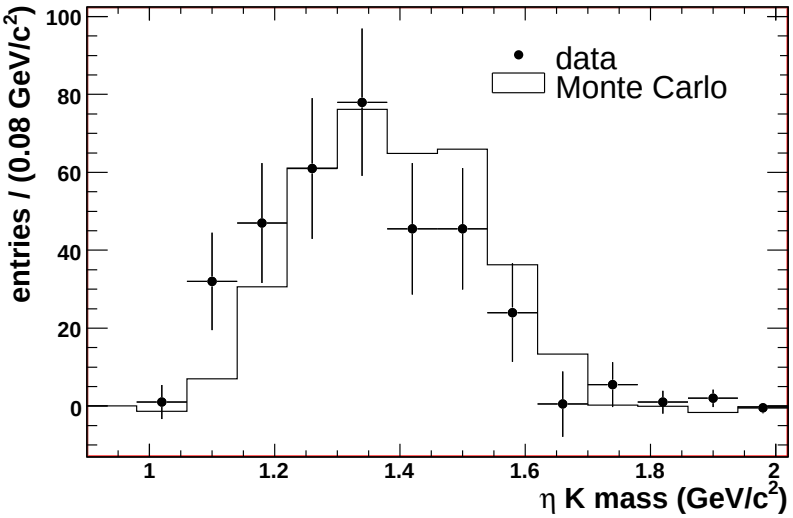

(a) e-tag events

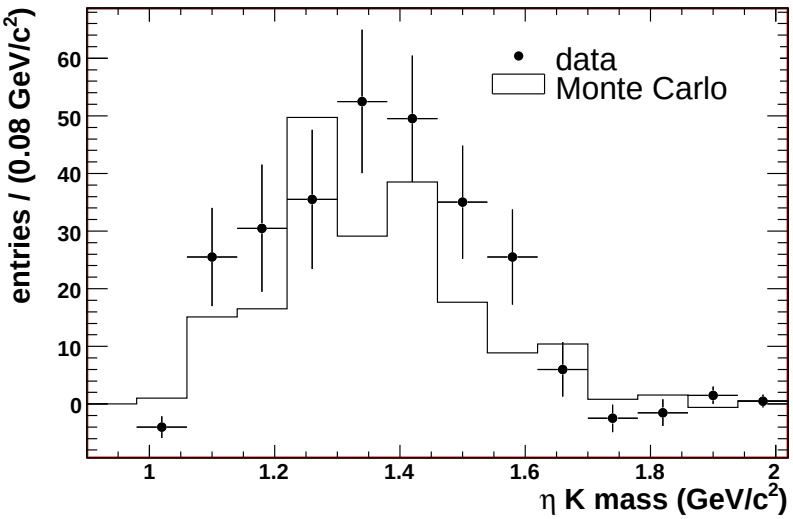

(b) μ-tag events

Figure 6.6: The ηK^- mass distribution for the data and MC samples, obtained using the sideband subtraction method. The MC samples are normalised to the data luminosity; in particular the $\tau^- \to K^- \eta \nu_\tau$ sample is normalised to luminosity using the branching fraction reported in the following chapter in equation 7.4.

Selection	Data	MC				
	on- & off-peak	τ	$c\overline{c}$	uds	$B^0\bar{B}^0$	B^+B^-
All events	100%	100%	100%	100%	100%	100%
`Tau1N` skim	3.87%	15.04%	7.58%	7.69%	2.03%	1.89%
Preselection	0.98%	4.72%	2.09%	2.36%	0.33%	0.36%
π^0 requirement	0.35%	2.44%	0.52%	0.74%	0.075%	0.077%
E_{total} selection	0.26%	1.99%	0.38%	0.38%	0.072%	0.072%
Thrust selections	0.074%	1.11%	0.035%	0.040%	0.0023%	0.0021%
Lepton tag	0.024%	0.42%	0.0072%	7.0×10^{-4}%	7.0×10^{-4}%	5.6×10^{-4}%
Photon requirement	0.017%	0.31%	0.0028%	3.2×10^{-4}%	2.4×10^{-4}%	1.7×10^{-4}%
(e-tag events only)	(0.011%)	(0.18%)	(0.0017%)	(0.77×10^{-4}%)	(1.4×10^{-4}%)	(1.0×10^{-4}%)
(μ-tag events only)	(0.0063%)	(0.13%)	(0.0011%)	(2.4×10^{-4}%)	(0.94×10^{-4}%)	(0.68×10^{-4}%)
4π mass $< \tau$ mass	0.017%	0.30%	0.0024%	2.7×10^{-4}%	2.2×10^{-4}%	1.5×10^{-4}%
Within 3π fit range	0.0016%	0.025%	4.2×10^{-4}%	3.9×10^{-5}%	5.5×10^{-5}%	3.0×10^{-5}%

Table 6.5: The percentage of original events which pass each selection, for the generic MC and data samples. Due to a problem with the Run 6 simulation of muons, the selection efficiency for Run 6 muons is set to zero. The fit range for the $\pi^+\pi^-\pi^0$ mass spectrum is defined as being between 0.49 GeV/c^2 and 0.62 GeV/c^2.

Selection	Dedicated MC samples				
	$\tau^- \to K^-\eta\nu_\tau$	$\tau^- \to \pi^-\eta\nu_\tau$	$\tau^- \to \pi^-\eta\pi^0\nu_\tau$	$\tau^- \to \pi^-\eta\overline{K^0}\nu_\tau$	$\tau^- \to K^-\eta\pi^0\nu_\tau$
All events	100%	100%	100%	100%	100%
`Tau1N` skim	21.6%	21.1%	21.8%	22.4%	21.8%
Preselection	10.8%	10.5%	14.1%	11.5%	14.1%
π^0 requirement	5.97%	5.78%	4.35%	4.36%	4.22%
E_{total} selection	4.59%	4.77%	3.34%	3.68%	3.16%
Thrust selections	3.16%	2.75%	1.95%	2.41%	2.22%
Lepton tag	1.08%	0.87%	0.65%	0.72%	0.69%
Photon requirement	0.86%	0.69%	0.18%	0.41%	0.23%
(e-tag events only)	(0.49%)	(0.41%)	(0.11%)	(0.24%)	(0.14%)
(μ-tag events only)	(0.38%)	(0.29%)	(0.072%)	(0.17%)	(0.088%)
4π mass $< \tau$ mass	0.86%	0.69%	0.18%	0.41%	0.23%
Within 3π fit range	0.78%	0.64%	0.069%	0.36%	0.13%

Table 6.6: The percentage of original events which pass each selection, for the dedicated MC samples. Due to a problem with the Run 6 simulation of muons, the selection efficiency for Run 6 muons is set to zero. The fit range for the $\pi^+\pi^-\pi^0$ mass spectrum is defined as being between 0.49 GeV/c^2 and 0.62 GeV/c^2.

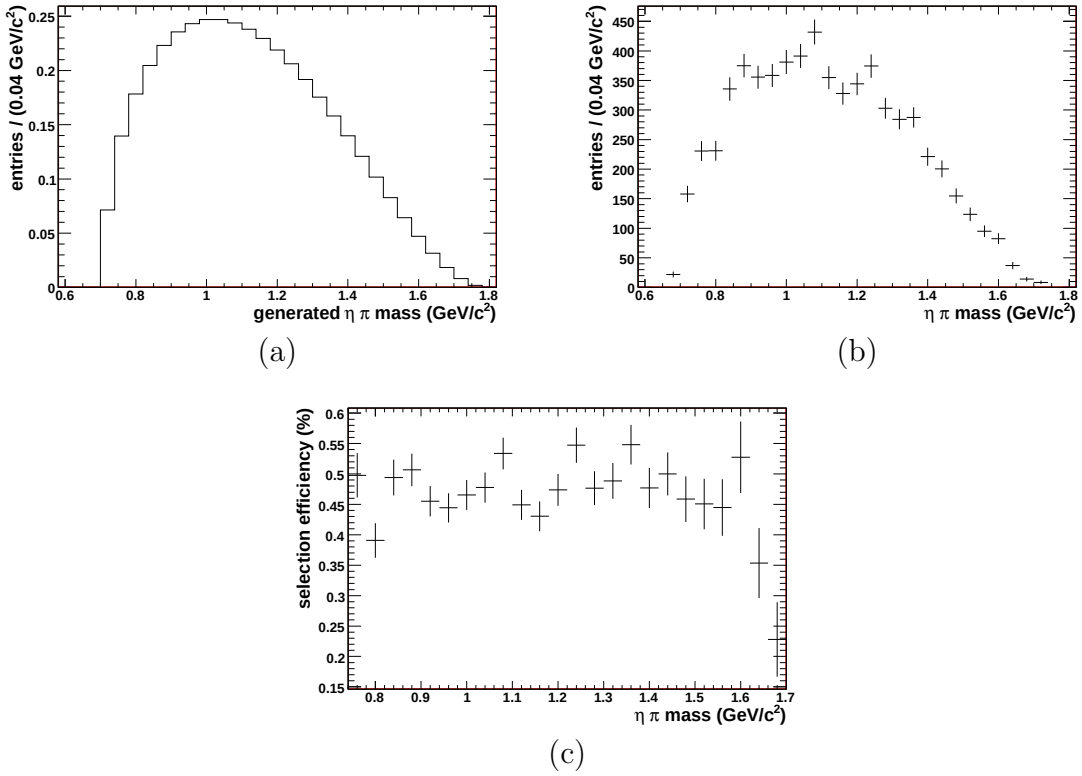

Figure 6.7: (a) The generated $\eta\pi^-$ mass spectrum for $\tau^- \to \pi^-\eta\nu_\tau$ MC and (b) the reconstructed $\eta\pi^-$ mass spectrum for $\tau^- \to \pi^-\eta\nu_\tau$ MC (made using the sideband subtraction method), are used to calculate (c) the selection efficiency as a function of $\eta\pi^-$ mass, for e-tagged and μ-tagged events.

reconstructed and generated distributions gives the relative selection efficiency as a function of $\eta\pi^-$ mass. In figure 6.7, this is scaled so that the weighted average selection efficiency across all $\eta\pi^-$ masses equals 0.47%, the selection efficiency found in section 7.4.2. There is seen to be no dependence of the selection efficiency on $\eta\pi^-$ mass, so the overall selection efficiency does not depend on the shape of the generated $\eta\pi^-$ mass spectrum.

Chapter 7

Branching fractions

The previous chapter describes how a sample of $\tau^- \to (\pi^-/K^-)\pi^+\pi^-\pi^0\nu_\tau$ candidates are selected. This chapter describes how these candidates are used to measure the $\tau^- \to K^-\eta\nu_\tau$ branching fraction and to search for $\tau^- \to \pi^-\eta\nu_\tau$ decays, using the $\eta \to \pi^+\pi^-\pi^0$ decay mode.

The branching fractions (BF) for $\tau^- \to K^-\eta\nu_\tau$ and $\tau^- \to \pi^-\eta\nu_\tau$ are calculated as

$$BF = \frac{N_{data} - N_{bkgd}}{\epsilon f N_{total}} \tag{7.1}$$

where N_{total} is the total number of τ decays in the data sample before any selections are made (864 million), N_{data} is the number of η mesons counted in the data sample after the selections are made (see sections 7.3.3 and 7.4.5), N_{bkgd} is the number of η mesons in the data sample which is expected to come from background modes, after the selections are made (see sections 7.3.1 and 7.4.1), ϵ is the signal efficiency (see sections 7.3.2 and 7.4.2), and f is a factor of 0.978 which corrects for the differences between branching fractions as set in `TAUOLA` and as measured by experiment (both of which are given in table 6.3), specifically for the $\eta \to \pi^+\pi^-\pi^0$ and $\pi^0 \to \gamma\gamma$ branching fractions. In the following sections, $N_{data} - N_{bkgd}$ is referred to as the 'observed signal'.

Section 7.1 explains how the number of η mesons in a sample is calculated by fitting the $\pi^+\pi^-\pi^0$ mass spectrum. Section 7.2 describes a study of the η production in simulated $q\overline{q}$ (uds and $c\overline{c}$) background events. The measurement of the $\tau^- \to K^-\eta\nu_\tau$ branching fraction is described in section 7.3 while section 7.4 describes the search for $\tau^- \to \pi^-\eta\nu_\tau$ decays.

7.1 Fitting the $\pi^+\pi^-\pi^0$ mass spectrum

The η meson decays via the $\eta \to \pi^+\pi^-\pi^0$ mode with a branching fraction of $(22.73 \pm 0.28)\%$ [15], making this the third most common η decay mode and the most common involving charged particles. The η meson has a mass of 547.853 ± 0.024 MeV/c^2 [15] and is seen in the $\pi^+\pi^-\pi^0$ mass spectrum as a peak centred near this mass.

To calculate the number of η mesons, the $\pi^+\pi^-\pi^0$ mass spectrum is fitted over the mass range 500 MeV/c^2 to 620 MeV/c^2 using a binned maximum likelihood fit. The combinatorial background is modelled as a second order polynomial while the peak within the η mass region, or 'η peak', is modelled as a double Gaussian function:

$$y = \frac{N}{\sqrt{2\pi}} \left\{ \frac{(1-R)}{\sigma_1} \exp\left[-\frac{(x-m_1)^2}{2\sigma_1^2} \right] + \frac{R}{\sigma_2} \exp\left[-\frac{(x-m_2)^2}{2\sigma_2^2} \right] \right\}, \qquad (7.2)$$

where N is the normalisation parameter, R is the ratio of the intensities of the two Gaussians, m_1 and m_2 are the peak masses of the Gaussians and σ_1 and σ_2 are the widths. A binned maximum likelihood fit is used because this procedure will correctly fit low statistics samples.

To count the number of η mesons in the sample the intensity of the η peak is obtained from the free parameter, N, of the fit. The parameters σ_1, σ_2, m_1, m_2 and R are all fixed; to find their best values, the mass spectrum from a high statistics sample of events is fitted while allowing all the parameters to float. Since the shape of the η peak may be different in the data and MC samples, the parameters are fixed to different values for each. For the MC events, the high statistics sample is the sum of e- and μ-tagged events from the dedicated $\tau^- \to \pi^-\eta\nu_\tau$ sample which have been selected as $\tau^- \to \pi^-\pi^+\pi^-\pi^0\nu_\tau$ candidates, and the e- and μ-tagged events from the dedicated $\tau^- \to K^-\eta\nu_\tau$ sample which have been selected as $\tau^- \to K^-\pi^+\pi^-\pi^0\nu_\tau$ candidates. The parameters found in the fit (see figure 7.1(a)) are 9.4 ± 0.3 MeV/c^2 and 3.80 ± 0.06 MeV/c^2 for σ_1 and σ_2, 546.8 ± 0.2 MeV/c^2 and 547.50 ± 0.04 MeV/c^2 for m_1 and m_2 and $(71 \pm 2)\%$ for R.

For the data events, the high statistics sample is the sum of π-tagged data events which have been selected to be $\tau^- \to \pi^-\pi^+\pi^-\pi^0\nu_\tau$ candidates or $\tau^- \to K^-\pi^+\pi^-\pi^0\nu_\tau$ candidates. To increase the statistics further, the selections on the thrust magnitude and total energy of the event are loosened to the values

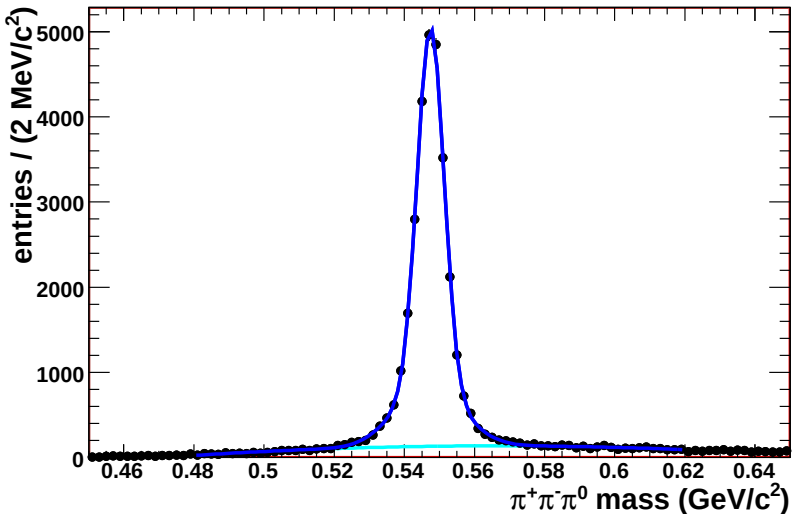

(a)

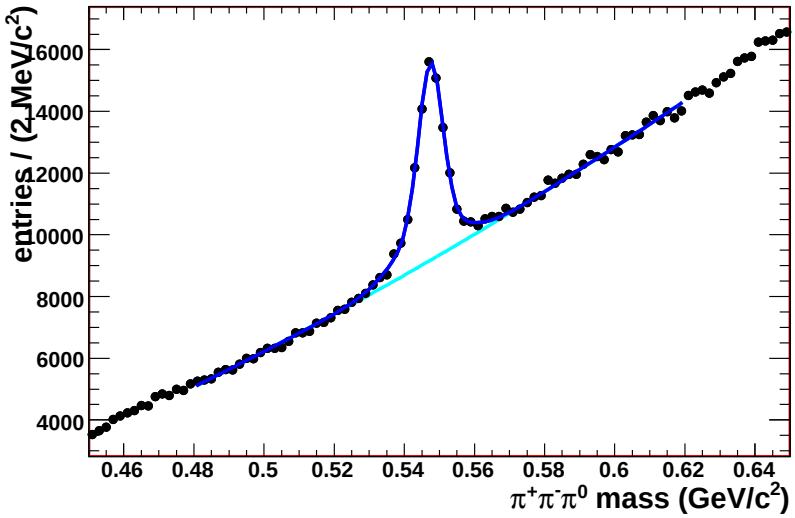

(b)

Figure 7.1: Invariant $\pi^+\pi^-\pi^0$ mass distribution of high statistics samples of (a) MC events and (b) data events. The spectra are fitted while allowing all the parameters to float, and for all proceeding fits the parameters σ_1, σ_2, m_1, m_2 and R are fixed to the values found here. The MC fit has a χ^2/NDF of 86/61 while the data fit has 84/61.

used for the 'increased statistics' sample, shown in table 7.1 in section 7.2.1. The parameters found in the fit (see figure 7.1(b)) are 8.6 ± 0.8 MeV/c^2 and 3.4 ± 0.1 MeV/c^2 for σ_1 and σ_2, 546.6 ± 0.5 MeV/c^2 and 547.52 ± 0.08 MeV/c^2 for m_1 and m_2 and $(62 \pm 4)\%$ for R.

The subsequent figures which show fits to the $\pi^+\pi^-\pi^0$ mass spectrum each have a box showing statistics from the fit: the χ^2 value divided by the number of degrees of freedom (χ^2/ndf), the three parameters which define the background polynomial function ($p0$, $p1$ and $p2$) and the normalisation parameter N which gives the intensity of the peak. The other five parameters of the fit are fixed to the values described above. All subsequent fits to the η peak are made in this way.

To measure the branching fractions of $\tau^- \to K^-\eta\nu_\tau$ and $\tau^- \to \pi^-\eta\nu_\tau$, the number of η mesons in the data must be counted and the number of η mesons contributed by each relevant background mode must be subtracted, as shown in equation 7.1. To calculate the number of η mesons in the data contributed by each τ-decay background mode, the τ-decay branching fractions measured by Belle and given in table 6.3 are used, rather than the average of these results with all previous results as reported by the Particle Data Group. This is done because the Belle Collaboration reports [16] that previous measurements underestimated the background contamination and this is an assumption which is supported by the results reported in this chapter. Therefore, the Belle measurements should supersede the previous measurements.

When the dedicated $\tau^- \to \pi^-\eta\pi^0\nu_\tau$, $\tau^- \to K^-\eta\pi^0\nu_\tau$ and $\tau^- \to \pi^-\eta\overline{K^0}\nu_\tau$ MC samples are normalised to the data luminosity, the branching fractions measured by Belle are used. When $\tau^- \to K^-\pi^+\pi^-\pi^0\nu_\tau$ candidates are selected, the $\tau^- \to K^-\eta\nu_\tau$ MC sample is normalised using the $\tau^- \to K^-\eta\nu_\tau$ branching fraction measured in this analysis, as reported in equation 7.4 (section 7.3.4). When $\tau^- \to \pi^-\pi^-\pi^+\pi^-\pi^0\nu_\tau$ candidates are selected, the $\tau^- \to K^-\eta\nu_\tau$ MC sample is normalised using the weighted average of the $\tau^- \to K^-\eta\nu_\tau$ branching fraction measured by Belle and the branching fraction measured in this analysis, as reported in equation 7.5 (section 7.3.4).

7.2 Simulated η production in $q\overline{q}$ events

All samples of simulated events are scaled to match the luminosity of the data. In addition, another scaling factor is applied to the $u\overline{u}/d\overline{d}/s\overline{s}$ (uds) and $c\overline{c}$ MC samples to correct for the poor simulation of η production in these modes.

7.2.1 Simulated η production in $u\overline{u}/d\overline{d}/s\overline{s}$ events

Although the $u\overline{u}+d\overline{d}+s\overline{s}$ cross section is known, the inclusive rate of η production from uds events is not fully understood; therefore, the uds MC sample may need to be corrected by applying a scaling factor. To calculate the scaling factor which should be applied to the uds MC simulation, an enriched sample of uds events is required from both data and MC. For this the π-tagged events are selected (as described in section 6.3.4). The statistics must be large enough to make a useful comparison between data and MC but the sample must also be as similar as possible to the e-tag and μ-tag samples which are used to measure the branching fractions, as described later in this chapter. Therefore, three samples (defined in table 7.1), each with a different purity of uds events, are examined.

The "τ selection" sample of events has the same selections as described in chapter 6, but applied to the π-tag sample of events. In order to calculate the uds scaling factor required for the $\tau^- \to K^-\pi^+\pi^-\pi^0\nu_\tau$ candidates, the bachelor track is required to be a kaon (as described in section 6.3.6). The sideband subtraction method described in section 6.3.6 is used to make the ηK^- mass spectrum, as shown in figure 7.2. When normalising the MC samples to the data luminosity, the $\tau^- \to K^-\eta\nu_\tau$ sample is normalised according to the $\tau^- \to K^-\eta\nu_\tau$ branching fraction reported in this chapter, in equation 7.4 (section 7.3.3). Since the $\tau^- \to K^-\eta\nu_\tau$ branching fraction reported in this chapter depends on the uds scaling factors, both have been recalculated in an iterative process (the dependence is small and only a single iteration is needed).

The $\pi^+\pi^-\pi^0$ mass spectrum is made for three bins of $K^-\pi^+\pi^-\pi^0$ mass, as shown in figure 7.3, for the data and MC samples. The $\pi^+\pi^-\pi^0$ mass spectra for the uds MC sample are fitted to give the numbers of η mesons, U, in the uds MC sample. The $\pi^+\pi^-\pi^0$ mass spectra for all non-uds MC samples are fitted to give the numbers of η mesons, N, in the non-uds modes. The $\pi^+\pi^-\pi^0$ mass spectra for the data sample are fitted to give the numbers of η mesons, D, in data. The uds scaling factor required to produce the same number of η mesons in data and MC

is calculated as $(D - N)/U$, for each bin of $K^-\pi^+\pi^-\pi^0$ mass. The resulting *uds* scaling factors for this "τ selection" sample of events are presented in table 7.1.

In order to calculate the *uds* scaling factor required for the $\tau^- \to \pi^-\pi^+\pi^-\pi^0\nu_\tau$ candidates, the bachelor track is required to be a pion (as described in section 6.3.6). The sideband subtraction method described in section 6.3.6 is used to make the $\eta\pi^-$ mass spectrum, as shown in figure 7.4. The shape of the $\eta\pi^-$ mass spectrum is poorly simulated. When normalising the MC samples to the data luminosity, the $\tau^- \to K^-\eta\nu_\tau$ sample is normalised according to the weighted average of the $\tau^- \to K^-\eta\nu_\tau$ branching factor found later in this chapter and the $\tau^- \to K^-\eta\nu_\tau$ branching fraction measured by Belle, as reported in equation 7.5 (section 7.3.3).

The 3π mass spectrum is made for three ranges of 4π mass, shown in figure 7.5. For each range of 4π mass, the *uds* scaling factor required to produce the same number of η mesons in data and MC is again calculated as $(D-N)/U$, as described above, and given in table 7.1 for the "τ selection" sample of events. For the $M(4\pi) < 1.1$ GeV/c^2 region, it can be seen from figure 7.5(a) that although scaling the *uds* sample by 3.03 will produce η peaks of the same intensity in data and MC, it will also reduce the agreement between data and MC in the sideband region. However, this does not affect the measured number of η mesons.

The "increased statistics" sample of events has looser cuts on the thrust and the reconstructed energy of the event. This increases the statistics of the sample, particularly for the *uds* events. This also allows more unsimulated events to pass the selections, both in the background continuum and the η peak, for low ηK^- and $\eta\pi^-$ masses. In particular, there are many unsimulated η mesons from the $a_0 \to \eta\pi^-$ mode in *uds* events in data. These features can been seen in figures B.1, B.2, B.3 and B.4 in appendix B. The *uds* scaling factors are calculated in the same way as described above, for this "increased statistics" sample, and included in table 7.1.

The "enhanced *uds*" sample of events is the same as the "increased statistics" sample except that the selection on the reconstructed energy is reversed. This further enhances the number of *uds* events, but results in a sample which is significantly different to the one used for the analysis presented in this chapter. The ηK^- mass spectrum (as shown in figure B.5 in appendix B) has more entries from the MC sample than from the data sample, for ηK^- masses up to the τ mass. This feature is also seen in the $\pi^+\pi^-\pi^0$ mass spectra in figure B.6. The shape

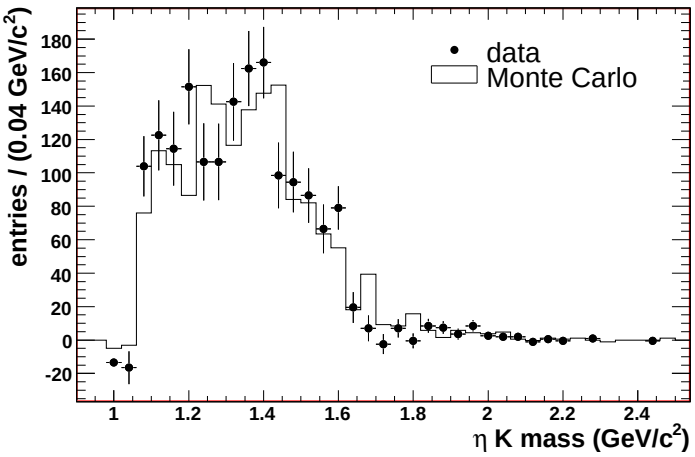

Figure 7.2: The ηK^- mass distribution of π-tagged events from the "τ selection" sample defined in table 7.1, obtained using the sideband subtraction method. The MC samples are normalised to the data luminosity but no additional $q\overline{q}$ scaling has been applied.

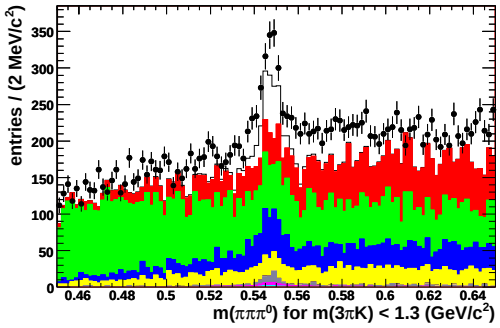

(a) $M(3\pi K) < 1.3$ GeV/c^2

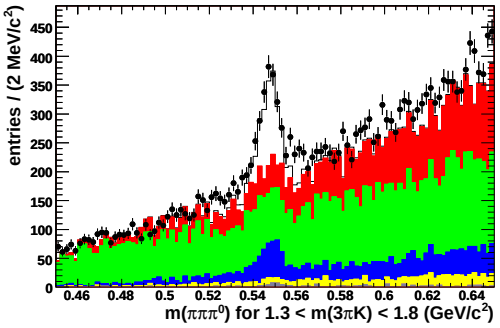

(b) $1.3 < M(3\pi K) < 1.8$ GeV/c^2

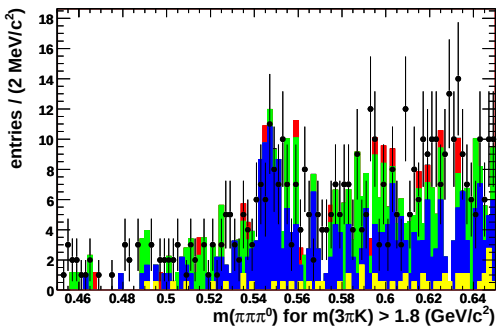

(c) $M(3\pi K) > 1.8$ GeV/c^2

Figure 7.3: The $\pi^+\pi^-\pi^0$ mass distribution of π-tagged events (selected for containing $K^-\pi^+\pi^-\pi^0$ candidates) from the "τ selection" sample defined in table 7.1. The MC samples are normalised to the data luminosity but no additional $q\overline{q}$ scaling has been applied.

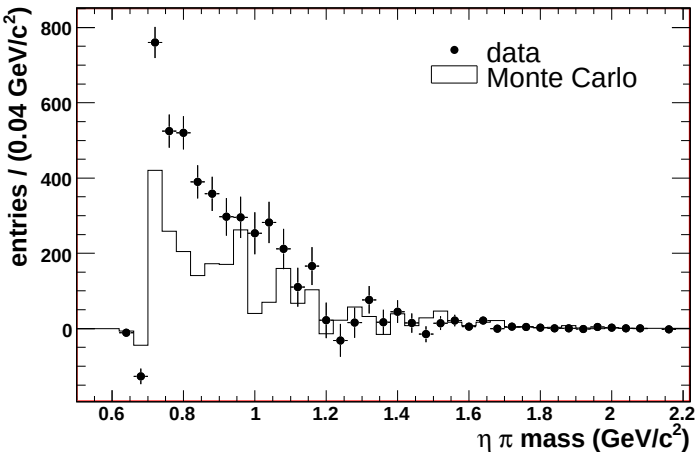

Figure 7.4: The $\eta\pi^-$ mass distribution of π-tagged events from the "τ selection" sample defined in table 7.1, obtained using the sideband subtraction method. The MC samples are normalised to the data luminosity but no additional $q\overline{q}$ scaling has been applied.

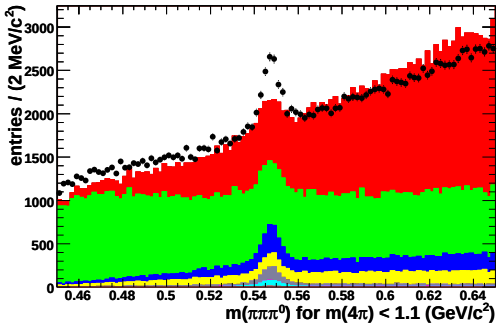

(a) $M(4\pi) < 1.1$ GeV/c^2

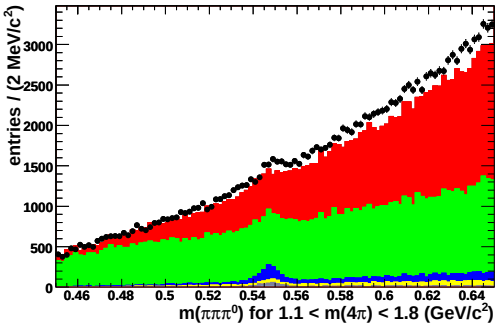

(b) $1.1 < M(4\pi) < 1.8$ GeV/c^2

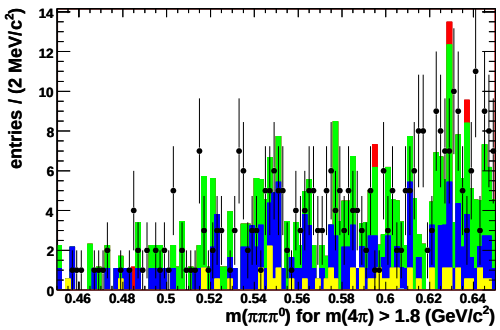

(c) $M(4\pi) > 1.8$ GeV/c^2

Figure 7.5: The $\pi^+\pi^-\pi^0$ mass distribution of π-tagged events (selected for containing $\pi^-\pi^+\pi^-\pi^0$ candidates) from the "τ selection" sample defined in table 7.1. The MC samples are normalised to the data luminosity but no additional $q\overline{q}$ scaling has been applied.

Selecting $K^-\pi^+\pi^-\pi^0\nu_\tau$ candidates				
		$3\pi K$ mass range (GeV/c^2)		
Sample	Selections	< 1.3	$1.3 - 1.8$	> 1.8
τ selection	$\epsilon < 0.80$; thrust > 0.95	1.26 ± 0.19	0.83 ± 0.12	$-$
Increased statistics	$\epsilon < 0.95$; thrust > 0.85	2.01 ± 0.16	1.11 ± 0.07	1.42 ± 0.12
Enhanced uds	$\epsilon > 0.95$; thrust > 0.85	0.50 ± 0.10	0.53 ± 0.06	1.07 ± 0.13
Selecting $\pi^-\pi^+\pi^-\pi^0\nu_\tau$ candidates				
		4π mass range (GeV/c^2)		
Sample	Selections	< 1.1	$1.1 - 1.8$	> 1.8
τ selection	$\epsilon < 0.80$; thrust > 0.95	3.03 ± 0.15	1.08 ± 0.08	$-$
Increased statistics	$\epsilon < 0.95$; thrust > 0.85	5.00 ± 0.14	1.28 ± 0.04	1.85 ± 0.16
Enhanced uds	$\epsilon > 0.95$; thrust > 0.85	0.83 ± 0.06	0.56 ± 0.03	1.08 ± 0.10

Table 7.1: The uds MC scaling factors for different ranges of $3\pi K$ and 4π mass. There are three different samples of events, each with different selections made on the measured energy divided by the initial energy of the event, ϵ, and the thrust magnitude.

of the $\eta\pi^-$ mass spectrum (as shown in figure B.7) is still poorly simulated; the number of simulated a_0 decays is approximately correct, but at higher 4π masses the spectrum shows more entries in MC than data. There are also unsimulated background events with a 3π mass below 0.54 GeV/c^2 (as shown in figure B.8), although these events should appear as continuum background only. The *uds* scaling factors are calculated again, for this "enhanced *uds*" sample, and included in table 7.1.

In summary, the *uds* data are not well simulated and the required *uds* scaling factor varies with both $K^-\pi^+\pi^-\pi^0$ and $\pi^\pm\pi^+\pi^-\pi^0$ mass. Scaling factors for the *uds* sample are taken as 1.0 ± 0.5 for the $K^-\pi^+\pi^-\pi^0$ analysis and 1.5 ± 1.0 for $\pi^-\pi^+\pi^-\pi^0$, to cover the uncertainty in the physics involved. The $uds \to \pi^-\eta$ candidates require a scaling factor with a large uncertainty because of the poorly simulated $a_0 \to \eta\pi^-$ production in *uds* events.

7.2.2 η production in simulated $c\overline{c}$ events

The $c\overline{c}$ events contain two charm particles which use up much of the CM energy, leaving little left for the production of η mesons and other particles. In addition, the branching fractions ($\mathcal{B}$) for the decays of charm mesons and baryons are typically known with a $\sim 10\%$ uncertainty; for example, $\mathcal{B}(D^- \to \pi^-\eta) = (3.39 \pm 0.29) \times 10^{-3}$ and $\mathcal{B}(D_s^- \to \pi^-\eta) = (1.58 \pm 0.21)\%$. Thus the simulation of η mesons in $c\overline{c}$ events is more reliable than in the *uds* events. However, the $c\overline{c}$ MC sample may still need to be corrected with a scaling factor.

To calculate the possible $c\overline{c}$ scaling factor, $\tau^- \to \pi^-\pi^+\pi^-\pi^0\nu_\tau$ candidates are selected from the e- and μ-tagged samples. To enhance the number of $c\overline{c}$ events the selection made on the thrust magnitude is removed and events with a $\pi^\pm\pi^+\pi^-\pi^0$ mass greater than the τ mass are selected.

The $\eta\pi^-$ mass distribution of this "enhanced $c\overline{c}$" sample, as shown in figure 7.6, is found using the sideband subtraction method. As well as being normalised to the data luminosity, the *uds* MC sample is scaled by 1.5, the factor found in section 7.2.1. Peaks can be seen which correspond to the $D^- \to \pi^-\eta$ and $D_s^- \to \pi^-\eta$ decays, at masses of 1869.3 GeV/c^2 and 1968.2 GeV/c^2 respectively [15]. The MC samples show that the events in these $\eta\pi^-$ mass bins are almost exclusively $c\overline{c}$ events.

The number of data and MC events in the $\eta\pi^-$ mass bins corresponding to the D^- and D_s^- meson masses are counted. To calculate the factor that the $c\overline{c}$

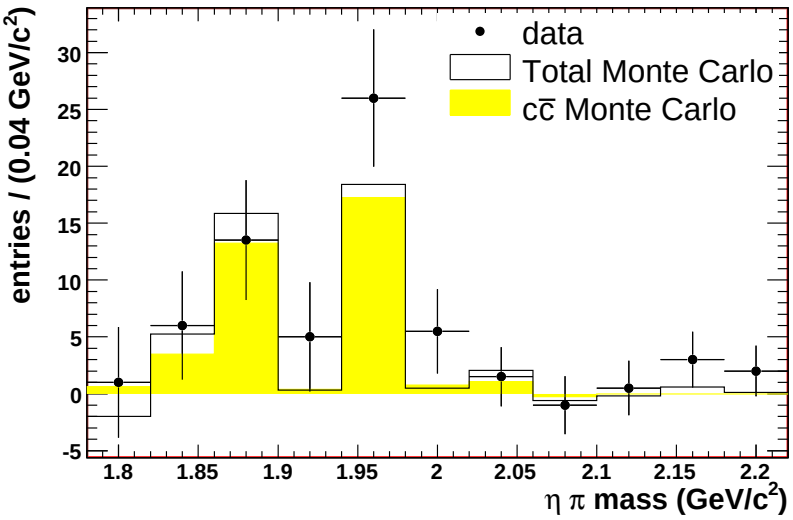

Figure 7.6: The $\eta\pi^-$ mass distribution for e- and μ-tagged events with a $\pi^\pm\pi^+\pi^-\pi^0$ mass greater than the τ mass. The MC samples are normalised to the data luminosity. In addition, the uds MC sample is scaled by 1.5, the factor found in section 7.2.1.

simulation should be scaled by to give the best representation of the data, the variable χ^2 is calculated as

$$\chi^2 = \frac{(\alpha M_1 - D_1)^2}{\alpha^2\sigma_{M1}^2 + \sigma_{D1}^2} + \frac{(\alpha M_2 - D_2)^2}{\alpha^2\sigma_{M2}^2 + \sigma_{D2}^2}, \tag{7.3}$$

where $M_1 \pm \sigma_{M1}$ and $M_2 \pm \sigma_{M2}$ are the numbers of MC events in the $\eta\pi^-$ mass bins corresponding to the D^- and D_s^- meson masses, $D_1 \pm \sigma_{D1}$ and $D_2 \pm \sigma_{D2}$ are the numbers of data events in the $\eta\pi^-$ mass bins corresponding to the D^- and D_s^- meson masses and α is the $c\overline{c}$ MC scaling factor.

The value of α which minimises χ^2 is 1.2 ± 0.3, which is therefore chosen as the $c\overline{c}$ scaling factor for the $K^-\pi^+\pi^-\pi^0$ and $\pi^-\pi^+\pi^-\pi^0$ analyses.

7.3 The $\tau^- \to K^-\eta\nu_\tau$ branching fraction

For this measurement, e- and μ-tagged $\tau^- \to K^-\pi^+\pi^-\pi^0\nu_\tau$ candidates are selected (as described in section 6.3.6).

Section 7.3.1 describes how the expected number of η mesons in each relevant MC background mode is calculated. Section 7.3.2 describes how the signal

efficiency is calculated by counting the number of η mesons in the dedicated $\tau^- \to K^-\eta\nu_\tau$ MC sample. The $\tau^- \to K^-\eta\nu_\tau$ branching fraction is calculated in section 7.3.3 by counting the number of η mesons in the data sample and subtracting the total number of η mesons from all the background modes. Section 7.3.4 outlines the systematic uncertainties on the result.

7.3.1 Background contributions to $\tau^- \to K^-\eta\nu_\tau$

Figure 7.7 shows the invariant $\pi^+\pi^-\pi^0$ mass distribution for the total MC and data samples, for e- and μ-tagged events, with an η peak clearly seen. The number of η mesons in each MC background sample is counted by fitting the $\pi^+\pi^-\pi^0$ mass spectrum for that sample, as described at the beginning of this chapter.

The background modes which do not contain any η mesons are called continuum backgrounds. The main continuum background modes are the $\tau^- \to \pi^-\omega\nu_\tau$ mode and other non-η τ background modes, which are both included in the generic τ MC sample. The $B^0\overline{B}^0$ mode and the B^+B^- mode are minor continuum background modes. The e-tagged events also include unsimulated, continuum Bhabha events at lower $\pi^+\pi^-\pi^0$ masses.

The modes that do contain $\eta \to \pi^+\pi^-\pi^0$ decays contribute to the η peak. The $q\overline{q}$ events, mainly $c\overline{c}$ with some uds events, can produce η mesons. There are also τ decay modes which contain η mesons, such as $\tau^- \to \pi^-\eta\pi^0\nu_\tau$, $\tau^- \to K^-\eta\pi^0\nu_\tau$ and $\tau^- \to \pi^-\eta\overline{K^0}\nu_\tau$. The number of $\eta \to \pi^+\pi^-\pi^0$ decays contributed by each background mode is calculated as described below, using MC samples, and the fits are shown in appendix C.

The $q\overline{q}$ background contributions: The number of η mesons in the uds MC sample is calculated by fitting the $\pi^+\pi^-\pi^0$ mass spectrum, as shown in figure C.1. This number is multiplied by the factor found in section 7.2.1, to give the number of η mesons expected in the data sample to come from uds events. The expected background contribution from uds events in the e-tagged data sample is found to be 4.5 ± 3.5 η mesons, while 8.9 ± 6.5 are expected in the μ-tagged data sample.

The number of η mesons in the $c\overline{c}$ MC sample is calculated by fitting the $\pi^+\pi^-\pi^0$ mass spectrum, as shown in figure C.2. In a similar way as for the uds events, the number of η mesons in the MC sample is multiplied by the factor

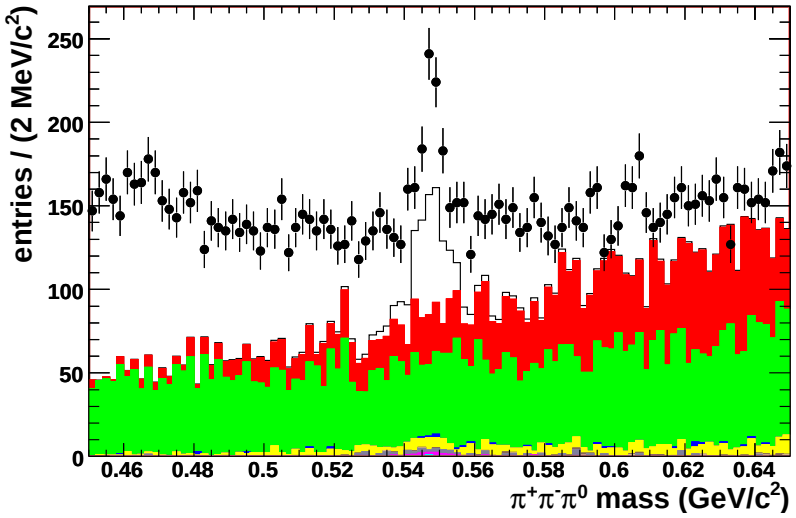

(a) e-tag events

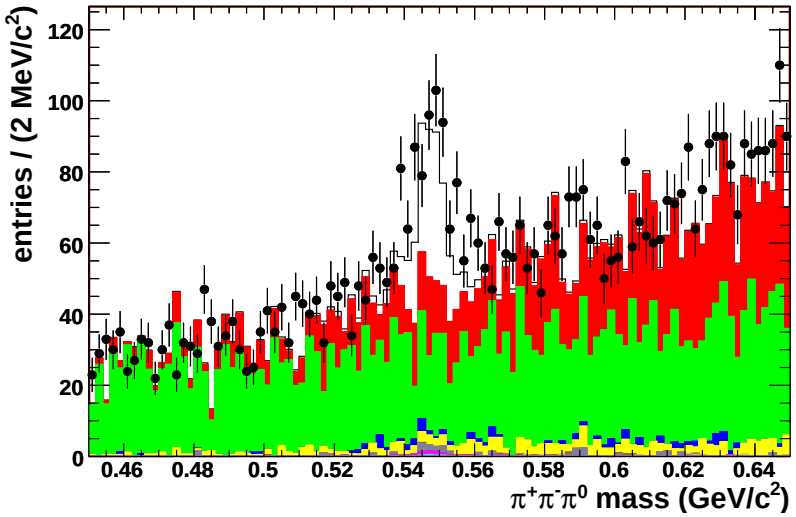

(b) μ-tag events

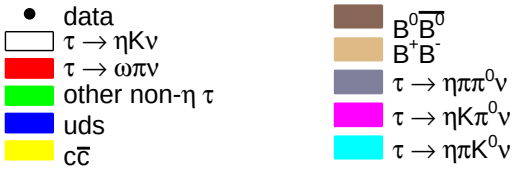

Figure 7.7: Invariant $\pi^+\pi^-\pi^0$ mass distribution for $K^-\pi^+\pi^-\pi^0$ candidates, selected from the data and MC samples. The MC samples are normalised to the data luminosity. For illustrative purposes, the $\tau^- \to K^-\eta\nu_\tau$ sample is normalised using the branching fraction measured by this analysis, in equation 7.4 (section 7.3.4). In addition, the $c\bar{c}$ background sample is scaled by 1.2 (as described in section 7.2).

found in section 7.2.2 to give the number of η mesons in the data sample that are expected to come from $c\bar{c}$ events. The expected background contribution from $c\bar{c}$ events in the e-tagged data sample is found to be 14 ± 9 η mesons, while 0.7 ± 5.5 are expected in the μ-tagged data sample.

The τ background contributions: The number of η mesons in the dedicated MC samples for each background τ-decay mode is calculated by fitting the $\pi^+\pi^-\pi^0$ mass spectra, as shown in figures C.3, C.4 and C.5.

Table 7.2 shows the probability of an event from a background mode passing all the selections and contributing an η meson to the η peak. This is calculated for each background mode by dividing the number of η mesons in the MC sample by the total number of events in the sample before selections are made (from table 6.1).

τ background	Misidentification probability	
	e-tag	μ-tag
$\tau^- \to K^-\eta\pi^0\nu_\tau$	$(2.2 \pm 0.1) \times 10^{-4}$	$(1.3 \pm 0.1) \times 10^{-4}$
$\tau^- \to \pi^-\eta\pi^0\nu_\tau$	$(1.2 \pm 0.3) \times 10^{-5}$	$(3 \pm 2) \times 10^{-6}$
$\tau^- \to \pi^-\eta\overline{K^0}\nu_\tau$	$(5.3 \pm 0.7) \times 10^{-5}$	$(3.1 \pm 0.5) \times 10^{-5}$

Table 7.2: The probability that an η meson from a background τ-decay mode will contribute to the η peak for the ηK^- analysis.

These misidentification probabilities, together with the luminosity of the data and the branching fractions in table 6.3, are used to calculate the number of η mesons in the data sample that are expected to come from each of these background τ-decay modes. There are expected to be no η mesons from the $\tau^- \to \pi^-\eta\nu_\tau$ mode because the branching fraction for $\tau^- \to \pi^-\eta\nu_\tau$ decays is assumed to be zero, consistent with the result reported in section 7.4.5.

The total background contributions: Table 7.3 shows a summary of the numbers of η mesons expected in the data sample to come from the background modes. When combining the e-tag and μ-tag numbers, uncertainties which are correlated between the two samples are treated differently from those that are uncorrelated.

For each entry, the first error is the statistical uncertainty from the $\pi^+\pi^-\pi^0$ mass spectra fits, due largely to the limited MC statistics. For these errors, the e-

Background contribution	Expected number of events					
	e-tag			μ-tag		
$c\bar{c}$	13.8	± 8.3	± 3.5	0.7	± 5.5	± 0.2
uds	4.5	± 2.7	± 2.3	8.9	± 4.7	± 4.5
$\tau^- \to K^-\eta\pi^0\nu_\tau$	8.4	± 0.5	± 2.1	5.0	± 0.4	± 1.3
$\tau^- \to \pi^-\eta\pi^0\nu_\tau$	13.3	± 3.7	± 0.7	2.9	± 2.0	± 0.2
$\tau^- \to \pi^-\eta\overline{K^0}\nu_\tau$	3.9	± 0.5	± 0.7	2.3	± 0.4	± 0.4
Total background	44	± 10	± 5	20	± 8	± 5
Combined e- and μ-tag	$64 \pm 12 \pm 8$					
Data	463	± 44	± 12	291	± 30	± 10
Combined e- and μ-tag	$754 \pm 53 \pm 16$					
Observed signal (data − background)	419	± 44	± 16	271	± 30	± 13
Combined e- and μ-tag	$690 \pm 53 \pm 22$					

Table 7.3: The numbers of η mesons in the data sample for ηK^- candidates that are expected to come from each background mode (as found in section 7.3.1) and the number of η mesons in the data sample (as found in section 7.3.3). The observed signal is the number of η mesons in the data after all the background contributions have been subtracted (as described in section 7.3.3). For each entry, the first error is statistical (due to the limited MC statistics) and the second error is systematic(due to the uncertainties on the τ-decay branching fractions and $q\overline{q}$ simulation factors). The statistical error on the observed signal is equal to the statistical error on the data. The systematic uncertainty on the observed signal is equal to the systematic uncertainty on the data added in quadrature with the statistical and systematic uncertainties on the background contributions. The systematic uncertainties are discussed further in section 7.3.4 and included in table 7.4.

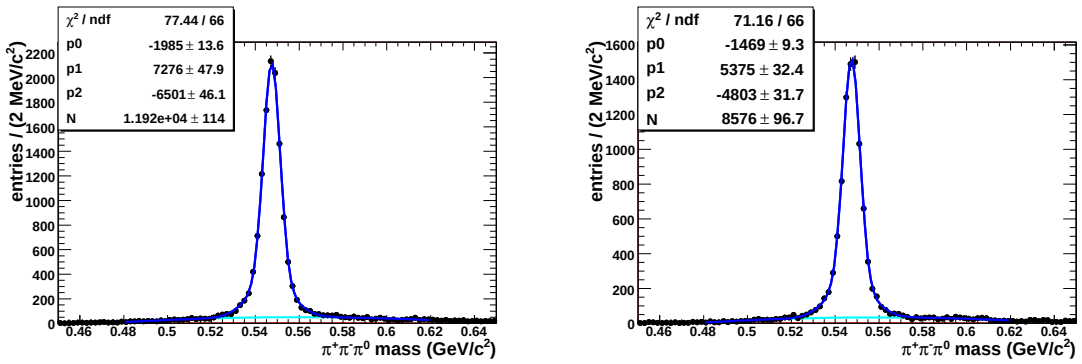

(a) e-tag events (b) μ-tag events

Figure 7.8: The $\pi^+\pi^-\pi^0$ mass distribution for $K^-\pi^+\pi^-\pi^0$ candidates selected from the dedicated $\tau^- \to K^-\eta\nu_\tau$ MC sample.

tag and μ-tag contributions are uncorrelated so they can be added in quadrature to produce the error on the combined e- and μ-tagged sample.

The second error is the systematic uncertainty due to the uncertainties in the branching fractions of the τ-decay background modes and due to the uncertainties on the uds and $c\overline{c}$ scaling factors. For these uncertainties, the e-tag and μ-tag contributions are correlated. The error on the combined e- and μ-tagged sample is calculated directly from the combined sample (instead of by combining the errors calculated separately for the e-tagged and μ-tagged samples). Both the statistical and systematic uncertainties on the background contributions are included in the systematic uncertainty on the final measurement of the $\tau^- \to K^-\eta\nu_\tau$ branching fraction, as described in section 7.3.4.

7.3.2 Signal efficiency for $\tau^- \to K^-\eta\nu_\tau$

The signal efficiency is the probability that genuine $\tau^- \to K^-\eta\nu_\tau$ events pass all the selections and contribute an η meson to the η peak. Figure 7.8 shows the $\pi^+\pi^-\pi^0$ mass spectra for the dedicated $\tau^- \to K^-\eta\nu_\tau$ MC samples, which are fitted to calculate the number of η mesons in the sample. This number is divided by the total number of events in the $\tau^- \to K^-\eta\nu_\tau$ sample (from table 6.1) to calculate the signal efficiency. The signal efficiency is found to be $(0.336\pm0.003)\%$ for e-tagged events and $(0.242 \pm 0.003)\%$ for μ-tagged events, resulting in an overall signal efficiency for e- and μ-tagged events of $(0.578 \pm 0.004)\%$, where the errors given are statistical only. The uncertainty on the signal efficiency is

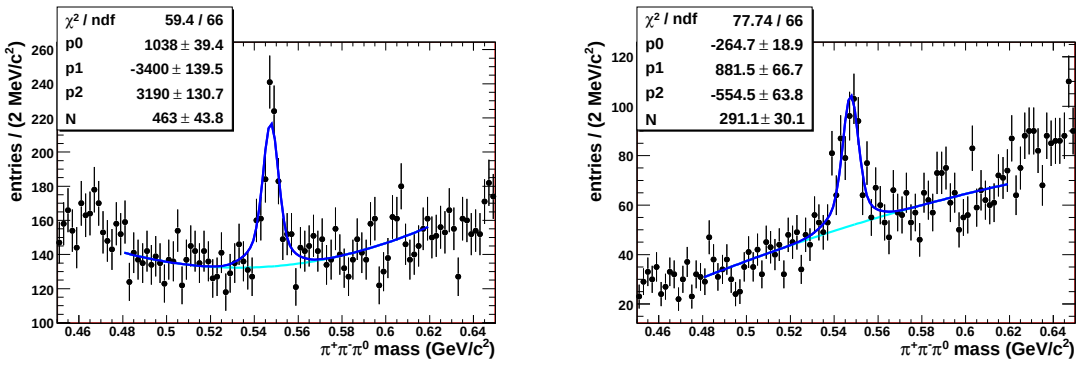

(a) e-tag events (b) μ-tag events

Figure 7.9: Invariant $\pi^+\pi^-\pi^0$ distribution for $K^-\pi^+\pi^-\pi^0$ candidates selected from the data sample.

included in the systematic uncertainty on the $\tau^- \to K^-\eta\nu_\tau$ branching fraction measurement (as described in section 7.3.4).

7.3.3 Results for the $\tau^- \to K^-\eta\nu_\tau$ branching fraction

Figure 7.9 shows the $\pi^+\pi^-\pi^0$ mass spectra for the data sample, fitted to count the numbers of η mesons. There are found to be 463 ± 44 η mesons in the e-tagged data sample and 291 ± 30 η mesons in the μ-tagged data sample.

The total number of η mesons in the data sample that are expected to come from background modes was reported in section 7.3.1 to be 44 ± 11 for the e-tagged sample and 20 ± 9 for the μ-tagged sample. These background contributions are subtracted from the number of η mesons seen in data, as shown in table 7.3, to give the observed signal, which is the number of η mesons in data expected to have come from $\tau^- \to K^-\eta\nu_\tau$ decays.

The branching fraction is calculated using equation 7.1, where $N_{data} - N_{bkgd}$ is the observed signal given in table 7.3, N_{total} is 864 million, ϵ is the signal efficiency given in section 7.3.2 and f is 0.978. Therefore, $\mathcal{B}(\tau^- \to K^-\eta\nu_\tau) = (1.48 \pm 0.15) \times 10^{-4}$ for e-tagged events and $\mathcal{B}(\tau^- \to K^-\eta\nu_\tau) = (1.33 \pm 0.15) \times 10^{-4}$ for μ-tagged events. Combining these branching fractions is complicated by correlations between the e-tagged and μ-tagged samples, so the branching fraction for the combined e- and μ-tagged sample is calculated directly using the 'Combined e- and μ-tag' numbers in table 7.3. Therefore, $\mathcal{B}(\tau^- \to K^-\eta\nu_\tau) = (1.42 \pm 0.11) \times 10^{-4}$ for the combined e- and μ-tagged sample.

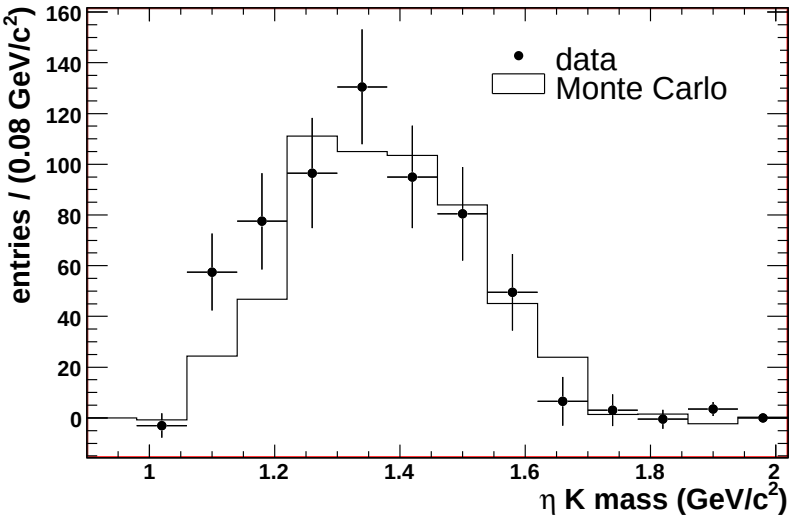

Figure 7.10: The ηK^- mass distribution in data and MC for e- and μ-tagged events, obtained using the sideband subtraction method. The MC samples are normalised to the data luminosity. For illustrative purposes, the $\tau^- \to K^-\eta\nu_\tau$ sample is normalised using the branching fraction measured by this analysis, in equation 7.4 (section 7.3.4). In addition, the $c\overline{c}$ background sample is scaled by 1.2 (as described in section 7.2).

The errors quoted are the statistical errors, coming purely from the statistical uncertainty on the fits to the data mass spectra (in table 7.3). The systematic uncertainties are described in the following section.

Figure 7.10 shows the ηK^- mass spectrum for e-tagged and μ-tagged events, obtained for data and MC using the sideband subtraction method. The $\tau^- \to K^-\eta\nu_\tau$ MC sample is normalised to the data luminosity according to the $\tau^- \to K^-\eta\nu_\tau$ branching fraction reported in this section (equation 7.4).

7.3.4 Systematic uncertainties for $\tau^- \to K^-\eta\nu_\tau$

The following sources of uncertainty are accounted for in the systematic error on the $\tau^- \to K^-\eta\nu_\tau$ branching fraction measurement. The systematic uncertainties are listed quantitatively in tables 7.3 and 7.4. The uncertainties on the combined e- and μ-tagged sample are calculated directly from the combined sample (instead of by combining the errors calculated separately from the e-tagged and μ-tagged samples), thus avoiding problems caused by correlations between the e-tagged and μ-tagged samples. To calculate the total systematic uncertainty on the $\tau^- \to$

$K^-\eta\nu_\tau$ branching fraction each systematic uncertainty in table 7.3 is expressed as a percentage of the observed signal and added in quadrature with the other errors listed in this section, as shown in table 7.4.

For the following uncertainties, the e-tag and μ-tag contributions are correlated:

- Branching fractions: The uncertainty on the τ-decay branching fractions (the Belle branching fractions from table 6.3) and the $q\overline{q}$ simulations is listed in table 7.3 as ± 8 events for the combined e- and μ-tagged sample. This uncertainty is applied to the observed signal of 690 events, giving an uncertainty of 1.2% on the $\tau^- \to K^-\eta\nu_\tau$ branching fraction, as shown in table 7.4. (Similarly, the uncertainty is $5/419 = 1.1\%$ for the e-tagged sample and $5/271 = 1.7\%$ for the μ-tagged sample).

- Bachelor kaon PID: As described in section 4.4, the PID efficiency corrections applied to the MC events have corresponding uncertainties. The uncertainty on the PID efficiency correction applied for the *KLHTight* kaon candidate list is 1.2%.

- Tracking efficiency: As described in section 4.4, there is an uncertainty on the tracking efficiency of charged particles. An uncertainty of 0.5% is assigned to each of the four tracks and added linearly, giving an uncertainty of 2.0%.

- π^0 detection efficiency: As described in chapter 5, there is an uncertainty of 0.85% on the π^0 detection efficiency, assigned for the π^0 candidate.

- Luminosity: An estimated uncertainty of 0.5% is correlated between the different Runs, while an estimated uncertainty of 0.42% is uncorrelated. The total uncertainty when combining Runs 1 through 6 is 0.65% [64].

- $\tau^+\tau^-$ cross section: The cross section for τ production at $\Upsilon(4S)$ is 0.919 ± 0.003 nb [21], giving a 0.31% systematic uncertainty.

For the following uncertainties, the e-tag and μ-tag contributions are uncorrelated:

- MC statistics of background contributions: Table 7.3 shows that, for the combined e- and μ-tagged sample, there is an uncertainty of ± 12 events

on the background contributions, due mainly to the limited MC statistics. This uncertainty is applied to the observed signal of 690 events, giving an uncertainty of 1.8% on the $\tau^- \to K^-\eta\nu_\tau$ branching fraction, as shown in table 7.4. (Similarly, the uncertainty is $10/419 = 2.3\%$ for the e-tagged sample and $8/271 = 2.8\%$ for the μ-tagged sample).

- Error on efficiency due to MC statistics: The statistical uncertainty on the signal efficiency, calculated in section 7.3.2, is $0.004/0.578 = 0.7\%$ for the combined e- and μ-tagged sample. (Similarly, the uncertainty is $0.003/0.336 = 1.0\%$ for the e-tagged sample and $0.003/0.242 = 1.1\%$ for the μ-tagged sample).

- Fitting to data: The values of each of the five fixed double-Gaussian parameters are increased and decreased, one at a time, by one standard deviation. The largest difference in the number of η mesons counted in the data sample is ± 16 for the combined e- and μ-tagged sample, as shown in table 7.3. This uncertainty is applied to the observed signal of 690 events, giving an uncertainty of 2.3% on the $\tau^- \to K^-\eta\nu_\tau$ branching fraction, as shown in table 7.4. (Similarly, the uncertainty is $12/419 = 2.9\%$ for the e-tagged sample and $10/271 = 3.7\%$ for the μ-tagged sample). For the MC samples this uncertainty is negligible when compared to the other uncertainties.

- Tag particle ID: As described in section 4.4, the PID efficiency corrections applied to MC events have corresponding uncertainties. The uncertainty on the corrections applied for the *pidLHElectron* electron candidate list is 0.7% and for the *muNNTight* muon candidate list is 1.8%. For the combined e- and μ-tagged sample, the uncertainties are weighted by the relative numbers of e-tagged and μ-tagged events to give 1.1%.

The total systematic uncertainties listed in table 7.4 are applied to the $\tau^- \to K^-\eta\nu_\tau$ branching fractions calculated in the previous section. For the e-tag sample of events the $\tau^- \to K^-\eta\nu_\tau$ branching fraction is $(1.48 \pm 0.15 \pm 0.07) \times 10^{-4}$ while for the μ-tag sample of events it is $(1.33 \pm 0.15 \pm 0.08) \times 10^{-4}$. For the combined e- and μ-tagged sample, the branching fraction is found to be:

$$\mathcal{B}(\tau^- \to K^-\eta\nu_\tau) = 1.42 \pm 0.11(\text{stat}) \pm 0.06(\text{syst}) \times 10^{-4}. \qquad (7.4)$$

This is compatible with the recent Belle measurement of $(1.58 \pm 0.05 \pm 0.09) \times$

Source	e-tag	μ-tag	e- and μ-tag
Fitting to data	2.9%	3.7%	2.3%
Tracking efficiency	2.0%	2.0%	2.0%
MC statistics of background contributions	2.3%	2.8%	1.8%
Branching fractions	1.1%	1.7%	1.2%
Bachelor K^- PID	1.2%	1.2%	1.2%
e-tag, μ-tag PID	0.7%	1.8%	1.1%
π^0 efficiency	0.9%	0.9%	0.9%
Luminosity and $\sigma_{\tau^+\tau^-}$	0.7%	0.7%	0.7%
Error on efficiency due to MC statistics	1.0%	1.1%	0.7%
Total systematic uncertainty	4.8%	5.9%	4.3%

Table 7.4: The systematic uncertainties on the measurement of the $\tau^- \to K^-\eta\nu_\tau$ branching fraction. The systematic uncertainties in table 7.3 have been expressed as percentages so that they can be included. The entries in each column are added in quadrature to give the total systematic uncertainty.

10^{-4} [16] for the $\tau^- \to K^-\eta\nu_\tau$ branching fraction, which used the $\eta \to \gamma\gamma$ and the $\eta \to \pi^+\pi^-\pi^0$ decay modes (a branching fraction of $(1.60 \pm 0.15 \pm 0.10) \times 10^{-4}$ is reported from the $\eta \to \pi^+\pi^-\pi^0$ decay mode alone). In the paper which presents this result [16], the Belle Collaboration suggest that previous $\tau^- \to K^-\eta\nu_\tau$ measurements [17, 31] underestimated background contamination, an assertion that is consistent with the result presented here. The weighted average of the Belle result and this result is

$$\mathcal{B}(\tau^- \to K^-\eta\nu_\tau) = (1.52 \pm 0.08) \times 10^{-4}, \tag{7.5}$$

where small correlations between the Belle and *BABAR* systematic uncertainties have not been taken into account. In section 7.4, this branching fraction is used to normalise the $\tau^- \to K^-\eta\nu_\tau$ MC sample to the data luminosity.

7.4 Search for $\tau^- \to \pi^-\eta\nu_\tau$ decays

To search for $\tau^- \to \pi^-\eta\nu_\tau$ decays, e- and μ-tagged $\tau^- \to \pi^-\pi^+\pi^-\pi^0\nu_\tau$ candidates are selected (as described in section 6.3.6). To avoid bias in the search, this analysis is carried out blind, which means that the η region in the data sample is kept hidden until the all cuts and selections have been chosen.

Section 7.4.1 describes how the expected number of η mesons in each relevant MC background mode is calculated. Section 7.4.2 describes how the signal efficiency is calculated by counting the number of η mesons in the dedicated $\tau^- \to \pi^-\eta\nu_\tau$ MC sample. Section 7.4.3 describes the systematic uncertainties on the measurement and section 7.4.4 presents the expected upper limit on the $\tau^- \to \pi^-\eta\nu_\tau$ branching fraction if no $\tau^- \to \pi^-\eta\nu_\tau$ signal events are observed. The $\tau^- \to \pi^-\eta\nu_\tau$ branching fraction, and an upper limit, is calculated in section 7.4.5 by counting the number of η mesons in the unblinded data sample and subtracting the total number of η mesons from all the background modes.

7.4.1 Background contributions to $\tau^- \to \pi^-\eta\nu_\tau$

Figure 7.11 shows the invariant $\pi^+\pi^-\pi^0$ mass distribution for the total MC sample, for e- and μ-tagged events, with an η peak clearly seen. The number of η mesons in each MC background sample is counted by fitting the $\pi^+\pi^-\pi^0$ mass spectrum for that sample, as described at the beginning of this chapter.

The background modes which do not contain any η mesons are called continuum backgrounds and are the same modes as for the $\tau^- \to K^-\eta\nu_\tau$ analysis, in section 7.3.1.

The $q\overline{q}$ events, mainly $c\overline{c}$, can produce η mesons. There are also τ decay modes which contain η mesons, such as $\tau^- \to \pi^-\eta\pi^0\nu_\tau$, $\tau^- \to K^-\eta\pi^0\nu_\tau$, $\tau^- \to \pi^-\eta\overline{K^0}\nu_\tau$ and $\tau^- \to K^-\eta\nu_\tau$. The number of $\eta \to \pi^+\pi^-\pi^0$ decays contributed by each background mode is calculated as described below, using MC samples, and the fits are shown in appendix D.

The $q\overline{q}$ background contributions: The number of η mesons in the uds MC sample is calculated by fitting to the $\pi^+\pi^-\pi^0$ mass spectrum, as shown in figure D.1. This is multiplied by the factor found in section 7.2.1 to give the number of η mesons in the data sample that are expected to come from uds events. The expected η meson background contribution from uds events in the e-tagged data sample is found to be 20 ± 16, while 64 ± 45 η mesons are expected in the μ-tagged data sample.

The number of η mesons in the $c\overline{c}$ MC sample is calculated by fitting to the $\pi^+\pi^-\pi^0$ mass spectrum, as shown in figure D.2. In the same way as for the uds events, the number of η mesons in the MC sample is multiplied by the factor found in section 7.2.2 to give the number of η mesons in the data sample which are

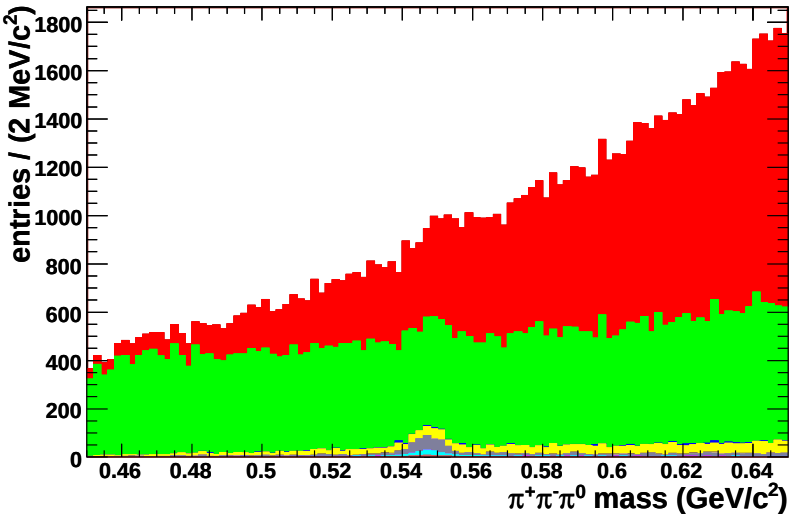

(a) e-tag events

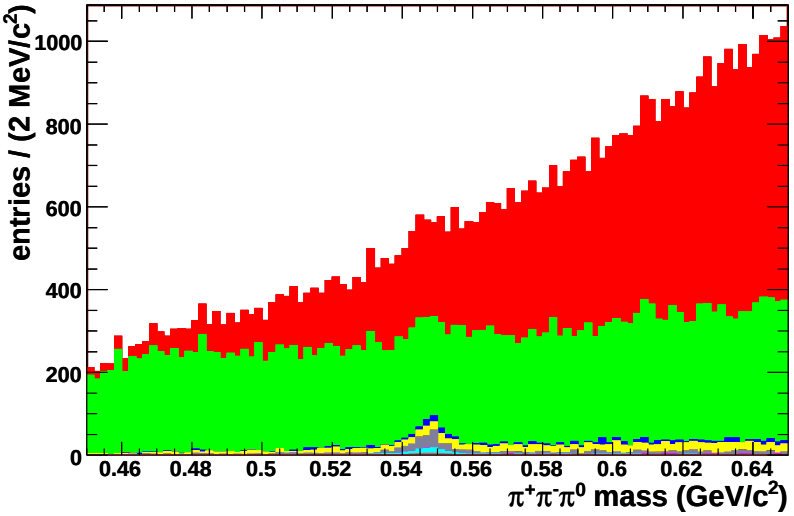

(b) μ-tag events

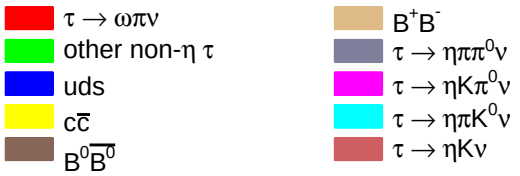

Figure 7.11: Invariant $\pi^+\pi^-\pi^0$ mass distribution for $\pi^-\pi^+\pi^-\pi^0$ candidates selected from the MC samples. The MC samples are normalised to the data luminosity. The $\tau^- \to K^-\eta\nu_\tau$ sample is normalised using the branching fraction in equation 7.5 (section 7.3.4). In addition, the uds and $c\overline{c}$ background sample are scaled by 1.5 and 1.2 respectively (as described in section 7.2).

expected to come from $c\overline{c}$ events. The expected η meson background contribution from $c\overline{c}$ events in the e-tagged data sample is found to be 74 ± 28, while 54 ± 20 η mesons are expected in the μ-tagged data sample.

The τ background contributions: The number of η mesons in the dedicated MC samples for each background τ-decay mode are calculated by fitting the $\pi^+\pi^-\pi^0$ mass spectra, as shown in figures D.3, D.4, D.5 and D.6.

Table 7.5 gives the probability of an event from a background mode passing all the selections and contributing an η meson to the η peak. This is calculated for each background mode by dividing the number of η mesons in the dedicated MC sample by the total number of events in the sample before selections are made (from table 6.1).

τ background	Misidentification probability	
	e-tag	μ-tag
$\tau^- \to \pi^-\eta\pi^0\nu_\tau$	$(1.9 \pm 0.1) \times 10^{-4}$	$(1.03 \pm 0.09) \times 10^{-4}$
$\tau^- \to \pi^-\eta\overline{K^0}\nu_\tau$	$(1.35 \pm 0.03) \times 10^{-3}$	$(9.6 \pm 0.3) \times 10^{-4}$
$\tau^- \to K^-\eta\nu_\tau$	$(2.7 \pm 0.1) \times 10^{-4}$	$(2.02 \pm 0.09) \times 10^{-4}$
$\tau^- \to K^-\eta\pi^0\nu_\tau$	$(1.5 \pm 0.6) \times 10^{-5}$	$(6 \pm 4) \times 10^{-6}$

Table 7.5: The probability that an η mesons from a background τ-decay mode will contribute to the η peak for the $\eta\pi^-$ analysis.

These misidentification probabilities, together with the luminosity of the data, the branching fractions in table 6.3 and the $\tau^- \to K^-\eta\nu_\tau$ branching fraction in equation 7.5, are used to calculate the number of η mesons in the data sample that are expected to come from each of these background τ-decay modes.

The total background contributions: Table 7.6 shows a summary of the numbers of η mesons in the data sample that are expected to come from background modes. When combining the e-tag and μ-tag numbers, uncertainties which are correlated between the two samples are treated differently from those that are uncorrelated.

For each entry, the first error is the statistical uncertainty from the $\pi^+\pi^-\pi^0$ mass spectra fits, due mainly to the limited MC statistics. For these errors, the e-tag and μ-tag contributions are uncorrelated so they can be added in quadrature to produce the error on the combined e- and μ-tagged sample.

Background contribution	Expected number of events					
	e-tag			μ-tag		
$c\overline{c}$	74	± 20	± 19	54	± 15	± 13
uds	20	± 9	± 14	64	± 13	± 43
$\tau^- \to \pi^-\eta\pi^0\nu_\tau$	215	± 14	± 12	118	± 11	± 7
$\tau^- \to \pi^-\eta\overline{K^0}\nu_\tau$	100	± 2	± 17	71	± 2	± 12
$\tau^- \to K^-\eta\nu_\tau$	35	± 1	± 2	26	± 1	± 1
$\tau^- \to K^-\eta\pi^0\nu_\tau$	0.6	± 0.2	± 0.1	0.24	± 0.16	± 0.06
Total	445	± 27	± 31	333	± 23	± 47
Combined e- and μ-tag	$778 \pm 35 \pm 73$					

Table 7.6: The numbers of η mesons in the data sample for $\eta\pi^-$ candidates that are expected to come from each background mode. For each entry, the first error is statistical (due to the limited MC statistics) and the second error is systematic (due to the uncertainties on the τ-decay branching fractions and $q\overline{q}$ simulation scaling factors). Both the statistical and systematic uncertainties are included in the systematic uncertainty on the $\tau^- \to \pi^-\eta\nu_\tau$ branching fraction, as described in section 7.4.3 and listed in table 7.9.

The second error is the systematic uncertainty due to the uncertainties in the branching fractions of the τ-decay background modes and due to the uncertainties on the uds and $c\overline{c}$ scaling factors. For these uncertainties, the e-tag and μ-tag contributions are correlated. The error on the combined e- and μ-tagged sample is calculated directly from the combined sample (instead of by combining the errors calculated separately for the e-tagged and μ-tagged samples). Both the statistical and systematic uncertainties on the background contributions are included in the systematic uncertainty on the final measurement of the $\tau^- \to \pi^-\eta\nu_\tau$ branching fraction, as described in section 7.4.3.

7.4.2 Signal efficiency for $\tau^- \to \pi^-\eta\nu_\tau$

The signal efficiency is the probability that genuine $\tau^- \to \pi^-\eta\nu_\tau$ events pass all the selections and contribute an η meson to the η peak.

Figure 7.12 shows the $\pi^+\pi^-\pi^0$ mass spectra for the dedicated $\tau^- \to \pi^-\eta\nu_\tau$ MC sample, which are fitted to calculate the number of η mesons in the sample. This number is divided by the total number of events in the $\tau^- \to \pi^-\eta\nu_\tau$ sample (from table 6.1) to calculate the signal efficiency. The signal efficiency is found to be $(0.286 \pm 0.004)\%$ for e-tagged events and $(0.186 \pm 0.004)\%$ for μ-tagged events, resulting in an overall signal efficiency for e- and μ-tagged events of $(0.472 \pm$

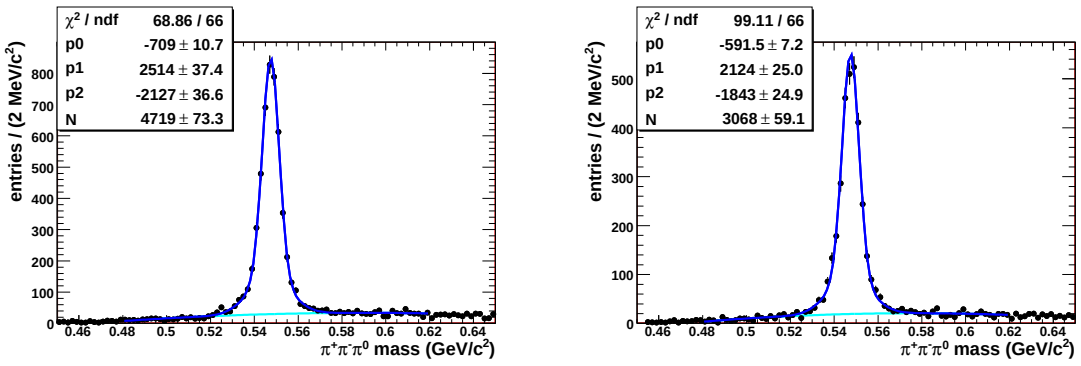

(a) e-tag events (b) μ-tag events

Figure 7.12: The $\pi^+\pi^-\pi^0$ mass distribution for $\pi^-\pi^+\pi^-\pi^0$ candidates selected from the dedicated $\tau^- \to \pi^-\eta\nu_\tau$ MC sample.

0.006)%, where the errors given are statistical only. The uncertainty on the signal efficiency is included in the systematic uncertainty on the $\tau^- \to \pi^-\eta\nu_\tau$ branching fraction measurement (as described in section 7.4.3).

The selection efficiency for the $\tau^- \to K^-\eta\nu_\tau$ signal is higher than that of $\tau^- \to \pi^-\eta\nu_\tau$ mainly because the efficiency of the selection on the thrust magnitude is $\sim 10\%$ higher for $\tau^- \to K^-\eta\nu_\tau$ events.

7.4.3 Systematic uncertainties on $\tau^- \to \pi^-\eta\nu_\tau$

The following sources of uncertainty are accounted for in the systematic error on the $\tau^- \to \pi^-\eta\nu_\tau$ branching fraction measurement. The systematic uncertainties are listed quantitatively in tables 7.6 and 7.9. The uncertainties on the combined e- and μ-tagged sample are calculated directly from the combined sample (instead of by combining the errors calculated separately from the e-tagged and μ-tagged samples), thus avoiding problems caused by correlations between the e-tagged and μ-tagged samples.

The systematic uncertainty on the $\tau^- \to \pi^-\eta\nu_\tau$ branching fraction is calculated in the same way as the systematic uncertainty on the $\tau^- \to K^-\eta\nu_\tau$ branching fraction (see section 7.3.4). However, the systematic uncertainties in table 7.6 can not be expressed as percentage errors on the $\tau^- \to \pi^-\eta\nu_\tau$ branching fraction until the observed signal is known and therefore the various contributions to the systematic uncertainty can not be combined. The observed signal is given in section 7.4.5 (table 7.8) so the total systematic uncertainty on the $\tau^- \to \pi^-\eta\nu_\tau$

branching fraction is shown in the same section, in table 7.9.

For the following uncertainties, the e-tag and μ-tag contributions are correlated:

- Branching fractions: The uncertainty on the τ-decay branching fractions (the Belle branching fractions from table 6.3 and the $\tau^- \to K^-\eta\nu_\tau$ branching fraction in equation 7.5) and the $q\overline{q}$ simulation scaling factors is listed in table 7.6 as ± 73 events for the combined e- and μ-tagged sample. This is the dominant source of systematic uncertainty.

- Bachelor pion PID: As described in section 4.4, the PID efficiency corrections applied to the MC events have corresponding uncertainties. The uncertainty on the PID efficiency correction applied for the *piLHTight* pion candidate list is 0.2%.

- Tracking efficiency: As described in section 4.4, there is an uncertainty on the tracking efficiency of charged particles. An uncertainty of 0.5% is assigned to each of the four tracks and added linearly, giving an uncertainty of 2.0%.

- π^0 detection efficiency: As described in chapter 5, there is an uncertainty of 0.85% on the π^0 detection efficiency, assigned for the π^0 candidate.

- Luminosity: An estimated uncertainty of 0.5% is correlated between the different Runs, while an estimated uncertainty of 0.42% is uncorrelated. The total uncertainty when combining Runs 1 through 6 is 0.65% [64].

- $\tau^+\tau^-$ cross section: The cross section for τ production at $\Upsilon(4S)$ is 0.919 ± 0.003 nb [21], giving a 0.31% systematic uncertainty.

For the following uncertainties, the e-tag and μ-tag contributions are uncorrelated:

- MC statistics of background contributions: Table 7.6 shows that, for the combined e- and μ-tagged sample, there is an uncertainty of ± 35 events on the background contributions, due mainly to the limited MC statistics.

- Error on efficiency due to MC statistics: The statistical uncertainty on the signal efficiency, calculated in section 7.4.2, is $0.006\%/0.472\% = 1.2\%$ for the combined e- and μ-tagged sample. (Similarly, the uncertainty is

0.004%/0.286% = 1.6% for the e-tagged sample and 0.004%/0.186% = 1.9% for the μ-tagged sample).

- Fitting of data: The values of each of the five fixed double-Gaussian parameters are increased and decreased, one at a time, by one standard deviation. The largest difference in the number of η mesons counted in the data sample is included in the systematic uncertainty. This uncertainty can only be quantified once the data is fitted in the following sections. For the MC samples, this uncertainty is negligible when compared to the other uncertainties.

- Tag particle ID: As described in section 4.4, the PID efficiency corrections applied to MC events have corresponding uncertainties. The uncertainty on the corrections applied for the *pidLHElectron* electron candidate list is 0.7% and for the *muNNTight* muon candidate list is 1.8%. For the combined e- and μ-tagged sample, the uncertainties are weighted by the relative numbers of e-tagged and μ-tagged events and added together to give 1.1%.

7.4.4 Calculation of expected upper limit

Before unblinding the data, the possible extent to which this analysis is sensitive in measuring the branching fraction of $\tau^- \to \pi^-\eta\nu_\tau$ is estimated. The total sum of all the MC background modes is used, as shown in figure 7.11. The MC samples are normalised to the data luminosity, and the uds and $c\overline{c}$ samples are scaled according to the scaling factors in section 7.2, so that the total MC sample closely simulates the data sample. No $\tau^- \to \pi^-\eta\nu_\tau$ MC events are included in the sample.

The $\pi^+\pi^-\pi^0$ mass spectra for the total MC sample are fitted to give the numbers of η mesons, as shown in figure 7.13. The expected statistical uncertainty comes directly from the fit and is given in table 7.7. The systematic uncertainty, also shown in table 7.7, is calculated by varying each of the fixed parameters of the fit by one standard deviation, as described in section 7.4.3. The uncertainties are therefore measured in the same way as they will be for the data sample (as described in section 7.4.5). Continuum MC samples are included in the total data-like MC sample but not in the samples used to calculate the background contributions, which is why in table 7.7 the number of η mesons is different for each (but they agree within statistical errors).

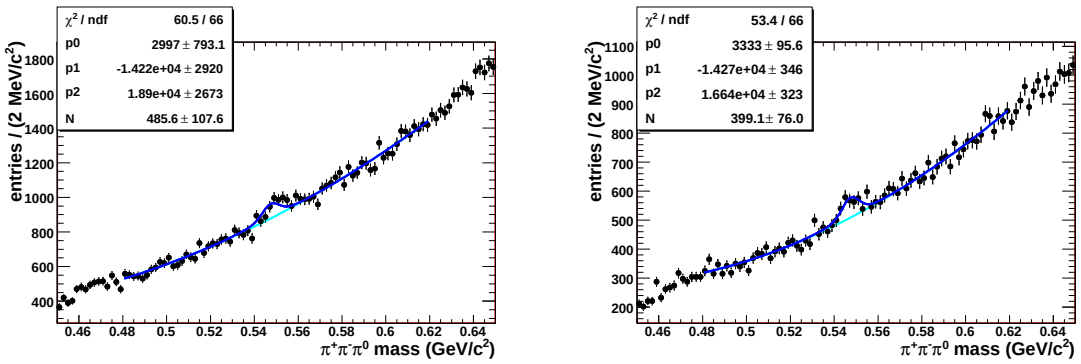

(a) e-tag events (b) μ-tag events

Figure 7.13: Invariant $\pi^+\pi^-\pi^0$ distribution for $\pi^-\pi^+\pi^-\pi^0$ candidates selected from the total data-like MC sample. It is fitted to obtain the expected upper limit for the $\tau^- \to \pi^-\eta\nu_\tau$ branching fraction in section 7.4.4.

The number of $\tau^- \to \pi^-\eta\nu_\tau$ decays in the total MC sample is known to be zero. However, the expected statistical and systematic uncertainty on the number of signal $\tau^- \to \pi^-\eta\nu_\tau$ decays must be calculated, using the uncertainties on the numbers of η mesons in the MC samples. The total uncertainty on the number of η mesons expected to come from background modes (calculated in section 7.4.1 and shown in table 7.7) is combined in quadrature with the systematic uncertainty on the number of η mesons in the total MC sample, and used as the systematic uncertainty on the number of signal $\tau^- \to \pi^-\eta\nu_\tau$ decays. The statistical uncertainty is equal to the statistical uncertainty on the number of η mesons in the total MC sample.

The 95% confidence level upper limit is obtained using 1.645σ, where σ is the total uncertainty on the number of $\tau^- \to \pi^-\eta\nu_\tau$ signal decays [65], as given in table 7.7 (the contributions from the other sources of uncertainty listed in section 7.4.3 are included but are negligible in comparison). The upper limit is calculated in this way because statistically a value drawn from a Gaussian distribution has a 95% probability of being less than the value that is 1.645 standard deviations above the mean [65] (as calculated from a one-tailed Gaussian integral). Using the known branching fractions of $\eta \to \pi^+\pi^-\pi^0$ and $\pi^0 \to \gamma\gamma$ (from table 6.3), the signal efficiency found in section 7.4.2 and the total number of τ decays in the data sample (864 million) it is converted into an expected upper limit on the $\tau^- \to \pi^-\eta\nu_\tau$ branching fraction. The result is 6.4×10^{-5} at the 95% confidence level.

	Expected number of events					
	e-tag			μ-tag		
Total background	445	± 27	± 31	333	± 23	± 47
Combined e- and μ-tag	$778 \pm 35 \pm 73$					
Total data-like MC	486	± 108	± 14	399	± 76	± 12
Combined e- and μ-tag	$885 \pm 132 \pm 18$					
$\tau^- \to \pi^-\eta\nu_\tau$ signal		± 108	± 43		± 76	± 53
Combined e- and μ-tag	$\pm 132 \pm 83$					
Total uncertainty	156					

Table 7.7: The total number of η mesons that are expected to come from background modes (as shown in table 7.6), and the number of η mesons in the total data-like MC sample (as found in section 7.4.4). The uncertainties are used to calculate the expected uncertainty on the number of signal $\tau^- \to \pi^-\eta\nu_\tau$ decays. For each entry, the first error is statistical and the second error is systematic. The statistical error on the $\tau^- \to \pi^-\eta\nu_\tau$ signal is equal to the statistical error on the total data-like MC sample. The systematic uncertainty on the $\tau^- \to \pi^-\eta\nu_\tau$ signal is equal to the systematic uncertainty on the total data-like MC sample added in quadrature with the statistical and systematic uncertainties on the background contributions. The total uncertainty is obtained by combining the statistical and systematic errors on the $\tau^- \to \pi^-\eta\nu_\tau$ signal in quadrature and it is used to give the 95% confidence level expected upper limit on the $\tau^- \to \pi^-\eta\nu_\tau$ branching fraction.

7.4.5 Results of search for $\tau^- \to \pi^-\eta\nu_\tau$ decays

Figure 7.14 shows the $\pi^+\pi^-\pi^0$ mass spectra for the data sample which are fitted to find the numbers of η mesons. There are found to be 913 ± 134 η mesons in the combined e- and μ-tagged data samples.

The total number of η mesons in the data sample that are expected to come from background modes was reported in section 7.4.1 to be 445 ± 41 for the e-tagged sample and 333 ± 52 for the μ-tagged sample. These background contributions are subtracted from the number of η mesons seen in data, as shown in table 7.8, to give the observed signal, which is the number of η mesons in data expected to have come from $\tau^- \to \pi^-\eta\nu_\tau$ decays.

Now that the observed signal is known, each systematic uncertainty in table 7.8 is expressed as a percentage of the observed signal and combined with the

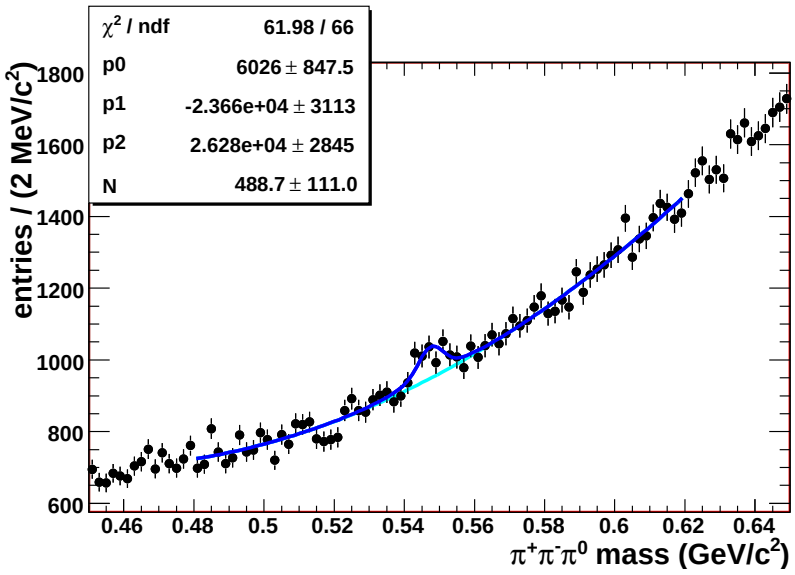

(a) e-tag events

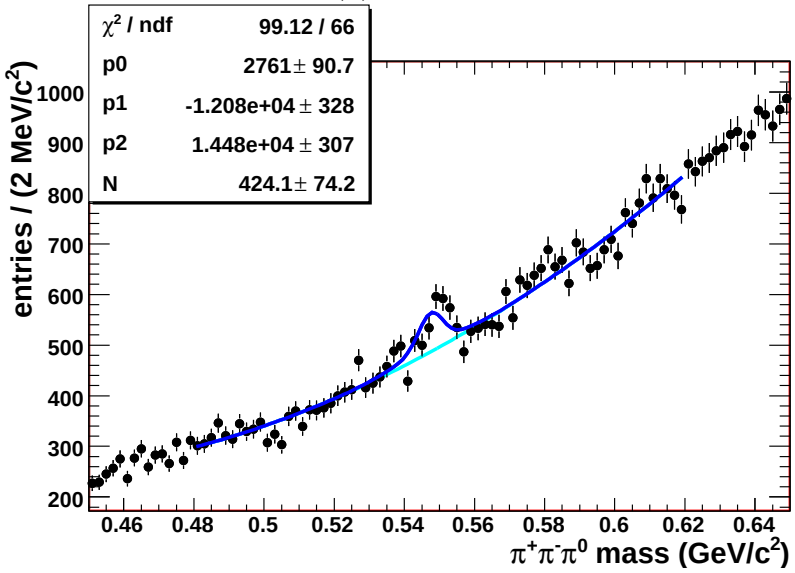

(b) μ-tag events

Figure 7.14: Invariant $\pi^+\pi^-\pi^0$ distribution for $\pi^-\pi^+\pi^-\pi^0$ candidates selected from the data sample.

Background contribution	Expected number of events	
	e-tag	μ-tag
Total background	$445 \pm 27 \pm 31$	$333 \pm 23 \pm 47$
Combined e- and μ-tag	$778 \pm 35 \pm 73$	
Data	$489 \pm 111 \pm 15$	$424 \pm 74 \pm 13$
Combined e- and μ-tag	$913 \pm 134 \pm 20$	
Observed signal (data - background)	$44 \pm 111 \pm 43$	$91 \pm 74 \pm 54$
Combined e- and μ-tag	$135 \pm 134 \pm 83$	

Table 7.8: The total number of η mesons in the data sample that are expected to come from background modes (as shown in table 7.6), and the number of η mesons in the data sample for $\eta\pi^-$ candidates (as found in section 7.4.5 after unblinding). The observed signal is the number of η mesons in the data after all the background contributions have been subtracted (as described in section 7.4.5). For each entry, the first error is statistical and the second error is systematic. The statistical error on the observed signal is equal to the statistical error on the data. The systematic uncertainty on the observed signal is equal to the systematic uncertainty on the data added in quadrature with the statistical and systematic uncertainties on the background contributions. These systematic uncertainties are also included in table 7.9.

other percentage errors from section 7.4.3 to give the total systematic uncertainty on the $\tau^- \to \pi^-\eta\nu_\tau$ branching fraction, as shown in table 7.9. For example, the systematic uncertainty on the fitting of the data (as described in section 7.4.3) is measured as ± 20 events for the combined e- and μ-tagged sample, as shown in table 7.8. This uncertainty is applied to the observed signal of 135 events, giving an uncertainty of 15% on the $\tau^- \to \pi^-\eta\nu_\tau$ branching fraction, as shown in table 7.9.

The branching fraction is calculated using equation 7.1, where $N_{data} - N_{bkgd}$ is the observed signal given in table 7.8, N_{total} is 864 million, ϵ is the signal efficiency given in section 7.4.2 and f is 0.978. Therefore, the $\tau^- \to \pi^-\eta\nu_\tau$ branching fraction is found to be $3.4 \pm 3.4(\text{stat}) \pm 2.1(\text{syst}) \times 10^{-5}$ for the combined e- and μ-tagged sample. The statistical uncertainty is the statistical uncertainty on the fits to the data mass spectra (in table 7.8). The systematic uncertainty is the total systematic uncertainty listed in table 7.9.

Since there is no significant $\tau^- \to \pi^-\eta\nu_\tau$ signal, the 95% confidence level

Source	e-tag	μ-tag	e- and μ-tag
Branching fractions	70%	51%	54%
MC statistics of background contributions	61%	25%	26%
Fitting to data	34%	14 %	15%
Tracking efficiency	2.0%	2.0%	2.0%
Error on efficiency due to MC statistics	1.6%	1.9%	1.2%
e-tag, μ-tag PID	0.7%	1.8%	1.1%
π^0 efficiency	0.9%	0.9%	0.9%
Luminosity and $\sigma_{\tau^+\tau^-}$	0.7%	0.7%	0.7%
Bachelor π^- PID	0.2%	0.2%	0.2%
Total systematic uncertainty	99%	59%	62%

Table 7.9: The systematic uncertainties on the measurement of the $\tau^- \to \pi^-\eta\nu_\tau$ branching fraction. The systematic uncertainties in table 7.8 have been expressed as percentages so that they can be included. The entries in each column are added in quadrature to give the total systematic uncertainty, which is dominated by the uncertainty due to the τ-decay branching fractions and the $q\overline{q}$ simulation scaling factors.

upper limit is obtained using $\mathcal{B} + 1.645\sigma$, where $\mathcal{B}$ is the measured $\tau^- \to \pi^-\eta\nu_\tau$ branching fraction and σ is the total error on the branching fraction [65]. This results in the 95% confidence level upper limit of

$$\mathcal{B}(\tau^- \to \pi^-\eta\nu_\tau) \leq 9.9 \times 10^{-5}. \tag{7.6}$$

This is an improvement on the existing upper limit of 1.4×10^{-4} which was set by the CLEO [17] Collaboration.

The systematic uncertainty is dominated by the uncertainties on the branching fractions of the background modes and the uncertainties in the $q\overline{q}$ simulation scaling factors, which contributes a total of ± 73 events (as shown in table 7.8) to the error on the observed signal of 135 events.

Chapter 8

Summary and conclusion

The analysis described in this thesis uses 470.1 fb^{-1} of integrated luminosity collected by the *BABAR* detector to measure the branching fraction of $\tau^- \to K^-\eta\nu_\tau$ and to search for $\tau^- \to \pi^-\eta\nu_\tau$ decays, using the $\eta \to \pi^+\pi^-\pi^0$ mode.

Dedicated samples of MC events are made for the signal and each background mode. Events which include $\tau \to (\pi^-/K^-)\pi^+\pi^-\pi^0$ candidates are selected from the data and background MC samples. The number of η mesons in each sample is counted by fitting the $\pi^+\pi^-\pi^0$ mass spectrum for the sample, around the region dominated by the η mass peak. The numbers of η mesons expected to come from each background mode is subtracted from the number of η mesons in the data, to give the observed signal. The observed signal is the number of η mesons in the data sample that is expected to have come from the signal $\tau^- \to (\pi^-/K^-)\eta\nu_\tau$ decays, and it is used to calculate a branching fraction.

The branching fraction for the $\tau^- \to K^-\eta\nu_\tau$ channel is found to be

$$\mathcal{B}(\tau^- \to K^-\eta\nu_\tau) = 1.42 \pm 0.11(\text{stat}) \pm 0.06(\text{syst}) \times 10^{-4}.$$

This is consistent with the previous measurement of $(1.52\pm0.05\pm0.1)\times10^{-4}$ found by the Belle Collaboration [16], where a branching fraction of $(1.60\pm0.15\pm0.10)\times 10^{-4}$ is found using only the $\eta \to \pi^+\pi^-\pi^0$ mode and $(1.57 \pm 0.05 \pm 0.09) \times 10^{-4}$ is found using the $\eta \to \gamma\gamma$ mode. For the overall *BABAR* branching fraction to be competitive with the Belle branching fraction, the $\eta \to \gamma\gamma$ mode must also be measured by *BABAR*.

The Belle measurement is lower than previous measurements of this branching fraction, which according to [16] is due to an underestimation of the background contamination in the previous low statistics analyses [17, 31]. This claim is con-

sistent with the *BABAR* measurement reported here, which is lower still. The weighted average of the Belle and *BABAR* result is

$$\mathcal{B}(\tau^- \to K^-\eta\nu_\tau) = (1.52 \pm 0.08) \times 10^{-4},$$

where small correlations in the systematic errors on the results have not been taken into account. An improvement in the measurement of this branching fraction is of some use for making a more accurate determination of V_{us} using hadronic τ decays [34].

The $\tau^- \to \pi^-\eta\nu_\tau$ decay would be mediated by a second-class current and as such is predicted to have a branching fraction of the order 10^{-5}. Second-class currents have never been experimentally observed; this decay mode provides a clean environment to search for them. The search for $\tau^- \to \pi^-\eta\nu_\tau$ decays is carried out blind to avoid bias, so the data remains hidden until the selections have been chosen. An expected upper limit of the $\tau^- \to \pi^-\eta\nu_\tau$ branching fraction is calculated using MC events and found to be $\mathcal{B}(\tau^- \to \pi^-\eta\nu_\tau) < 6.4 \times 10^{-5}$ at the 95% confidence level.

After unblinding the data, the branching fraction is measured as

$$\mathcal{B}(\tau^- \to \pi^-\eta\nu_\tau) = 3.4 \pm 3.4(\text{stat}) \pm 2.1(\text{syst}) \times 10^{-5}.$$

Since there is no evidence for $\tau^- \to \pi^-\eta\nu_\tau$ decays, an upper limit on the branching fraction is found to be

$$\mathcal{B}(\tau^- \to \pi^-\eta\nu_\tau) < 9.9 \times 10^{-5}$$

at the 95% confidence level (or 8.5×10^{-5} at the 90% confidence level). This is an improvement on the previous upper limit of 1.4×10^{-4} at the 95% confidence level, which was measured by CLEO using $\eta \to \gamma\gamma$ events.

The upper limit reported for the $\tau^- \to \pi^-\eta\nu_\tau$ branching fraction is limited by systematic and statistical uncertainties. The systematic uncertainty is dominated by the uncertainty on the branching fractions for the background τ decay modes and by the uncertainty on the scaling of the simulated $q\overline{q}$ events. The η production in *uds* events is studied and is found to be poorly simulated, so further study or more accurate simulation of this process could reduce the systematic uncertainty. Measuring the $\eta \to \gamma\gamma$ mode would improve the limit further or provide evidence

for second-class currents.

Appendix A

$N-1$ distributions

The following figures show the $N-1$ distributions using the selections described in chapter 6. Each page shows distributions for a possible cut variable, for either e-tagged or μ-tagged events.

For each variable the first distribution is for data and the total MC, scaled to the data luminosity. The second distribution is for the (unscaled) $\tau^- \to \pi^- \eta \nu_\tau$ signal MC in white. The following six distributions show the individual background MC modes which contain η mesons, each scaled to the data luminosity. The legend for the $N-1$ distributions is shown in figure A.1.

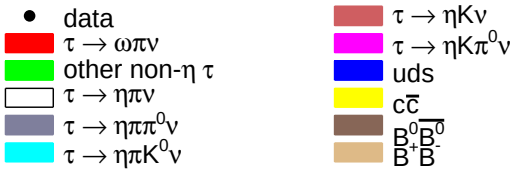

Figure A.1: The legend for the $N-1$ distributions.

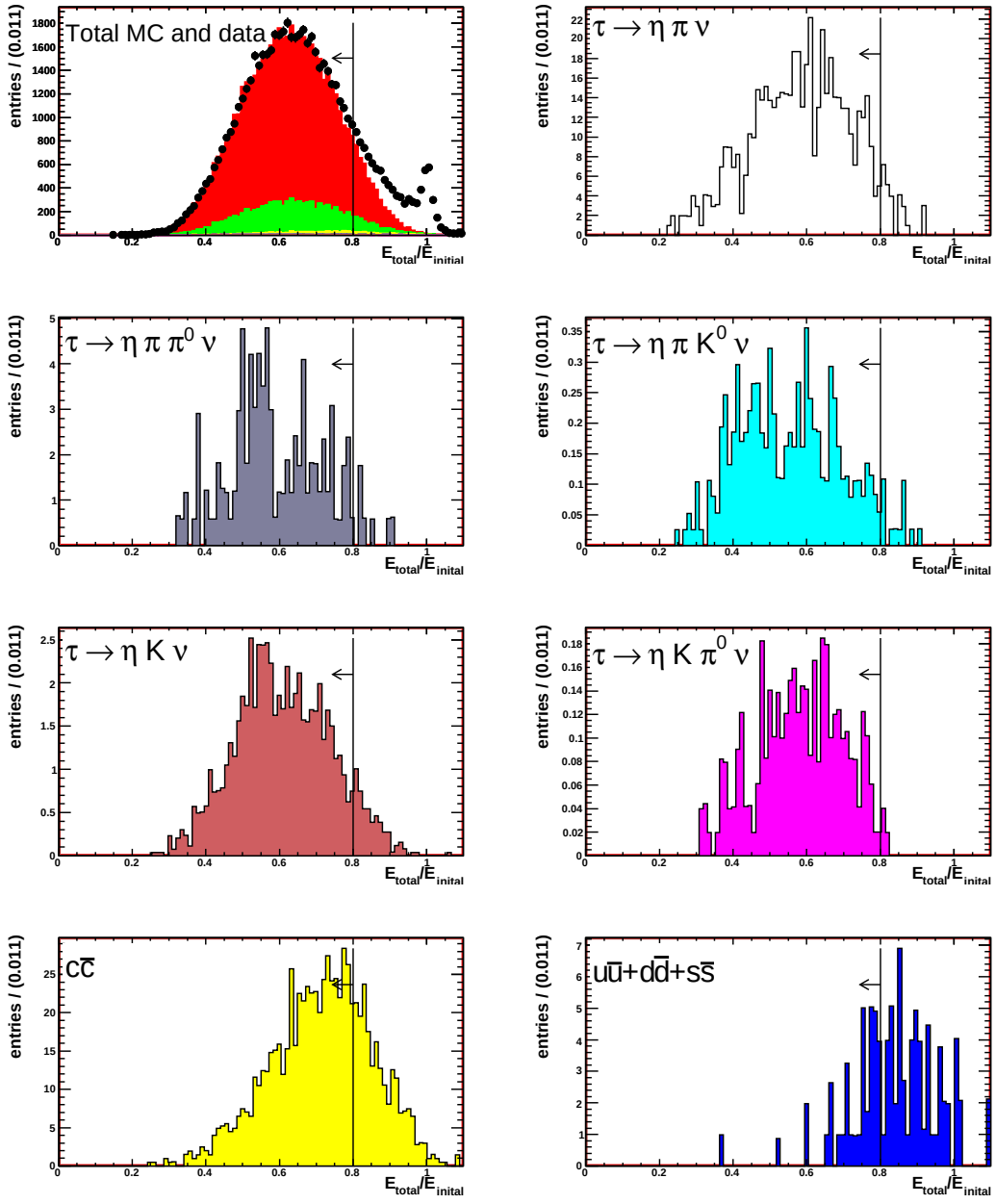

Figure A.2: $N-1$ distribution of $E_{total}/E_{initial}$ for e-tag events, as described in section 6.3.3. The selected region is indicated by the arrow.

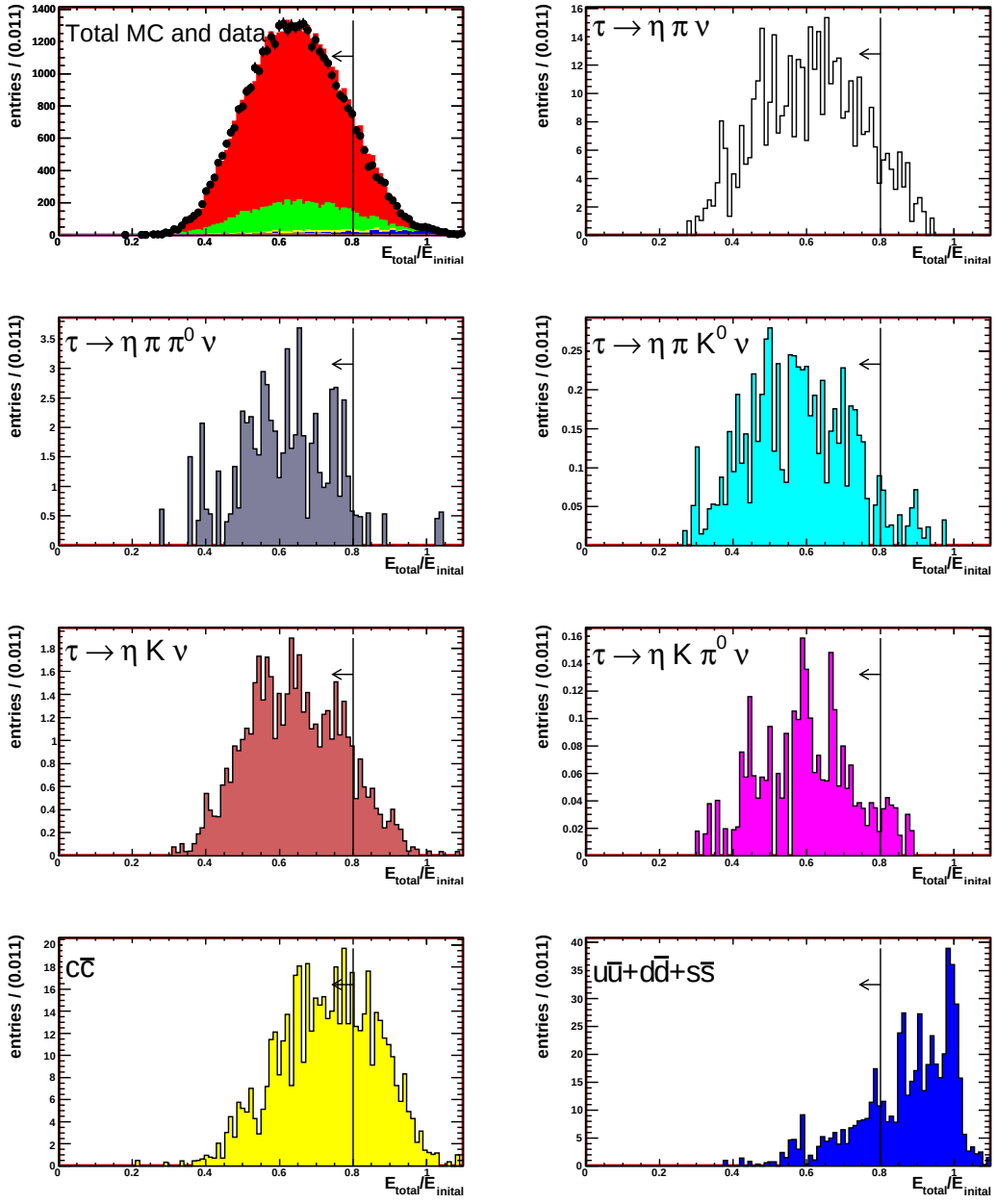

Figure A.3: $N-1$ distribution of $E_{total}/E_{initial}$ for μ-tag events, as described in section 6.3.3. The selected region is indicated by the arrow.

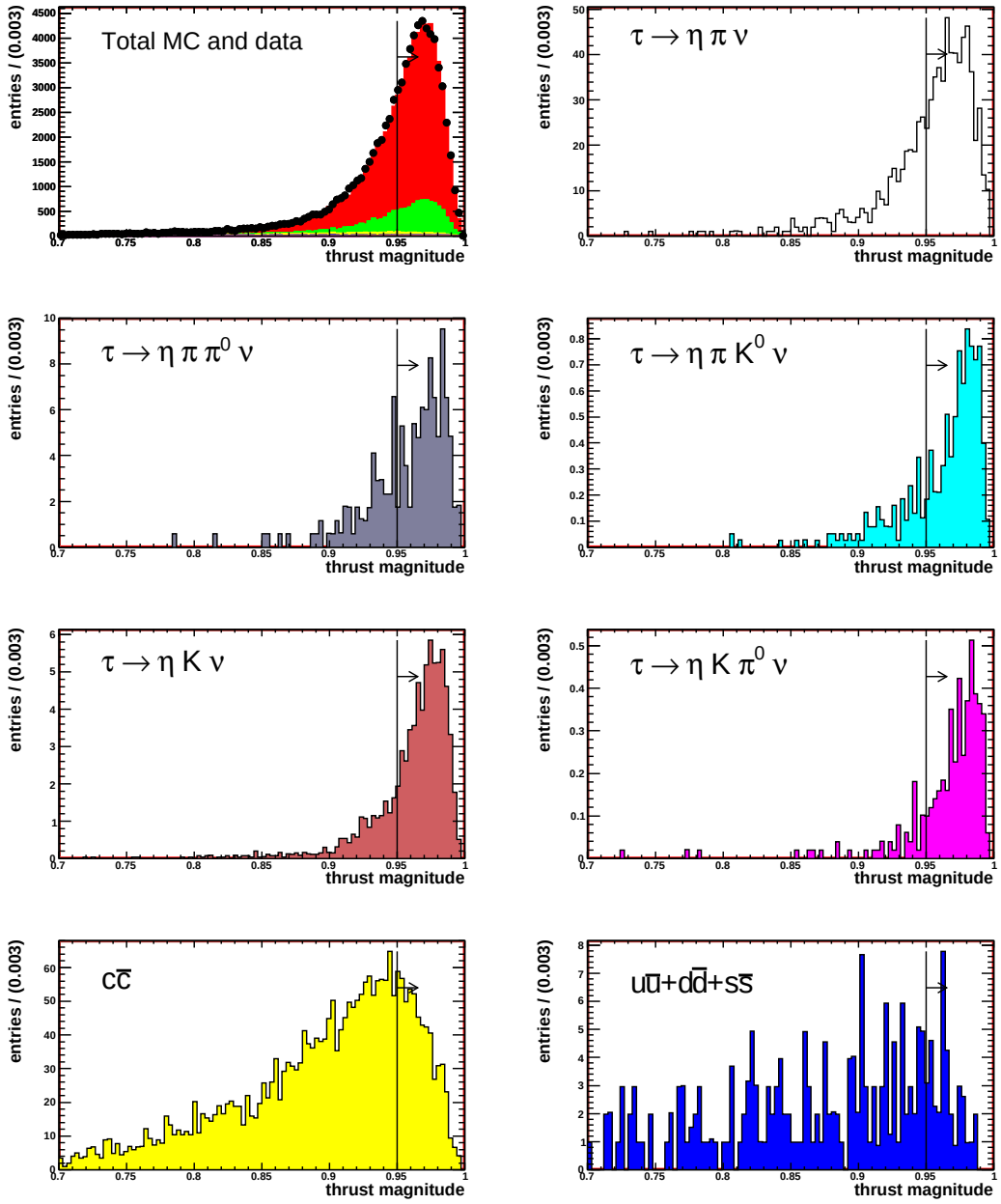

Figure A.4: $N-1$ distribution of the thrust magnitude for e-tag events, as described in section 6.3.3. The selected region is indicated by the arrow.

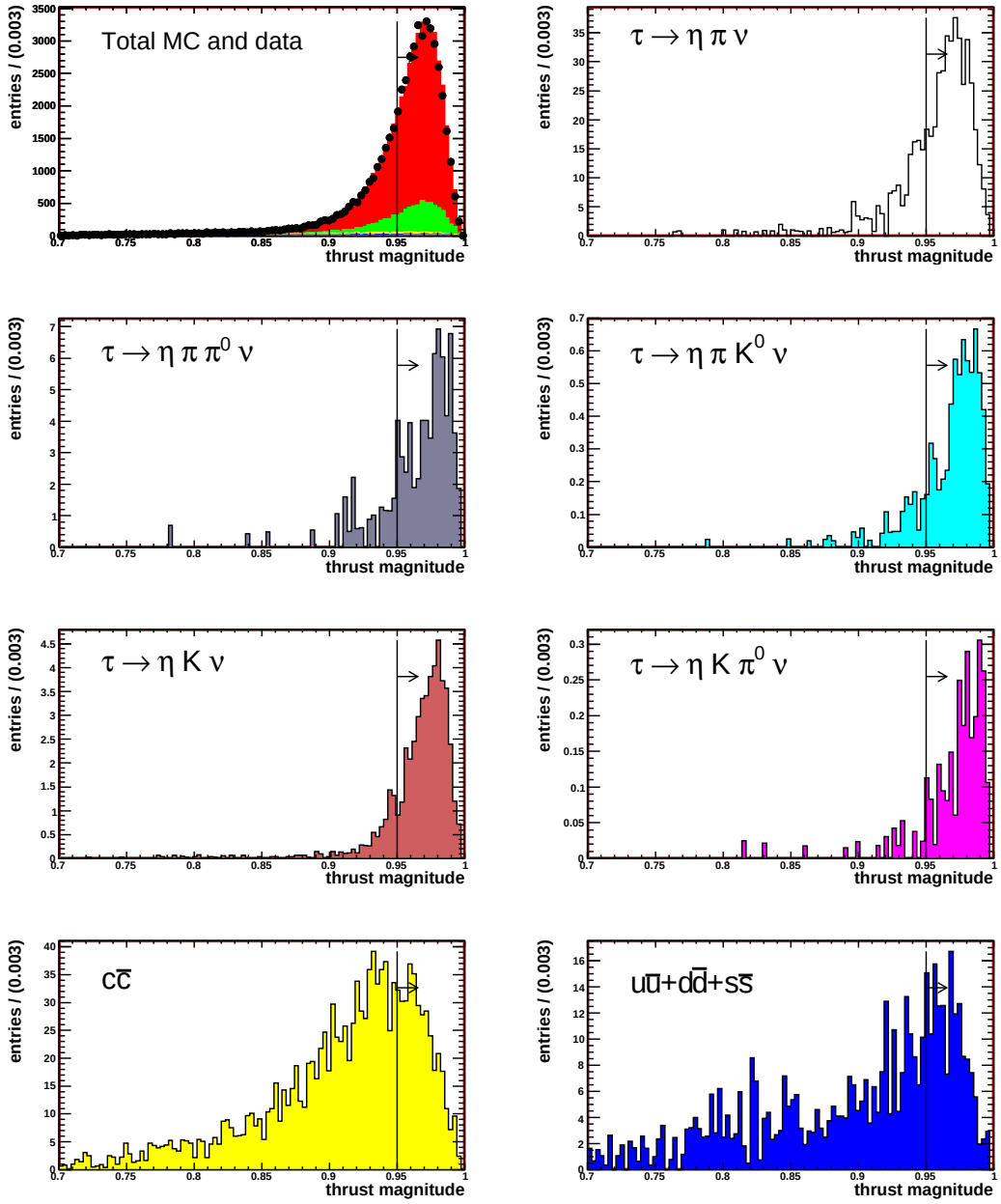

Figure A.5: $N-1$ distribution of the thrust magnitude for μ-tag events, as described in section 6.3.3. The selected region is indicated by the arrow.

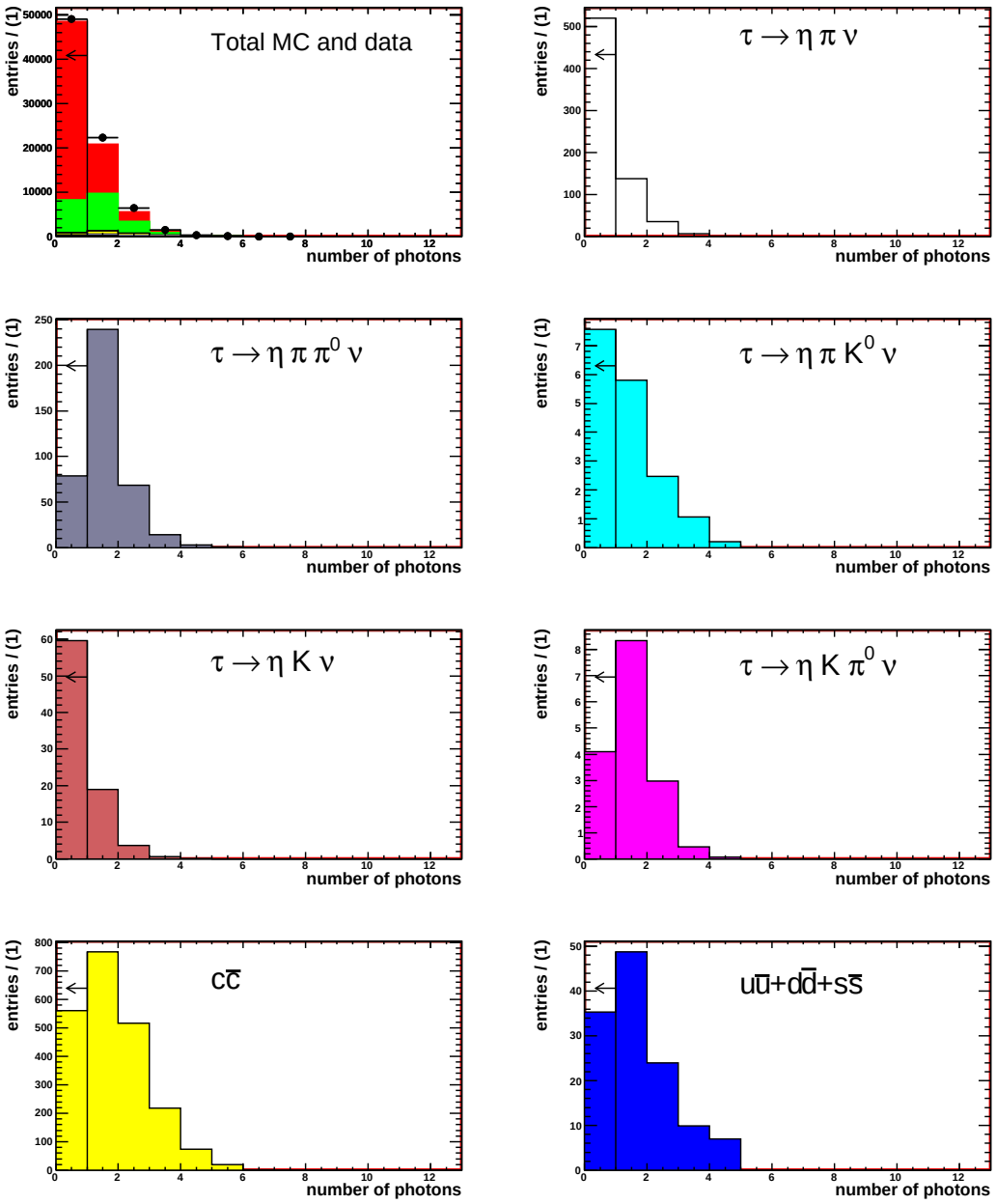

Figure A.6: $N-1$ distribution for the number of signal-side photons which are not daughters of the π^0 and which have an energy of at least 100 MeV, for e-tag events, as described in section 6.3.5. The selected region is indicated by the arrow.

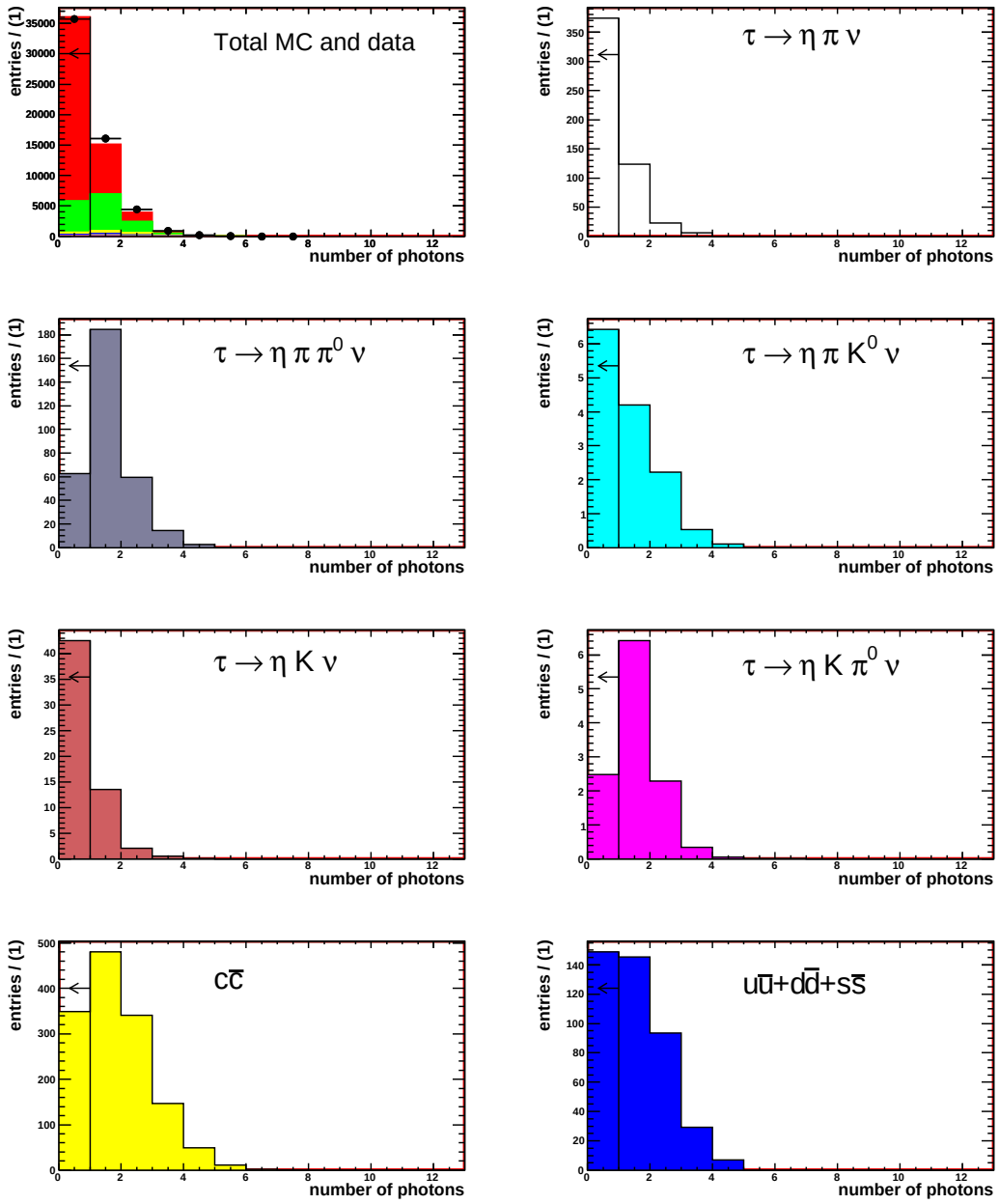

Figure A.7: $N-1$ distribution for the number of signal-side photons which are not daughters of the π^0 and which have an energy of at least 100 MeV, for μ-tag events, as described in section 6.3.5. The selected region is indicated by the arrow.

Appendix B

Distributions for $u\overline{u}/d\overline{d}/s\overline{s}$ background study

Section 7.2.1 describes how the π-tag sample of events is used to investigate the η production in the $u\overline{u}/d\overline{d}/s\overline{s}$ (uds) background. The distributions here are the ηK^- mass, $\eta\pi^-$ mass and $\pi^+\pi^-\pi^0$ mass distributions for the "increased statistics" and "enhanced uds" samples of events.

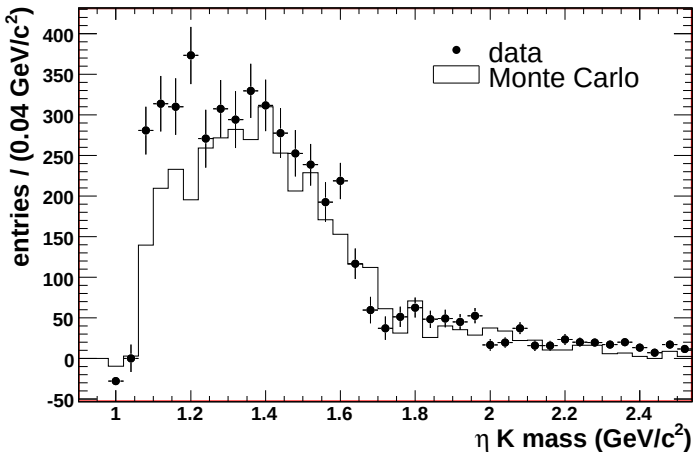

Figure B.1: The ηK^- mass distribution of π-tagged events from the "increased statistics" sample defined in table 7.1, obtained using the sideband subtraction method. The MC samples are normalised to the data luminosity but no additional $q\overline{q}$ scaling has been applied.

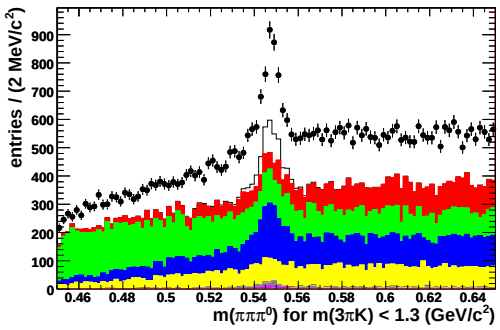

(a) $M(3\pi K) < 1.3$ GeV/c^2

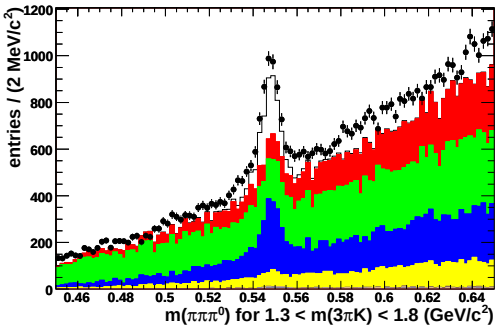

(b) $1.3 < M(3\pi K) < 1.8$ GeV/c^2

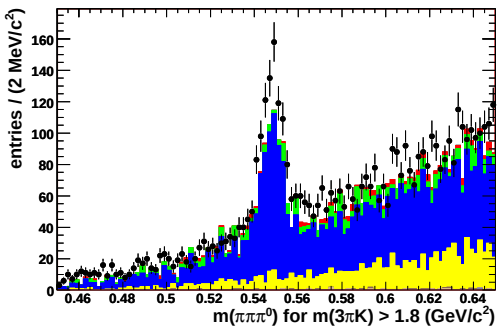

(c) $M(3\pi K) > 1.8$ GeV/c^2

Figure B.2: The $\pi^+\pi^-\pi^0$ mass distribution of π-tagged events (selected for containing $K^-\pi^+\pi^-\pi^0$ candidates) from the "increased statistics" sample defined in table 7.1. The MC samples are normalised to the data luminosity but no additional $q\overline{q}$ scaling has been applied.

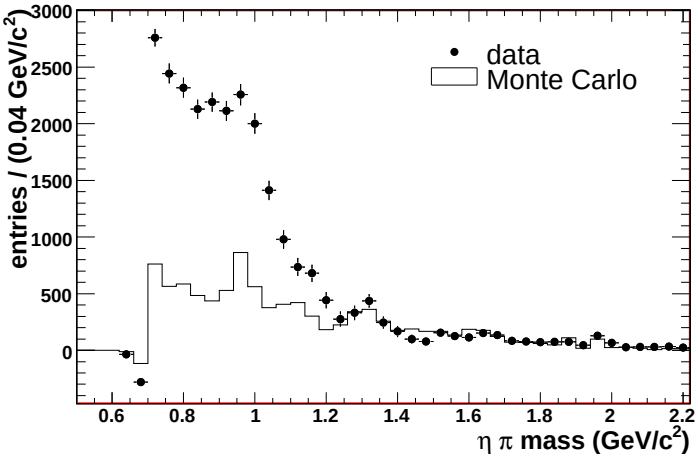

Figure B.3: The $\eta\pi^-$ mass distribution of π-tagged events from the "increased statistics" sample defined in table 7.1, obtained using the sideband subtraction method. The MC samples are normalised to the data luminosity but no additional $q\overline{q}$ scaling has been applied.

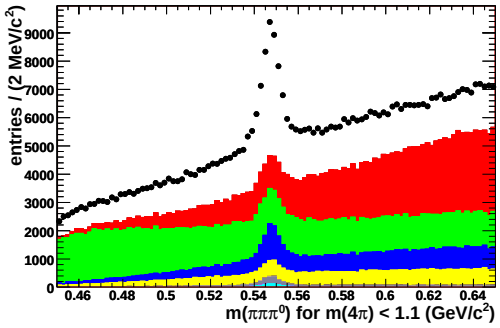

(a) $M(4\pi) < 1.1$ GeV/c^2

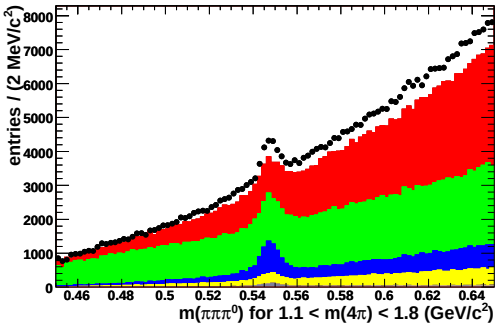

(b) $1.1 < M(4\pi) < 1.8$ GeV/c^2

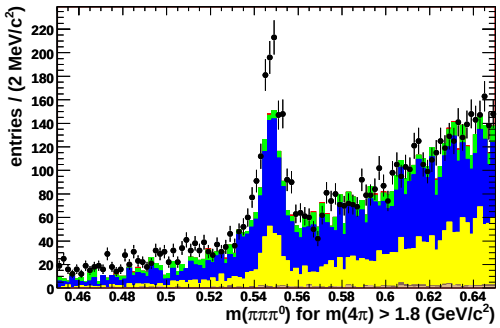

(c) $M(4\pi) > 1.8$ GeV/c^2

Figure B.4: The $\pi^+\pi^-\pi^0$ mass distribution of π-tagged events (selected for containing $\pi^-\pi^+\pi^-\pi^0$ candidates) from the "increased statistics" sample defined in table 7.1. The MC samples are normalised to the data luminosity but no additional $q\overline{q}$ scaling has been applied.

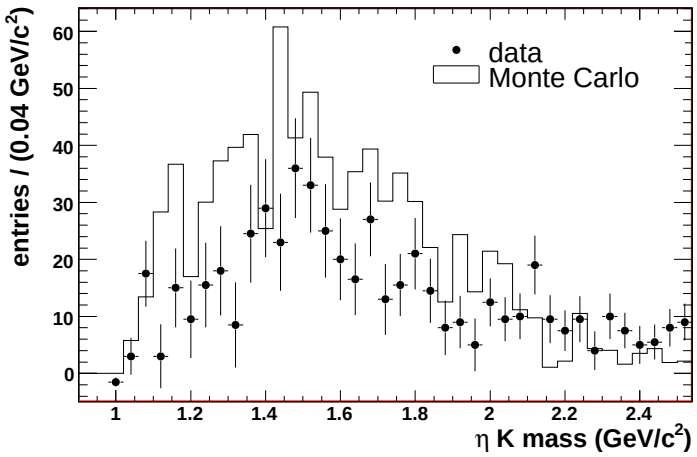

Figure B.5: The ηK^- mass distribution of π-tagged events from the "enhanced *uds*" sample defined in table 7.1, obtained using the sideband subtraction method. The MC samples are normalised to the data luminosity but no additional $q\overline{q}$ scaling has been applied.

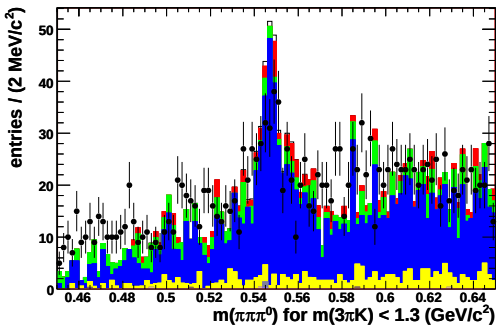

(a) $M(3\pi K) < 1.3$ GeV/c^2

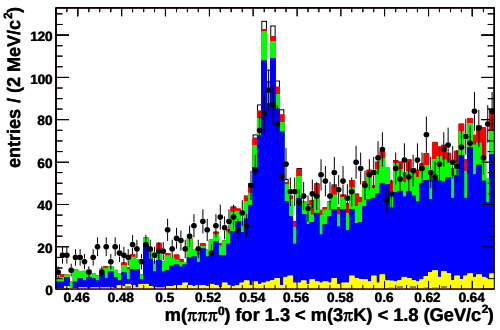

(b) $1.3 < M(3\pi K) < 1.8$ GeV/c^2

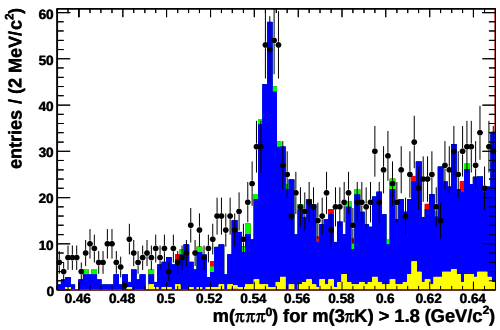

(c) $M(3\pi K) > 1.8$ GeV/c^2

Figure B.6: The $\pi^+\pi^-\pi^0$ mass distribution of π-tagged events (selected for containing $K^-\pi^+\pi^-\pi^0$ candidates) from the "enhanced *uds*" sample defined in table 7.1. The MC samples are normalised to the data luminosity but no additional $q\overline{q}$ scaling has been applied.

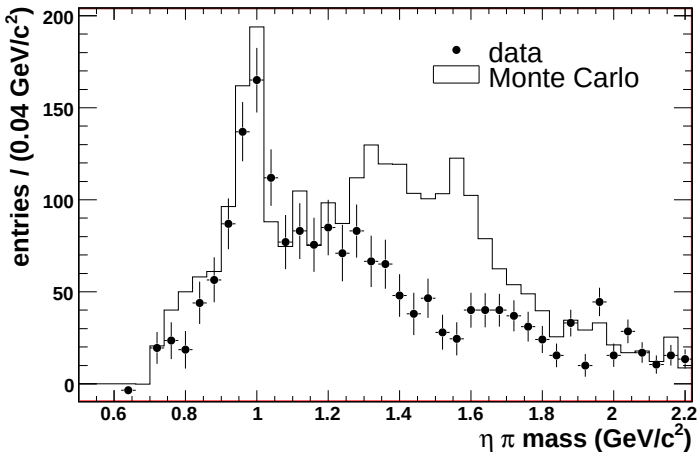

Figure B.7: The $\eta\pi^-$ mass distribution of π-tagged events from the "enhanced *uds*" sample defined in table 7.1, obtained using the sideband subtraction method. The MC samples are normalised to the data luminosity but no additional $q\overline{q}$ scaling has been applied.

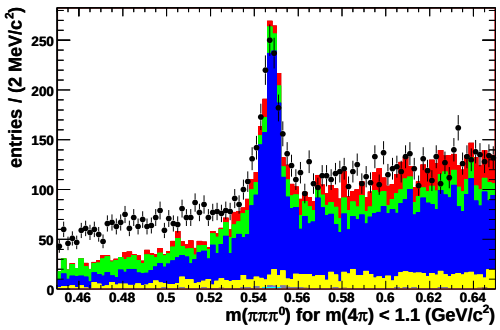

(a) $M(4\pi) < 1.1$ GeV/c^2

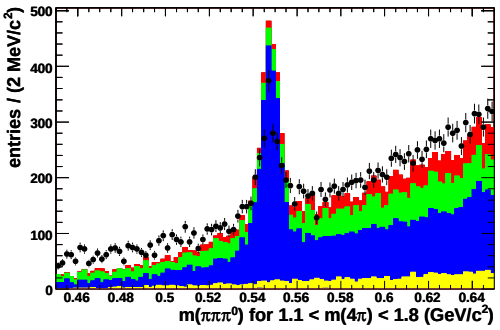

(b) $1.1 < M(4\pi) < 1.8$ GeV/c^2

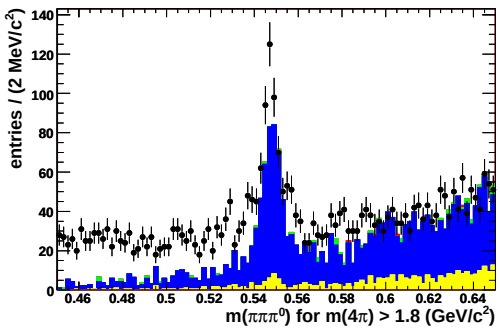

(c) $M(4\pi) > 1.8$ GeV/c^2

Figure B.8: The $\pi^+\pi^-\pi^0$ mass distribution of π-tagged events (selected for containing $\pi^-\pi^+\pi^-\pi^0$ candidates) from the "enhanced *uds*" sample defined in table 7.1. The MC samples are normalised to the data luminosity but no additional $q\overline{q}$ scaling has been applied.

Appendix C

Background contributions to $\tau^- \to K^-\eta\nu_\tau$

As explained in section 7.3.1, for each relevant background mode, the $\pi^+\pi^-\pi^0$ mass spectrum for the MC sample is fitted to count the number of η mesons within the sample.

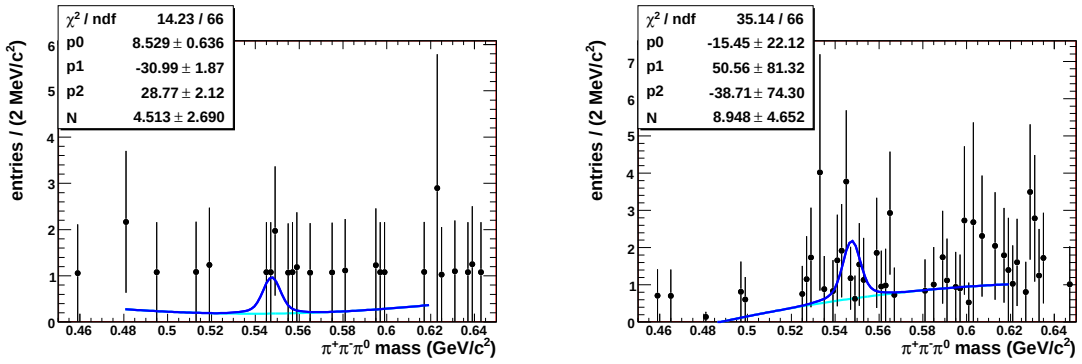

(a) e-tag events (b) μ-tag events

Figure C.1: The $\pi^+\pi^-\pi^0$ mass distribution for $K^-\pi^+\pi^-\pi^0$ candidates selected from the *uds* MC sample.

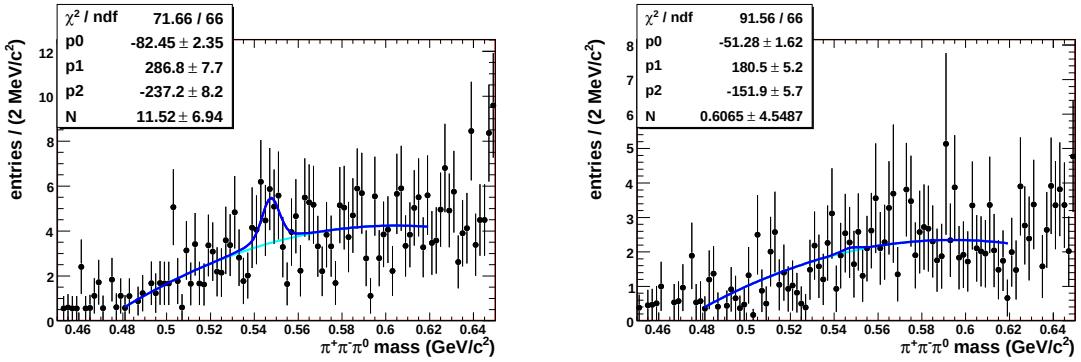

(a) e-tag events (b) μ-tag events

Figure C.2: The $\pi^+\pi^-\pi^0$ mass distribution for $K^-\pi^+\pi^-\pi^0$ candidates selected from the $c\overline{c}$ MC sample.

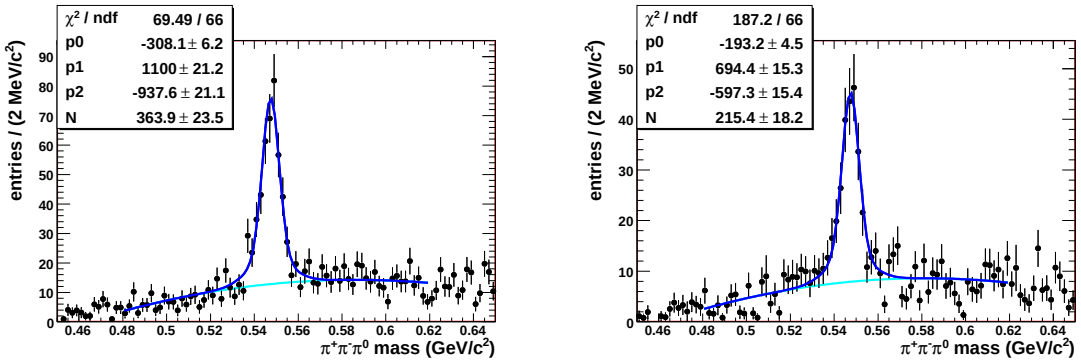

(a) e-tag events (b) μ-tag events

Figure C.3: The $\pi^+\pi^-\pi^0$ mass distribution for $K^-\pi^+\pi^-\pi^0$ candidates selected from the dedicated $\tau^- \to K^-\eta\pi^0\nu_\tau$ MC sample.

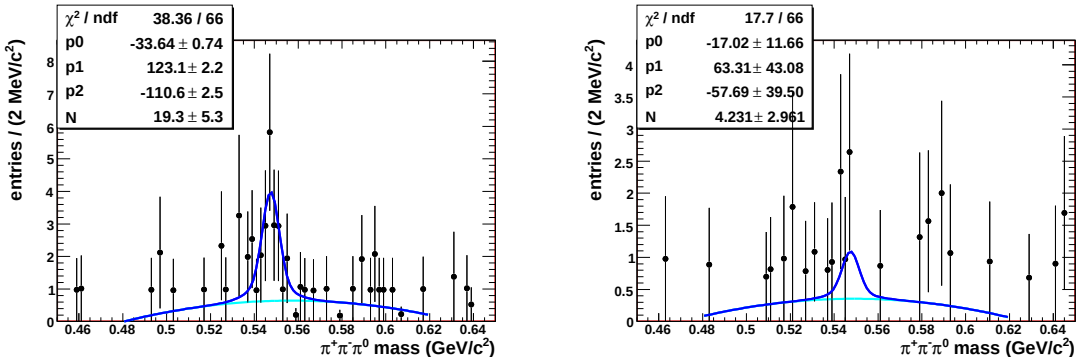

(a) e-tag events (b) μ-tag events

Figure C.4: The $\pi^+\pi^-\pi^0$ mass distribution for $K^-\pi^+\pi^-\pi^0$ candidates selected from the dedicated $\tau^- \to \pi^-\eta\pi^0\nu_\tau$ MC sample.

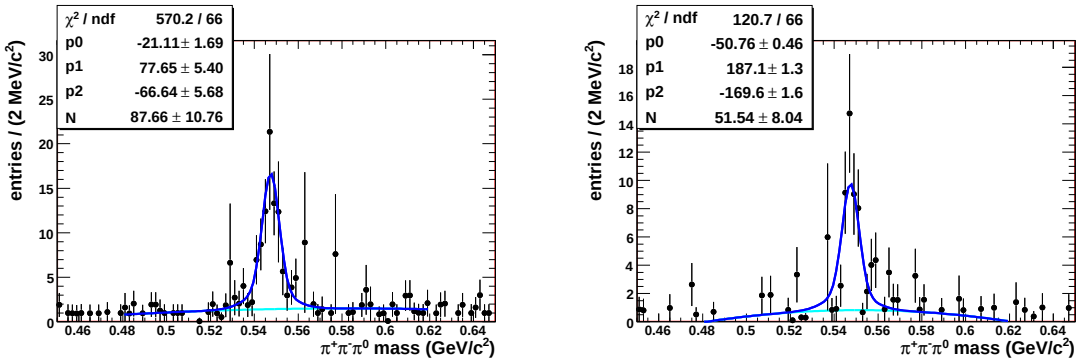

(a) e-tag events (b) μ-tag events

Figure C.5: The $\pi^+\pi^-\pi^0$ mass distribution for $K^-\pi^+\pi^-\pi^0$ candidates selected from the dedicated $\tau^- \to \pi^-\eta\overline{K^0}\nu_\tau$ MC sample.

Appendix D

Background contributions to $\tau^- \longrightarrow \pi^- \eta \nu_\tau$

As explained in section 7.4.1, for each relevant background mode, the $\pi^+\pi^-\pi^0$ mass spectrum for the MC sample is fitted to count the number of η mesons within the sample.

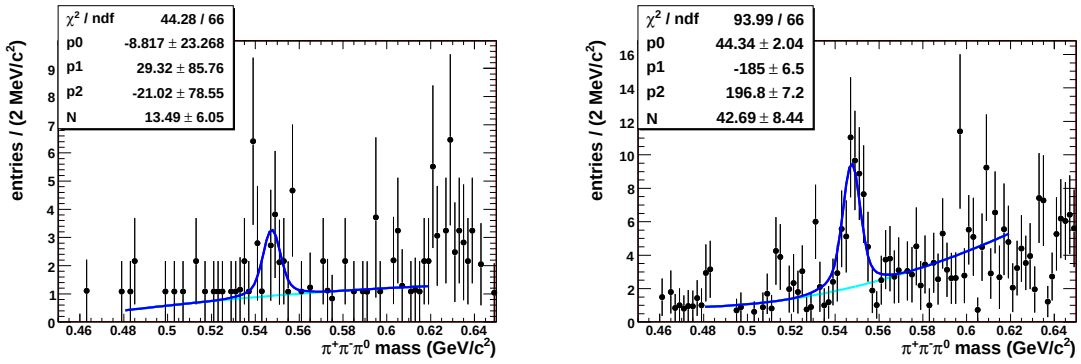

(a) e-tag events (b) μ-tag events

Figure D.1: The $\pi^+\pi^-\pi^0$ mass distribution for $\pi^-\pi^+\pi^-\pi^0$ candidates selected from the *uds* MC sample.

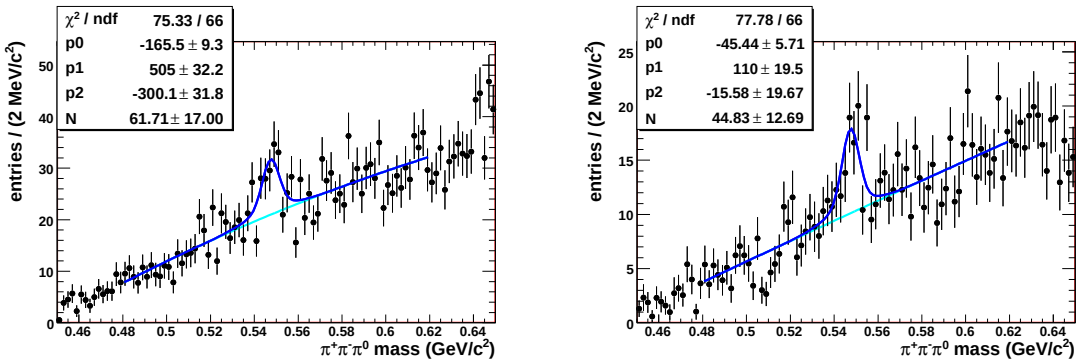

(a) e-tag events (b) μ-tag events

Figure D.2: The $\pi^+\pi^-\pi^0$ mass distribution for $\pi^-\pi^+\pi^-\pi^0$ candidates selected from the $c\overline{c}$ MC sample.

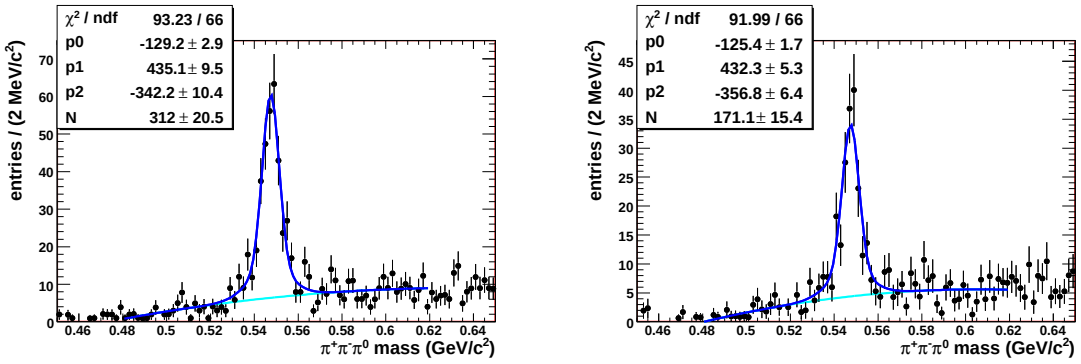

(a) e-tag events (b) μ-tag events

Figure D.3: The $\pi^+\pi^-\pi^0$ mass distribution for $\pi^-\pi^+\pi^-\pi^0$ candidates selected from the dedicated $\tau^- \to \pi^-\eta\pi^0\nu_\tau$ MC sample.

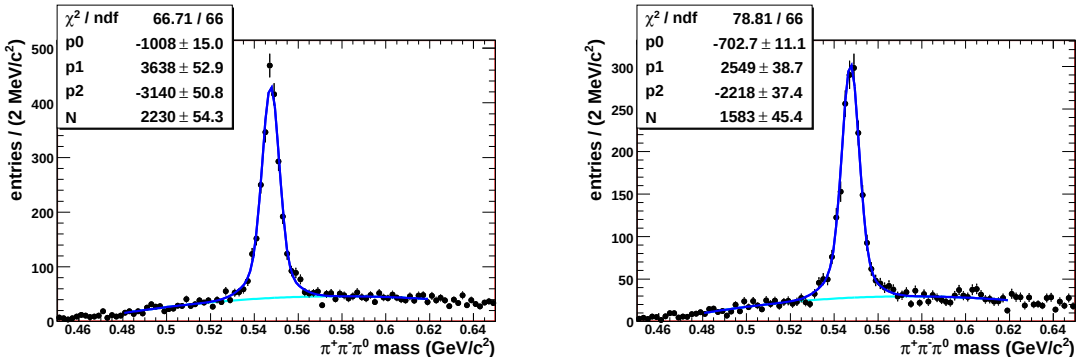

(a) e-tag events (b) μ-tag events

Figure D.4: The $\pi^+\pi^-\pi^0$ mass distribution for $\pi^-\pi^+\pi^-\pi^0$ candidates selected from the dedicated $\tau^- \to \pi^-\eta\overline{K^0}\nu_\tau$ MC sample.

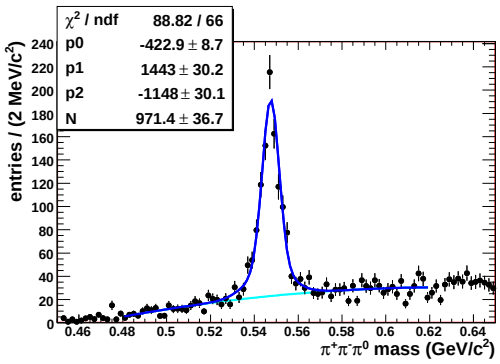

(a) e-tag events

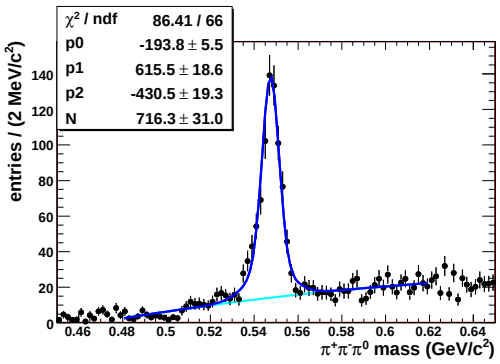

(b) μ-tag events

Figure D.5: The $\pi^+\pi^-\pi^0$ mass distribution for $\pi^-\pi^+\pi^-\pi^0$ candidates selected from the dedicated $\tau^- \to K^-\eta\nu_\tau$ MC sample.

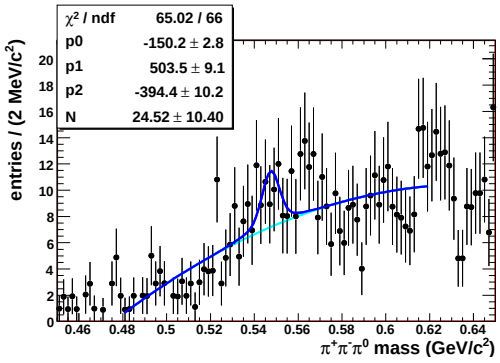

(a) e-tag events

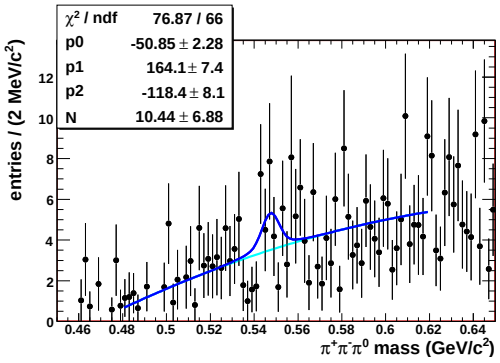

(b) μ-tag events

Figure D.6: The $\pi^+\pi^-\pi^0$ mass distribution for $\pi^-\pi^+\pi^-\pi^0$ candidates selected from the dedicated $\tau^- \to K^-\eta\pi^0\nu_\tau$ MC sample.

References

[1] M. Kobayashi and T. Maskawa, Prog. Theor. Phys **49**, 652 (1973).

[2] J. H. Christenson, J. W. Cronin, V. L. Fitch and R. Turlay, Phys. Rev. Lett. **13**, 138 (1964).

[3] A. D. Sakharov, Pisma Zh. Eksp. Teor. Fiz. **5**, 32 (1967), translated in JETP Lett. **5**, 24 (1967) and reprinted in Sov. Phys. Usp. **34**, 392 (1991).

[4] N. Cabibbo, Phys. Rev. Lett. **10**, 531 (1963).

[5] D. H. Perkins, *Introduction to High Energy Physics, 3rd edition*, Adison-Wesley Publishing Company (1987).

[6] J. -E. Augustin *et al.*, Phys. Rev. Lett. **33**, 1406 (1974);
J. J. Aubert *et al.*, Phys. Rev. Lett. **33**, 1404 (1974).

[7] S. W. Herb *et al.*, Phys. Rev. Lett. **39**, 252 (1977).

[8] F. Abe *et al.* (CDF Collaboration), Phys. Rev. Lett. **74**, 2626 (1995);
S. Abachi *et al.* (D0 Collaboration), Phys. Rev. Lett. **74**, 2422 (1995).

[9] A. B. Carter and A. I. Sanda, Phys. Rev. **D23**, 1567 (1981);
I. I. Bigi and A. I. Sanda, Nucl. Phys. **B193**, 85 (1981).

[10] P. Oddone, *An asymmetric B factory based on PEP*, Second International Symposium on The 4th Family of Quarks and Leptons (California 1989), published in Annals N. Y. Acad. Sci. **578**, 237 (1989).

[11] B. Aubert *et al.* (*BABAR* Collaboration), Phys. Rev. Lett. **87**, 091801 (2001).

[12] K. Abe *et al.* (Belle Collaboration), Phys. Rev. Lett. **87**, 091802 (2001).

[13] I. Aitchison, R. Cowan and O. Long (*BABAR* Collaboration), *Nobel Prize in Physics 2008*, (2008),
`http://www-public.slac.stanford.edu/babar/Nobel2008.htm`.

[14] M. L. Perl *et al.*, Phys. Rev. Lett. **35**, 1489 (1975).

[15] C. Amsler *et al.* (Particle Data Group), Phys. Lett. **B667**, 1 (2008) and partial update for the 2010 edition.

[16] K. Inami *et al.* (Belle Collaboration), Phys. Lett. **B672**, 209 (2009).

[17] J. Bartelt *et al.* (CLEO Collaboration), Phys. Rev. Lett. **76**, 4119 (1996).

[18] W. Heisenberg, Zeitschrift für Physik **A77**, 1 (1932), [doi:10.1007/BF01342433].

[19] M. L. Perl, *Tau Physics*, 20th Annual SLAC Summer Institute on Particle Physics (1992), SLAC-PUB-6071.

[20] A. Stahl, *Physics with Tau Leptons*, Springer (2000).

[21] S. Banerjee, B. Pietrzyk, J. M. Roney and Z. Was, Phys. Rev. **D77**, 054012 (2008).

[22] D. Epifanov *et al.* (Belle Collaboration), Phys. Lett. **B654**, 65 (2007).

[23] S. Weinberg, Phys. Rev. **112**, 1375 (1958).

[24] N. V. Samsonenko and A. D. Nevskii, Bull. Russ. Acad. Sci. Phys. **57**, 1545 (1993).

[25] K. Minamisono *et al.*, Phys. Rev. **C65**, 015501 (2002).

[26] S. Nussinov and A. Soffer, Phys. Rev. **D78**, 033006 (2008).

[27] H. Neufeld and H. Rupertsberger, Z. Phys **C68**, 91 (1995).

[28] S. Tisserant and T.N.Thruong, Phys. Lett. **B115**, 264 (1982).

[29] T. West, *Studies of Hadronic τ decays using the BABAR detector*, PhD Thesis, University of Manchester, UK (2008).

[30] B. Aubert *et al.* (*BABAR* Collaboration), Phys. Rev. **D77**, 112002 (2008).

[31] D. Buskulic *et al.* (ALEPH Collaboration), Z. Phys. **C74**, 263 (1997).

[32] K. W. Edwards *et al.* (CLEO Collaboration), Phys. Rev. **D61**, 072003 (2000).

[33] B. Aubert *et al.* (*BABAR* Collaboration), Phys. Rev. Lett. **103**, 041802 (2009).

[34] K. Maltman *et al.*, Nucl. Phys. Proc. Suppl. **189**, 175 (2009).

[35] B. Aubert *et al.* (*BABAR* Collaboration), Nucl. Instr. Meth. **A479**, 1 (2002).

[36] *BABAR* Collaboration, *BABAR detector image gallery*, (1999), avaliable at http://www.slac.stanford.edu/BFROOT/www/Detector/Images/Images.html.

[37] P. F. Harrison and H. R. Quinn (editors), *The BABAR Physics Book*, (1998).

[38] *BABAR* Collaboration, *Accelerator and detector performance data*, (2009), avaliable at
`http://www-public.slac.stanford.edu/babar/perfdata.html`.

[39] M. Sullivan *et al.*, *Interaction Region Design at the PEP-II B Factory*, (1996), `SLAC-PUB-7206`.

[40] I. Adam *et al.*, Nucl. Instr. Meth. **A538**, 28 (2005).

[41] P. Grosso *et al.*, *The BABAR fast control system*, proceedings of the International Conference on Computing in High Energy Physics, Chicago, IL, USA (1998).

[42] G. P. Dubois-Felsmann, E. Chen, Yu. Kolomensky *et al.*, IEEE Trans. Nucl. Sci. **NS-47**, 353 (2000).

[43] T. Johnson, *Java analysis studio*, proceedings of the International Conference on Computing in High Energy Physics, Padova, Italy (2000).

[44] L. Dalesio *et al.*, Nucl. Instr. and Meth. **A352**, 179 (1994).

[45] B. Franek and C. Gaspar, IEEE Trans. Nucl. Sci. **NS-45**, 1946 (1998).

[46] Wind River Systems, Inc., The VxWorks realtime operating system and Tornado Development interface, Alameda, CA, USA.

[47] D. H. Wouter, *TreeFitter Vertexing Algorithm*, algorithm documented in *Decay Chain Fitting with a Kalman Filter*, published in Nucl. Instrum. Meth. **A552**, 566 (2005).

[48] P. Golonka and Z. Was, Eur. Phys. J. C **45**, 97 (2006).

[49] T. Sjostrand, Comput. Phys. Commun. **82**, 74 (1994).

[50] D. J. Lange, Nucl. Instrum. Methods Phys. Res., Sect. A **462**, 152 (2001).

[51] B. F. Ward, S. Jadach, and Z. Was, Nucl. Phys. Proc. Suppl. **116**, 73 (2003).

[52] S. Jadach, Z. Was, R. Decker and J. H. Kuhn, Comput. Phys. Commun. **76**, 361 (1993).

[53] Radiative processes are based on the Born-level formulae in: A. B. Arbuzov *et al.*, JHEP **9710**, 001 (1997);
The generation of ISR processes uses an approach in: H. Czyz and J.H. Kuhn, Eur. Phys. J. **C18**, 497 (2001).

[54] S. Agostinelli *et al.* (`GEANT4` Collaboration), Nucl. Instrum. Methods Phys. Res., Sect. A **506**, 250 (2003).

[55] I. M. Neugent, M. Roney and R. Kowalewski, *Tau31 Tracking Efficiency Study For 2004*, *BABAR* Analysis Document #931, version 2 (2004).

[56] M. Allen, M. Naisbit, A. Roodman and S. Banerjee, *A Measurement of* π^0 *Efficiency Using* $\tau \to \rho\nu$ *and* $\tau \to \pi\nu$ *Decays*, *BABAR* Analysis Document #870, version 3 (2004).

[57] E. Farhi, Phys. Rev. Lett. **39**, 1587 (1977);
S. Brandt *et al.*, Phys. Lett. **12**, 57 (1964).

[58] S. Banerjee *et al.*, *CM2 skims for* $e^+e^- \to \mu^+\mu^-$ *and* $e^+e^- \to \tau^+\tau^-$ *events (TAUQED2)*, *BABAR* Analysis Document #760, version 1 (2003).

[59] `ROOT` framework for data processing, CERN, documented at:
`http://root.cern.ch`.

[60] J. Allison, Comp. Phys. Comm. **77**, 377 (1993).

[61] M. N. Achasov *et al.*, Phys. Rev. **D66**, 032001 (2002).

[62] R. Barlow, *Systematic errors: facts and fictions*, (2002),
`[arXiv:hep-ex/0207026v1]`.

[63] Private correspondence with E. P. Solodov.

[64] R. Gamet and C. Touramanis, *Luminosity Measurement for the Runs 1,2 and 3 data sample using Release 12 and SP5 Simulation*, *BABAR* Analysis Document #1312, version 1 (2005);
R. Gamet, *Luminosity Measurement for the Run 4 and Run 5 data samples using Release 18d and SP8 Simulation*, *BABAR* Analysis Document #1850, version 1 (2007).

[65] R. J. Barlow, *Statistics*, John Wiley and Sons (1989).